Phase-field modeling of diffusion controlled phase transformations

by

Irina Loginova

October 2003
Technical Reports from
Royal Institute of Technology
Department of Mechanics
S-100 44 Stockholm, Sweden

Typsatt i $\mathcal{A}\mathcal{M}\mathcal{S}$-LaTeX.

Akademisk avhandling som med tillstånd av Kungliga Tekniska Högskolan i Stockholm framlägges till offentlig granskning för avläggande av teknologie doktorsexamen fredagen den 31:a oktober 2003 kl 13.15 i Sal D2, Kungliga Tekniska Högskolan, Valhallavägen 79, Stockholm.

Universitetsservice, Stockholm 2003

Phase-field modeling of diffusion controlled phase transformations

Irina Loginova 2003
Department of Mechanics, Royal Institute of Technology
SE-100 44 Stockholm, Sweden.

Abstract

Diffusion controlled phase transformations are studied by means of the phase-field method. Morphological evolution of dendrites, grains and Widmanstätten plates is modeled and simulated.

Growth of dendrites into highly supersaturated liquids is studied for binary alloy solidification. Phase-field equations that involve both temperature and solute redistribution are formulated. It is demonstrated that while at low undercooling heat diffusion does not affect the growth of dendrites, i.e. solidification is nearly isothermal, at high cooling rates the supersaturation is replaced by the thermal undercooling as the driving force for growth.

In experiments many crystals with different orientations nucleate. The growth of randomly oriented dendrites, their subsequent impingement and formation of grain boundaries are studied in two dimensions using the FEM on adaptive grids.

The structure of dendrites is determined by growth conditions and physical parameters of the solidifying material. Effects of the undercooling and anisotropic surface energy on the crystal morphology are investigated. Transition between seaweeds, doublons and dendrites solidifying out of pure substance is studied and compared to experimental data. Two- and three-dimensional simulations are performed in parallel on adaptive and uniform meshes.

A phase-field method based on the Gibbs energy functional is formulated for austenite to ferrite phase transformation in Fe-C. In combination with the solute drag model, transition between diffusion controlled and massive transformations as a function of C concentration and temperature is established by performing a large number of one dimensional calculations with real physical parameters. In two dimensions, growth of Widmanstätten plates is governed by the highly anisotropic surface energy. It is found that the plate tip can be approximated as sharp, in agreement with experiments.

Descriptors: heat and solute diffusion, solidification, solid-solid phase transformation, microstructure, crystal growth, dendrite, grain boundary, Widmanstätten plate, phase-field, adaptive mesh generation, FEM.

Preface

This thesis concerns modeling of microstructures arising during diffusion controlled phase transformations by means of the phase-field models. The first part of the thesis contains introduction to the field and a review of important works published in the literature. The second part consists of published or submitted papers listed below

Paper 1. I. Loginova, G. Amberg and J. Ågren, 'Phase-field simulations of non-isothermal binary alloy solidification', *Acta materialia,* **49,** 573-581, 2001

Paper 2. J.A. Warren, I. Loginova, L. Gránásy, T. Börzsönyi and T. Pusztai, 'Phase-field modeling of alloy polycrystals', *Proceedings of Modeling Casting and Advanced Solidification Processes X, edited by D. Stefanescu, J. A. Warren, M. Krane and M. Jolly,* 2003.

Paper 3. I. Loginova, J. Odqvist, G. Amberg and J. Ågren, 'The phase-field approach and solute drag modeling of the transition to massive $\gamma \rightarrow \alpha$ transformation in binary Fe-C alloys', *Acta Materialia,* **51,** 1327-1339, 2003

Paper 4. I. Loginova, J. Ågren and G. Amberg, 'On the formation on Widmanstätten ferrite in binary Fe-C - phase-field approach', *submitted to Acta materialia*

Paper 5. I. Loginova, H. Singer, J. Bilgram and G. Amberg, 'Morphology diagram of thermal dendritic solidification by means of phase-field models in 2 and 3 dimensions', *to be submitted to Journal of crystal growth*

Division of work between paper authors

The papers presented in this thesis are written in collaboration with other researchers. Professor Gustav Amberg acted as the supervisor and the project leader in all investigations, except Paper 2. Professor Jonh Ågren from the Department of Materials Science and Engineering was the respondent's second adviser in the projects resulted in Papers 1, 3 and 4.

Paper 1. This work was performed by the respondent.

Paper 2. This work was done during the respondent's visit to NIST, Gaithersburg, MD, USA, under the supervision of Dr. James Warren. The respondent extended the grain boundary model of a pure material to a binary alloy case, and performed the simulations on adaptive grids.

Paper 3. The respondent performed the phase-field part of the paper which included the model derivation, programming and the phase-field simulations.

Paper 4. The work done by the respondent included the model derivation, inclusion of high anisotropy and the simulations. A parallel adaptive FEM code written by Minh Do-Quang was used to perform the calculations.

Paper 5. The idea of the paper is due to Herman Singer and Prof. Jorg Bilgram from ETH, Switzerland, who provided the experimental part of the paper. The respondent worked on the part involving simulations: writing a parallel Finite Difference code and performing large number of two and three dimensional calculations, as well as visualization of the results.

Contents

CHAPTER 1

Introduction

Phase transformations controlled by diffusion are familiar to everyone. The simplest example would be making ice cubes out of water, i.e. solidification of a pure substance. In general, the manufacture of almost every man-made object involves a phase transformation at some stage. In metals, phase transformations lead to different pattern formation; most of them can only be discerned by means of a microscope, after special preparation procedures, e.g. etching.

Compositional and structural inhomogeneities, appearing during processing of materials, may consist of spatially distributed phases of different composition and crystal structures, grains of different orientations, domains of different structural variants, and structural defects. When such inhomogeneities form patterns or have self-repeating shapes, they are referred as microstructures.

In a single phase alloy microstructures can be revealed due to local composition changes, i.e. microsegregation. Microsegregation results because the growing solid is of different composition (usually less rich in solute) than the parent liquid. The redistribution of the excess solute rejected into the liquid depends significantly on the complicated shape of the solid microstructure. Understanding underlying physical processes of microstructural formation is of great technological importance. The size, shape, and spatial arrangement of the local structural features in a microstructure play a critical role in determining the physical properties of materials.

Probably the most fascinating and most studied pattern formation is dendritic structures, which appears in metals and other materials, such as ceramics. Dendrites are also a key element in the neural system of animals and man. The name comes from the highly branched tree-like morphology: the Greek for tree is $'\delta\epsilon\nu\delta\rho o\nu'$ (dendron). Figure 1.1 gives an example of an equiaxed dendritic structure computed in 3 dimensions, other examples on experimentally observed dendrites can be found in Paper 5. In metals, dendrites appear during solidification which begins with nucleation. Once a nucleus has formed, it starts to grow. Usually the interface between solid and liquid becomes unstable and breaks up into a dendritic morphology.

There are several control parameters that can be used to control the growth pattern, for example, the flow. In some industrial applications a homogeneous material is preferred which means that the dendritic structures must be avoided, for example, by applying a forced flow to obtain a less heterogeneous solidified material. In other products, such as high quality turbine blades of super-alloys, the dendrites are forced to grow along the axis of the turbine blade, which results in improved temperature properties of the blades. The dendritic structure is probably

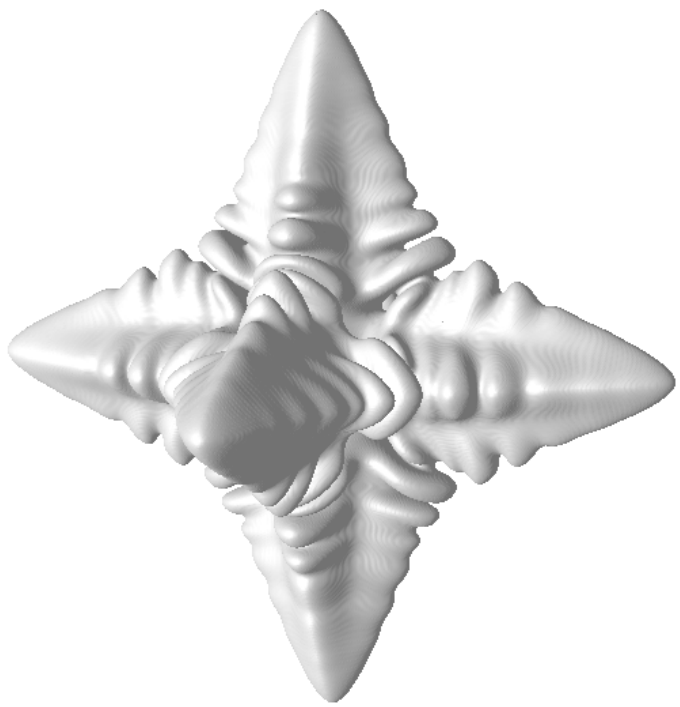

FIGURE 1.1. Solutal dendrite.

the most common crystal structure in metallurgy determining to a high degree the thermal and mechanical properties of solidified materials.

In a casting, there are millions of dendrites forming independently out of solution and subsequently communicating through heat and solutes diffusion. When the dendrites approach each other, they impinge and form grain boundaries. Within each grain the atoms are all aligned, and adjacent grains differ in orientation. The subsequent process when some of the grains shrink and disappear while others grow is called grain growth. Grain growth occurs because of the tendency to reduce the total grain boundary area and thus to reduce the associated surface energy. This allows some grains to grow at the expense of others and hence for the mean grain size to increase with time. The properties of a material are dependent on the size of its grains and therefore it is of interest to gain a better understanding of this process.

Another example of a microstructure is Widmanstätten precipitates. They are plate- or needle-shaped crystals that develop into parent grains from grain boundaries. Widmanstätten plates are regular patterns which can be observed if the parent crystal is sectioned along the direction of growth of plates. An example of the Widmanstätten plates is given in Figure 13 of the Paper 4. The plates were first discovered by Alois von Widmanstätten in the beginning of the 19th century, when he studied the regular crystallographic features visible by the naked eye on etched plane sections of metallic meteorites. Since their discovery, Widmanstätten structures have been found, albeit on a much finer scale, in many artificially prepared

alloys, and perhaps most notably in steels containing less than 0.5% carbon by weight. In these alloys, for certain ranges of parent crystal size and transformation temperature, Widmanstätten plates of low-carbon ferrite grow in parent grains of higher-carbon austenite. Again, ability to control growth of the precipitates is of great interest for materials science.

This thesis concerns modeling of microstructural development of dendrites, grains and Widmanstätten plates. Ideally, microstructure predictions encompass all the scales involved in materials processing, from the atomistic spacing, through dendritic and grain mesoscale, to the macroscopic dimension of the product, with the corresponding timescale differences. However, since computers are not yet capable of achieving this task, modeling of microstructural formation has to be approximated and somehow performed at various levels.

CHAPTER 2

Modeling phase transformations

Diffusion controlled phase transformations considered in this thesis concern two-phase systems of pure substances and binary mixtures. In particular we study solidification where a solid phase grows out of liquid, and solid state transformation where the parent phase is solid. Independent of the transformation's type, the underlying diffusion nature of the processes is the same.

In a classical approach to modeling phase transformation, diffusion equations are formulated in the bulk phases and then boundary conditions are specified on the moving phase interface. As an example, the growth of a single crystal into an undercooled pure melt is classically described by the Stefan problem

$$\begin{cases} \dot{T} &= \alpha \nabla^2 T, & \mathbf{x} \in \Omega_{L,S}(t) \\ L\mathcal{V}_n &= -c\alpha \left[\dfrac{\partial T}{\partial n}\right]_{solid}^{liquid} & \mathbf{x} \in \partial\Omega(t) \\ T &= T_M - \dfrac{\sigma T_M}{L}\mathcal{K} - \dfrac{\mathcal{V}_n}{\mu}, & \mathbf{x} \in \partial\Omega(t) \end{cases} \tag{1}$$

where $\Omega_{L,S}$ are the regions of liquid and solid phases, separated by the interface $\partial\Omega$, T is the system temperature, T_M is the melting temperature, c is the heat capacity, α is the thermal diffusivity, L is the latent heat of fusion, $\mathcal{V}_n$ is the normal velocity of the interface, $\mathcal{K}$ is the interface curvature taken to be positive if the center of curvature lies inside the solid, σ is the surface tension and μ is the interfacial mobility.

The first equation of (1) describes the heat diffusion in the solid and liquid phases. The second equation is the classical Stefan condition, implying that the normal velocity is proportional to the jump in the temperature gradient across the interface. This is the condition of heat conservation at the interface. The Gibbs-Thomson relation (the last equation in (1)) defines the change of the melting temperature at the interface due to capillary and kinetic effects.

When a pure melt is held in a metastable state, i.e. at a temperature below T_M, the solidification can be initiated by a small disturbance of the system, e.g. by introducing a crystal seed. During growth of the crystal the latent heat is released at the interface, and the rate at which the heat is conducted away specifies how rapidly the interface can move. The latent heat is released more rapidly when the growing solid has a large surface area. On the other hand, the interface is associated with a surface energy which would in turn imply that a small interfacial area is desirable. Surface energy has a stabilizing effect on the growth since it determines the smallest scale in the pattern. The actual shape of the crystal is determined by a compromise between these two competing effects [**2, 3**].

In alloys, the diffusion of chemical species controls the motion of the solidification front in a manner analogous to the way the motion is governed by the thermal diffusion in the case of a pure substance. In metals thermal diffusion is much faster than chemical diffusion, thus the chemical effects on the interfacial instabilities are dominant. When the interface advances, the solute is rejected from solid in much the same way as, in the pure thermal case, it releases latent heat, thus governing the interface motion [**2, 3**].

During phase transformations the interface of a growing crystal is a subject to morphological instability. For example, when a bump is formed on a planar solidification front advancing into an undercooled melt, the local temperature gradient ahead of the interface will increase, and thus cool the front more efficiently there, causing an amplification of the disturbance. The basic morphological instability of a planar and spherical front was first investigated by Mullins and Sekerka [**4, 5**]. It was demonstrated that a perturbation of the planar interface will grow if its wave length is greater than the marginally stable wavelength defined by the material properties and growth conditions. The stability analysis has been applied extensively in different contexts, for example under rapid solidification conditions [**6**] and in the case of anisotropic surface tension and interface kinetics [**7**].

In spite of the apparent simplicity of the Stefan problem (1) analytical solutions are known only for a few special cases in a simple geometry, e.g. planar fronts. Ivantsov [**1**] found an analytical solution of (1) for a paraboloid of revolution, representing the shape of an isothermal dendrite tip advancing with a steady-state velocity into a pure undercooled melt. In the absence of capillary and kinetic effects, the Ivantsov solution is formulated in terms of Peclet number (product of the tip velocity and radius). However, these quantities can not be defined separately from the Ivantsov solution. The remedy for solving complicated models of the phase transformation is thus numerical computations which are discussed in the coming sections.

2.1. The sharp-interface method

Direct numerical simulations of crystal growth, e.g. solving the Stefan problem, involve explicit tracking of the phase boundary, since its location and shape are parts of the solution itself. In the front tracking methods, the interface is represented by a surface mesh, while the thermal and velocity fields are discretized on another mesh, a base-mesh. The time-dependent problem is then solved by advecting the surface mesh according to the velocity condition in eq.(1), and solving the heat equation in the solid and liquid given the location of the interface and using the Gibbs-Thomson relation as the boundary condition.

In [**23**] an approach based on the immersed boundary method is used to transfer data between a fixed temperature grid and interfaces. The position of the interface is updated by using the kinetic term in the Gibbs-Thomson equation. A different algorithm is implemented by Almgren [**24**], where the surface mesh is advected by minimizing an energy function chosen such that the Gibbs-Thomson condition holds. Impressive simulations of 3 dimensional dendritic growth of a pure material with the sharp-interface method were done by Schmidt [**25**]. A combination of a front tracking technique and FEM results in a method with impressively low

demands of computer resources. In the method, both the surface mesh and the base-mesh are adaptively changed according to a post-error estimation. Though this method seems to be very attractive, it requires a lot of administration, because the surface mesh must be re-mapped and adjusted at each time step to prevent degeneration of the mesh elements.

The complicated interfacial patterns arising during phase transformation, e.g. dendrites, require adjustment of the surface meshes. Merging and splitting of the interfaces are inherently difficult, since it becomes necessary to redefine mesh connectivity to represent the new geometry. This difficulty increases significantly with number of space dimensions.

2.2. The level-set method

In the level-set method [**26, 27, 28**] the problem of explicit front tracking is avoided by introducing an extra field variable $\psi(\mathbf{x}, t)$, which is a signed distance function, or level-set function. For every point in the domain, the level-set function gives the distance to the closest phase interface, defined as the zero level-set. The evolution of the level-set function is governed by the advection equation

$$\dot{\psi} = -\vec{V} \cdot \nabla\psi \tag{2}$$

where $\vec{V}$ is the interface velocity, obtained through the Stefan condition. The temperature is updated in the bulk phases and special temperature interpolants are constructed at the solid/liquid interface to satisfy the Gibbs-Thomson condition. The benefit of the level-set method is that it is independent of the width of the diffuse interface introduced in the phase-field method. Simulations are performed using the sharp interface formulation. The inherent problem with the level-set method is that eq.(2) does not preserve the distance property of the level-set function and a reinitialization procedure must be performed after every interface update. Another problem is extrapolation of the interface velocity into the bulk phases. These technical difficulties reduce the attractiveness of the method for simulating dendritic growth.

2.3. The phase-field method

In the phase-field method the interface between two phases is treated as a region of finite width, where different state variables have gradual variations, i.e. phase-field method employs the diffuse interface model. An auxiliary variable, phase-field or order parameter $\phi(\mathbf{x}, t)$, is introduced into the model to indicate the state of the system at every point. The phase-field variable keeps a constant value in the bulk phases (e.g. $\phi = 0$ in liquid and $\phi = 1$ in solid) and varies smoothly but rapidly over the phase boundary.

An evolution equation for ϕ and the transport equations are derived thermodynamically for the whole system, without distinguishing between the phases. The thermodynamic and kinetic coefficients entering the model are chosen to match the corresponding parameters in conventional sharp interface equations through asymptotic analysis.

The indisputable computational advantage of the phase-field methods is avoiding explicit front-tracking of the phase boundary. In combination with relative simplicity of solving phase-field equations numerically, this makes the method extremely attractive for modeling microstructural evolution in the materials science community. However, the phase-field method is not only a mathematical tool for avoiding front tracking. Its underlying diffuse interface nature is directly linked to the thermodynamics of phase transformations. In contrast to the sharp-interface method, non-equilibrium effects at the phase boundary are included into the phase-field models automatically.

An overview of the phase-field method and its derivation are given in the following chapters.

CHAPTER 3

The phase-field method

In this chapter literature on the phase-field modeling that is the most important and relevant to the thesis is reviewed. Detailed summaries on modeling microstructural evolution by the phase-field methods can be found in the extensive reviews [**18, 19, 20**]

3.1. Solidification of pure materials

The phase-field equations originate in the works of Cahn and Hilliard [**9**] on the free energy of nonuniform systems and Allen and Cahn [**8**] on an antiphase boundary motion. Early works on phase-field methods investigate dendritic solidification of pure materials. Langer [**10**] and Fix [**11**] were first to introduce a phase-field model for first-order phase transition. A similar diffuse interface model for solidification was independently written by Collins and Levin [**12**]. Significant early work on development and analysis of the phase-field models, including effects of anisotropy, was done by Caginalp et al [**13, 14**]. The computations of Kobayashi [**21, 22**] in 3 dimensions demonstrated the potential of the phase-field approach as a computational tool for modeling complicated, realistically looking dendritic structures. His work generated considerable interest in the material science community for the phase-field method.

Wang et al [**29**] put derivation of the phase-field models on a thermodynamically consistent basis. General conditions were developed to ensure that the phase-field variable takes on constant values in the bulk phases. Wheeler et al [**30**] performed an asymptotic analysis of the phase-field model to recover the classical free boundary problem in the limit when the interface thickness vanishes. Nowadays this analysis is often referred in the literature as the sharp-interface limit.

The phase-field model proposed in [**30**] was extensively used [**31, 32**] to study the dendritic growth and to compare its different aspects to experimental observations. In particular, cleaving phenomenon was simulated in 2 dimensions [**31**], which includes splitting of the dendrite tip into two branches and subsequent predominant growth of one of them.

Despite the success of simulating realistically looking dendrites, early simulations were limited to high undercooling rates. Karma and Rappel [**33**] proposed a phase-field model where parameters could be adjusted to eliminate interface kinetics, thus allowing to perform simulations at low undercoolings. Moreover, in their thin-interface asymptotic limit, the interface thickness could be the order of the capillary length in order to produce accurate results, while in the previous models it must be much less than the capillary length. Quantitative phase-field simulations of free equiaxed dendritic growth have been carried out in 3 dimensions by

Karma [**34**] at low undercooling and by Bragard [**35**] at high undercooling with the incorporation of anisotropic interface kinetic effects. For the high undercoolings, the phase-field simulations were performed using as an input interfacial properties computed from atomistic molecular dynamics simulations.

3.2. Binary alloy solidification

The growth of a crystal from an alloy melt results in a local change in the composition over the phase change boundary. This is because the equilibrium condition for a binary system requires continuity of chemical potentials of the components at the phase boundary. A typical concentration profile is shown in Figure 3.1. The composition has a rather constant value in the growing phase, jumps across the interface and then relaxes to its far-field value c_∞ in the parent phase. The difference in composition at the moving interface, assuming local thermodynamic equilibrium under normal solidification conditions, can be described by the partition coefficient

$$k = \frac{c_S}{c_L} \tag{3}$$

where c_S and c_L are concentration of solute at the solid and liquid sides of the interface, respectively. The values of c_S and c_L for a given temperature can be obtained through a phase diagram (Figure 4.1), whose derivation is described in details in Section 4.2. Under rapid solidification conditions k may become a function on the interface velocity $\mathcal{V}$.

Langer and Sekerka [**15**] considered a model of diffuse interface motion in a binary alloy system with a miscibility gap in a solid solution phase. Caginalp et al [**16**] studied solidification of a binary mixture by the phase-field method. They showed that the phase-field equations reduce to the traditional sharp interface models in the limit when the thickness of the interfacial region δ is taken to zero.

Wheeler et al [**36, 37**] and Boettinger et al [**38**] presented a model that includes gradient energy contributions for the phase-field and for the composition field. They studied interface velocity dependence on the solute profiles. While at low solidification rates equilibrium behavior was recovered, at high solidification rates non-equilibrium effects such as solute trapping naturally emerged from the model. By solute trapping one understands the velocity dependence of the jump in concentration which provides a mechanism whereby the jump vanishes at high rates of solidification leading to a partitionless transformation. In the subsequent work [**39**] Ahmad et al showed that solute trapping occurs when the solute diffusion length $D_I/\mathcal{V}$ is comparable to the diffuse interface thickness, where D_I is a characteristic solute diffusivity in the interfacial region. Loginova et al [**40**] (Paper 3) investigated the transition between diffusion controlled and massive transformation $\gamma \to \alpha$ in Fe-C alloys. The solute trapping was observed when far-field composition of Austenite was below a critical value for a given temperature. In this case the solute profile comprises a spike traveling with constant velocity; the variation of the composition occurs inside the diffuse interface.

Warren and Boettinger [**41**] derived a phase-field model for isothermal solidification of a binary alloy, applying constant diffusivities within the solid and liquid

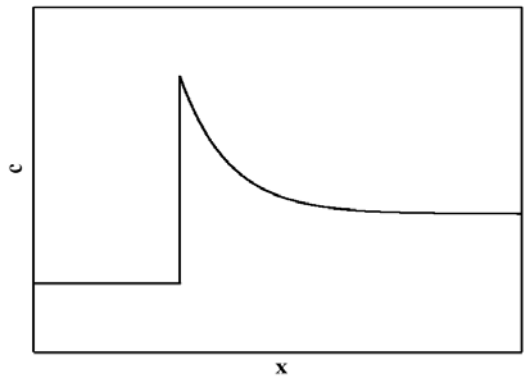

FIGURE 3.1. Sketch of the concentration distribution in a binary alloy.

phases, and performed 2D simulations of dendritic growth into a highly supersaturated liquid. This model has also been used to study directional solidification at high velocities [**43**], solidification during recalescence [**42**], Ostwald ripening and coalescence [**44**]. A desirable extension of the isothermal model is to study the effect of heat flow due to release of latent heat. Inclusion of heat flow effect due to release of latent heat represents a severe numerical problem since the temperature and solute evolution occurs on completely different time-scales. A simplified approach was proposed in [**42**], where the spatial variation of the temperature is neglected and the heat equation is replaced by a heat balance of an imposed heat extraction rate and the latent heat release rate.

Bi and Sekerka [**45**] proposed a general phase-field model for binary alloy solidification which included energy gradients of phase-field, concentration and internal energy. Loginova et al [**46**] (Paper 1) derived a model for simultaneous heat and solute evolution. The inherent difficulty of different time-scales was circumvented by applying adaptive grids and implicit time-stepping schemes. It was demonstrated that at high cooling rates the supersaturation is replaced by the thermal undercooling as the driving force for growth. Even though realistic microstructural patterns were obtained in [**41, 46**], the models still exhibit interface thickness dependent results and presence of solute trapping.

Recently Karma [**47**] re-examined existing phase-field models for binary alloys in the thin-interface limit. He demonstrated presence of solute trapping in the low growth regime due to the jump of chemical potential across the interface. He proposed a new model which includes a so-called "anti-trapping" term which yields the same computational benefits as the thin-interface limit of the symmetric model (i.e. with equal diffusion coefficients in liquid and solid) for dendritic growth of pure substances [**33**]. Ramirez and Beckermann [**48**] extended [**47**] to a non-isothermal case and demonstrated good agreement with simple analytical solutions. Thermosolutal dendritic growth was simulated in 2 dimensions for equal heat and solute diffusivities. However, their model leads to inaccurate results when the diffusivities differ significantly.

3.3. Grain growth

Both solidification and solid-solid phase transformations take place to reduce the bulk free energy, whereas coarsening and grain growth are driven by reduction in the free energy associated with a decrease in the total grain boundary area. Chen and Yang [**49**] proposed a model for describing grain growth, in which the grains of different orientations are represented by a set of nonconserved order parameter fields. Assigning N order parameters to the N allowed orientations, they simulated grain growth kinetics in 2 and 3 dimensions [**49, 51**]. A similar multiorder parameter model, the so-called multiphase-field model, for grain growth was proposed by Steinbach et al [**50**]. In this model, a special constraint is imposed, requiring that the sum of all order parameters in every point must be 1, which implies that the order parameters represent the volume fraction of grains of different orientations.

Recently, Kobayashi et al [**52, 53**] proposed a new phase-field model to study the crystalline grains. Different from multiorder parameter models for grain growth, it uses two order parameters to describe a grain structure: one represents the crystalline order, the other reflects the crystalline orientation of the crystal. Whereas the relaxation of the crystalline orientation parameter simulates the grain rotation, which is absent in the multiorder parameter models, this order parameter is undefined in a disordered liquid phase. The main property of the model is invariance under rotation of the reference frame, the property which earlier models [**49, 50**] have lacked. The authors extended the model [**54, 55, 56**] to simulate simultaneous processes of solidification, impingement of arbitrary oriented crystals and consequent coarsening. Based on [**52, 53**] Gránásy et al [**57, 58**] proposed a model for nucleation and growth of multiple particles in binary alloys. Warren et al [**59**] (Paper 2) simulated complex solidification processes which occur when many crystallites grow independently out of solution communicating through the diffusion field. The simulations demonstrate impingement of particles, grain boundary formation, coarsening and grain growth.

3.4. Other applications

There has been an extensive study of the effect of fluid flow on dendritic growth of pure substances. It was shown that due to natural convection [**60**] and forced flow [**76, 77, 78, 80**] the dendrite tip pointed into the flow grows at a much faster velocity than the other tips. Eutectic and peritectic morphologies have been successfully modeled by means of the multiphase-field method [**84, 85, 86**]. Recently, the phase-field models for multicomponent alloys were reported [**63**]. In the area of solid state phase transformation the following phenomena were considered: martensitic transformations in single and polycrystals [**88**], phase transformations under applied stress [**89**] and ferroelastic transformations [**90**]. Morphological pattern formation in thin films and on surfaces were studied by a number of investigators [**91, 92**]. Among the latest applications of the phase-field method are crack propagation [**93**] and electrochemistry [**94**].

CHAPTER 4

Derivation of the phase-field method

4.1. Derivation of phase-field models

There are different approaches to phase-field modeling of diffusion controlled phase transformation. In this chapter we examine a thermodynamical treatment based on an entropy functional and a geometrical method where the equations are derived backward from the sharp interface method.

4.1.1. Thermodynamically consistent derivation. This approach is found in many papers on the phase-field method [**29, 30, 31, 41, 46, 62**]. The derivation of the evolution equations is based on basic concepts of irreversible thermodynamics. Here we present a rather general derivation of a binary alloy solidification following the work of Bi and Sekerka [**45**].

We first postulate a general form of an entropy functional over the system volume V

$$S = \int_V \left(s(\phi, X, e) - \frac{\varepsilon_\phi^2}{2}|\nabla\phi|^2 - \frac{\varepsilon_X^2}{2}|\nabla X|^2 - \frac{\varepsilon_e^2}{2}|\nabla e|^2 \right) dV \tag{4}$$

where the thermodynamic entropy density s is a function of the phase-field variable ϕ, the concentration X of a solute B in solvent A and the internal energy e. The entropy functional contains the gradient energy terms associated with the formation of an interface. The parameters ε_X, ε_e and ε_ϕ are constants.

The internal energy and mole fraction are conserved quantities, their evolution is governed by the normal conservation laws

$$\dot{X} + \nabla \cdot \mathbf{J}_X = 0 \tag{5}$$

$$\dot{e} + \nabla \cdot \mathbf{J}_e = 0 \tag{6}$$

Consistent with the second law of thermodynamics, we postulate that the local entropy production is a non-negative quantity. This can be achieved by adopting the following linear laws of irreversible thermodynamics for the diffusional and heat fluxes

$$\mathbf{J}_e = M_{ee}\nabla\left(\frac{\delta s}{\delta e}\right) + M_{eX}\nabla\left(\frac{\delta s}{\delta X}\right) \tag{7}$$

$$\mathbf{J}_X = M_{XX}\nabla\left(\frac{\delta s}{\delta X}\right) + M_{Xe}\nabla\left(\frac{\delta s}{\delta e}\right) \tag{8}$$

where M_{XX} and M_{ee} are related to the inter-diffusional mobility of B and A and the heat conduction, respectively. The second law requires M_{ee} and M_{XX} to be positive. The coefficients M_{eX} and M_{Xe} describe the cross effects between the heat

flow and diffusion and are equal according to the Onsager's reciprocal theorem. It should be emphasized that the gradients $\nabla(\delta s/\delta X)$ and $\nabla(\delta s/\delta e)$ are to be evaluated isothermally and under fixed composition, respectively. Since there are gradient terms of X and e in the entropy functional (4), the variational derivatives in eq.(7) and (8) are given by

$$\frac{\delta s}{\delta e} = \frac{\partial s}{\partial e} + \varepsilon_e^2 \nabla^2 e \tag{9}$$

$$\frac{\delta s}{\delta X} = \frac{\partial s}{\partial X} + \varepsilon_X^2 \nabla^2 X \tag{10}$$

The phase-field variable is a non-conservative quantity, therefore to guarantee that the entropy increases, a special relationship is derived

$$\dot{\phi} = M_\phi \frac{\delta s}{\delta \phi} = M_\phi \left(\frac{\partial s}{\partial \phi} + \varepsilon_\phi^2 \nabla \phi \right) \tag{11}$$

where M_ϕ is a positive mobility related to the kinetic coefficient. Eq.(11) is often called Allen-Cahn equation [**8**].

For the case of a regular solution, the energy density and the entropy density can be written in the form

$$e(T, X, \phi) = e_A(T, \phi)(1 - X) + e_B(T, \phi)X + \Omega(\phi)X(1 - X) \tag{12}$$

$$s\left(e(T, X, \phi)\right) = s_A(T, \phi)(1 - X) + s_B(T, \phi)X - \frac{R}{V_m}\left[X \ln X + (1 - X)\ln(1 - X)\right] \tag{13}$$

where e_A and e_B are the energy densities of the pure components, s_A and s_B are their entropy densities, $\Omega(\phi)$ is a thermodynamic constant associated with the enthalpy of mixing, T is temperature, R is the ideal gas constant and V_m is the molar volume, taken as a constant. We postulate the energy density of a pure material according to [**29**]

$$e_A(T, \phi) = e_A^S(T)(1 - p(\phi)) + e_A^L(T)p(\phi) \tag{14}$$

where e_A^L and e_A^S are energy densities for the liquid and solid phases, respectively, and $p(\phi)$ is an interpolating function which satisfies $p(0) = 0$ and $p(1) = 1$. The entropy density s_A then can be found by integrating $ds_A = de_A/T$ over temperature at constant ϕ

$$s_A(T, \phi) = (1 - p(\phi)) \int_0^T c_A^S(u) \frac{du}{u} + p(\phi) \int_0^T c_A^L(u) \frac{du}{u} + K_A(\phi) \tag{15}$$

where $c_A^S(T)$ and $c_A^L(T)$ are the specific heats of the liquid and solid phases, respectively, and $K_A(\phi)$ is an integration constant obeying $K_A(0) = K_A(1)$ according to the third law of thermodynamics. The corresponding relations for the component B can be obtained by replacing the subscript A by B.

Helmholz free energy density is constructed using eq. (12) and (13)

$$\begin{aligned} f(T,X,\phi) &= e(T,X,\phi) - Ts\left(e(T,X,\phi),X,\phi\right) \\ &= f_A(T,\phi)(1-X) + f_B(T,\phi)X + \Omega(\phi)X(1-X) \\ &+ \frac{RT}{V_m}\left[X\ln X + (1-X)\ln(1-X)\right] \end{aligned} \tag{16}$$

where

$$f_{A,B}(T,\phi) = e_{A,B}(T,\phi) - Ts_{A,B}(T,\phi) \tag{17}$$

are the free energy densities of pure A and B. Substituting (14) and (15) into (17) yields an explicit expression for f_A

$$f_A(T,\phi) = f_A^S(T,\phi)(1-p(\phi)) + f_A^L(T,\phi)p(\phi) - TK_A(\phi) \tag{18}$$

where

$$f_A^{L,S}(T,\phi) = e_A^{L,S}(T) - T\int_0^T c_A^{L,S}(u)\frac{du}{u} \tag{19}$$

with a similar expression for f_B.

In order to apply the evolution equations (5),(6) and (11) we need to evaluate the driving forces for the phase transformation. Namely, we need to calculate $\nabla\left(\partial s/\partial e\right)_{X,\phi}$, $\nabla\left(\partial s/\partial X\right)_{e,\phi}$ and $\left(\partial s/\partial\phi\right)_{e,X}$ terms in the eq.(9), (10) and (11). By first noting that

$$de = Tds + \left(\frac{\partial e}{\partial X}\right)_{s,\phi} dX + \left(\frac{\partial e}{\partial \phi}\right)_{s,\phi} d\phi \tag{20}$$

we obtain

$$\nabla\left(\frac{\partial s}{\partial e}\right)_{X,\phi} = \nabla\frac{1}{T} = -\frac{1}{T^2}\nabla T \tag{21}$$

Furthermore, we use

$$df = -sdT + \left(\frac{\partial e}{\partial X}\right)_{s,\phi} dX + \left(\frac{\partial e}{\partial \phi}\right)_{s,\phi} d\phi \tag{22}$$

to recognize

$$\left(\frac{\partial s}{\partial X}\right)_{e,\phi} = -\frac{1}{T}\left(\frac{\partial e}{\partial X}\right)_{s,\phi} = -\frac{1}{T}\left(\frac{\partial f}{\partial X}\right)_{T,\phi} \tag{23}$$

$$\left(\frac{\partial s}{\partial \phi}\right)_{e,X} = -\frac{1}{T}\left(\frac{\partial e}{\partial \phi}\right)_{s,X} = -\frac{1}{T}\left(\frac{\partial f}{\partial \phi}\right)_{T,X} \tag{24}$$

In order to evaluate $\nabla\left(\partial s/\partial X\right)_{e,\phi}$ we first write

$$\nabla\left(\frac{\partial s}{\partial X}\right)_{e,\phi} = \frac{\partial}{\partial\phi}\left(\frac{\partial s}{\partial X}\right)_{e,\phi}\nabla\phi + \frac{\partial}{\partial X}\left(\frac{\partial s}{\partial X}\right)_{e,\phi}\nabla X \tag{25}$$

next, we calculate the second derivatives

$$\frac{\partial}{\partial\phi}\left(\frac{\partial s}{\partial X}\right)_{e,\phi} = -\frac{1}{T}\frac{\partial^2 f}{\partial\phi\partial X} = H_A(T,\phi) - H_B(T,\phi) - \frac{1}{T}\frac{d\Omega(\phi)}{d\phi}(1-2X) \tag{26}$$

$$\frac{\partial}{\partial X}\left(\frac{\partial s}{\partial X}\right)_{e,\phi} = -\frac{1}{T}\left(\frac{\partial^2 f}{\partial X^2}\right)_{T,\phi} = -\frac{R}{V_m}\frac{1}{X(1-X)} + \frac{2}{T}\Omega(\phi) \tag{27}$$

where the following notations were introduced

$$H_{A,B}(T,\phi) = \frac{1}{T}\frac{\partial f_{A,B}(T,\phi)}{\partial \phi} \tag{28}$$

Substituting eqs.(26) and (27) into (25) gives

$$\begin{aligned} \nabla\left(\frac{\partial s}{\partial X}\right)_{e,\phi} &= \left[H_A(T,\phi) - H_B(T,\phi) - \frac{1}{T}\frac{d\Omega(\phi)}{d\phi}(1-2X)\right]\nabla\phi \\ &+ \left[-\frac{R}{V_m}\frac{1}{X(1-X)} + \frac{2}{T}\Omega(\phi)\right]\nabla X \end{aligned} \tag{29}$$

And finally, the term in eq.(11) is given by

$$\begin{aligned} \left(\frac{\partial s}{\partial \phi}\right)_{e,X} &= -\frac{1}{T}\left(\frac{\partial f}{\partial \phi}\right)_{T,X} \\ &= -H_A(T,\phi)(1-X) - H_B(T,\phi)X - \frac{1}{T}\frac{d\Omega(\phi)}{d\phi}X(1-X) \end{aligned} \tag{30}$$

The general phase-field equations for a binary alloy solidification can be obtained by substituting expressions for the fluxes into eq.(9), (10) and (11). Here we present a simplified version under the commonly used assumptions $\varepsilon_e = \varepsilon_X = 0$ and $M_{eX} = M_{Xe} = 0$

$$\left\{\begin{aligned} \dot{\phi} &= M_\phi\left[\varepsilon_\phi^2\nabla^2\phi - H_A(T,\phi)(1-X) - H_B(T,\phi)X - \frac{1}{T}\frac{d\Omega}{d\phi}X(1-X)\right] \\ \dot{X} &= \nabla\cdot\left[M_{XX}\left(\frac{R}{V_m}\frac{1}{X(1-X)} - \frac{2}{T}\Omega(\phi)\right)\nabla X\right] \\ &+ \nabla\cdot\left[M_{XX}\left(H_B(T,\phi) - H_A(T,\phi) + \frac{1}{T}\frac{d\Omega}{d\phi}(1-2X)\right)\nabla\phi\right] \\ \frac{\partial e}{\partial T}\dot{T} &+ \frac{\partial e}{\partial \phi}\dot{\phi} + \frac{\partial e}{\partial X}\dot{X} = \nabla\cdot\left[\frac{M_{ee}}{T^2}\nabla T\right] \end{aligned}\right. \tag{31}$$

4.1.2. Reduction to the isothermal model [41]. From the derived model, several existing phase-field models can be recovered under certain assumptions. For example, a model of a pure substance by Wang et al [**29**] can be obtained if $X = 0$. In this section we recover Warren and Boettinger's model [**41**] for isothermal binary alloy solidification. They assumed an ideal behavior of the solution, i.e. $\Omega(\phi) = 0$, so that phase-field and diffusion equations in (31) become equivalent to eq.(3.2) and (3.6) in [**41**]. In order to continue, we evaluate $H_{A,B}$ explicitly using expression (18) for the free energy

$$H_A = p'(\phi)\frac{f_A^L(T) - f_A^S(T)}{T} - K_A'(\phi) \tag{32}$$

Since we are interested in temperatures near the melting point T_M, we can avoid integration from absolute zero (as in eq.(19)) by integrating of $d(f_A/T)/d(1/T) = e_A$ to obtain

$$\frac{f_A^L(T) - f_A^S(T)}{T} = -\int_{T_M}^{T} \frac{L_A(u)}{u^2} du \tag{33}$$

where we have used $f_A^L(T_M) = f_A^S(T_M)$ and defined $L_A(T) = e_A^L(T) - e_A^S(T)$. Thus, $L_A(T_M)$ is just the latent heat (per unit volume) of A. To proceed further, we need to specify the energies $e_A^L(T)$ and $e_A^S(T)$. For Ni-Cu alloy considered in [**41**] one may assume that the heat capacity for the pure, single-phase materials, is constant and that $c_A^L = c_A^S$. Then

$$e_A^L(T) = e_A^L(T_M) + c_A^L(T - T_M^A) \tag{34}$$

$$e_A^S(T) = e_A^S(T_M) + c_A^S(T - T_M^A) \tag{35}$$

which gives $e_A^L(T) - e_A^S(T) = e_A^L(T_M) - e_A^S(T_M) = L_A$ and

$$H_A(T, \phi) = p'(\phi) L_A \int_{T_M}^{T} \frac{1}{u^2} du - K_A'(\phi) = p'(\phi) L_A \left(\frac{1}{T} - \frac{1}{T_M^A} \right) - K_A'(\phi) \tag{36}$$

Choosing the interpolation function $p(\phi) = \phi^3(6\phi^2 - 15\phi + 10)$ and $K_A(\phi)$ as a double well potential $K_A(\phi) = -W_A g(\phi)$, $g(\phi) = \phi^2(1-\phi)^2$, where W_A is the energy hump between the free energies of the liquid and solid, we obtain

$$H_A = W_A g'(\phi) + 30 g(\phi) L_A \left(\frac{1}{T} - \frac{1}{T_M^A} \right) \tag{37}$$

and similarly for B

$$H_B = W_B g'(\phi) + 30 g(\phi) L_B \left(\frac{1}{T} - \frac{1}{T_M^B} \right) \tag{38}$$

In the expressions above T_M^A and T_M^B are the melting temperature of the pure A and B and we accounted that $p'(\phi) = 30 g(\phi)$. Equations (37) and (38) are exactly the same as eq.(3.3) in [**41**]. Taking the parameter $M_{XX} = V_m D(\phi) X(1-X)/R$, where $D(\phi)$ is the diffusion coefficient, we fully recover the Warren-Boettinger's model [**41**] for the isothermal solidification of Ni-Cu alloy.

4.1.3. Geometrical description. Beckerman et al [**61**] presented a simple geometrically motivated derivation of the phase-field equations for a binary alloy starting from the phenomenological Gibbs-Thomson interface relation

$$\frac{\mathcal{V}_n}{\mu_A} = T_M^A - T + m_L c_L - \Gamma \mathcal{K} \tag{39}$$

where μ_A is the linear kinetic coefficient, m_L is the liquidus slope from an equilibrium phase diagram and Γ is the Gibbs-Thomson coefficient. If one considers the interface as represented by a constant value of ϕ, the normal $\vec{n}$ to the interface and the curvature $\mathcal{K}$ can be evaluated as follows

$$\vec{n} = \frac{\nabla \phi}{|\nabla \phi|} \tag{40}$$

$$\mathcal{K} = \nabla \cdot \vec{n} = \frac{1}{|\nabla\phi|}\left[\nabla^2\phi - \frac{\nabla\phi\cdot\nabla|\nabla\phi|}{|\nabla\phi|}\right] \tag{41}$$

The normal velocity of the interface is given by

$$\mathcal{V}_n = \frac{1}{|\nabla\phi|}\frac{\partial\phi}{\partial t} \tag{42}$$

Substituting eq.(41) and (42) into the Gibbs-Thomson condition (39) yields

$$\frac{1}{\mu_A}\frac{\partial\phi}{\partial t} = \Gamma\left[\nabla^2\phi - \frac{\nabla\phi\cdot\nabla|\nabla\phi|}{|\nabla\phi|}\right] + \left(T_M^A - T + m_L c_L\right)|\nabla\phi| \tag{43}$$

A variation of ϕ in the normal direction across the interface can be obtained as a steady state solution of eq.(43) (more details are given in Section 4.2)

$$\phi = \frac{1}{2}\left(1 + \tanh\frac{n}{2\delta}\right) \tag{44}$$

where n is the coordinate normal to the interface and δ specifies the width of the diffuse interface. Using eq.(44) one can compute

$$|\nabla\phi| = \frac{\partial\phi}{\partial n} = \frac{\phi(1-\phi)}{\delta} \tag{45}$$

$$\frac{\nabla\phi\cdot\nabla|\nabla\phi|}{|\nabla\phi|} = \frac{\partial^2\phi}{\partial n^2} = \frac{\phi(1-\phi)(1-2\phi)}{\delta^2} \tag{46}$$

Substituting eq.(45) and (46) into eq.(43) results in the phase-field equation

$$\frac{1}{\mu_A}\frac{\partial\phi}{\partial t} = \Gamma\left[\nabla^2\phi - \frac{\phi(1-\phi)(1-2\phi)}{\delta^2}\right] + \left(T_M^A - T + m_L X_L\right)\frac{\phi(1-\phi)}{\delta} \tag{47}$$

Finally, the diffusion equation can be derived by using phase-field weighted values for the average concentration

$$\frac{\partial X}{\partial t} = \nabla\cdot\left[(1-\phi)D_S\nabla X_S + \phi D_L\nabla X_L\right] \tag{48}$$

where the phase concentrations can be expressed in terms of average mixture concentration

$$X_L = \frac{X}{\phi + k(1-\phi)} \tag{49}$$

and

$$X_S = \frac{kX}{\phi + k(1-\phi)} \tag{50}$$

where k is the solute partition coefficient. We shall notice that in the method only the values of T_M^A, m_L and k are required. Even though this derivation is not mathematically strict, it does provide a sense of the relationship between terms in the phase-field equation and quantities like the interface curvature and velocity.

4.2. The equilibrium phase diagram

In most analysis of alloy solidification, it is assumed that the solid/liquid interface behaves locally as if it were in a state of equilibrium. This means that the reaction rates, in the small volume which makes up the very thin but finite interface layer, are expected to be rapid in comparison with the rate of interface advance. As a result, the transfer of atoms and changes in their arrangement, which are required in order to maintain the continuity of the chemical potentials in both phases, are relatively rapid and can be neglected. The assumption of local equilibrium means that, if the interface temperature is known, then one can obtain the liquid and solid compositions at the interface by reference to the equilibrium phase diagram (Kurz and Fisher, [**3**]).

In this section we demonstrate a derivation of the equilibrium phase diagram for Ni-Cu alloy from the phase-field model of Warren and Boettinger [**41**]. The phase-field equations nondimensionalized with a characteristic length l and a diffusion time l^2/D are given by

$$\left\{\begin{array}{rcl} \dot{\phi} & = & M_\phi \left[\varepsilon_\phi^2 \nabla^2 \phi - H_A(T,\phi)(1-X) - H_B(T,\phi)X\right] \\ \dot{X} & = & \nabla \cdot \left[\nabla X + \dfrac{V_m}{R} X(1-X)(H_B(T,\phi) - H_A(T,\phi))\nabla\phi\right] \end{array}\right. \tag{51}$$

with the phase-field parameters

$$M_\phi = \frac{(T_m^A)^2 \beta_A d_0^2}{6\sqrt{2}\sigma_A D}\delta = \tilde{M}_\phi \delta \tag{52}$$

$$\varepsilon^2 = \frac{6\sqrt{2}L_A}{T_m^A}\frac{1}{\delta} = \frac{\tilde{\varepsilon}^2}{\delta} \tag{53}$$

$$W_{A,B} = \frac{3L_A}{\sqrt{2}T_m^A}\frac{1}{\delta} = \frac{\tilde{W}_{A,B}}{\delta} \tag{54}$$

where β_A is the kinetic coefficient, σ_A is the surface energy of pure A and d_0 is the capillary length. The parameter $\delta = l/d_0$ is a non-dimensional interface thickness.

We now apply an asymptotic analysis for $\delta \to 0$ proposed by Caginalp and Xie, [**62**]. We consider a stationary one-dimensional interface and introduce z to be the coordinate which measures the distance to the interface, i.e. $\phi = 1/2$. Then the equations (51) can be presented as

$$0 = \frac{d}{dz}\left[X(1-X)\frac{d}{dz}\left(\ln\frac{X}{1-X} + (W_B - W_A)g(\phi) + p(\phi)(A_B(T) - A_A(T))\right)\right] \tag{55}$$

$$0 = M_\phi\left[\varepsilon^2\frac{d^2\phi}{dz^2} - (1-X)H_A(\phi,T) - XH_B(\phi,T)\right] \tag{56}$$

where we introduced the following functions:

$$A_A(T) = \frac{V_m L_A}{R}\left(\frac{1}{T} - \frac{1}{T_m^A}\right),\ A_B(T) = \frac{V_m L_B}{R}\left(\frac{1}{T} - \frac{1}{T_m^B}\right) \tag{57}$$

We seek a solution in the form of an asymptotic expansion in powers of the small parameter δ:

$$\begin{aligned} \phi &= \phi^0 + \delta\phi^1 + \delta^2\phi^2 + ... \\ X &= X^0 + \delta X^1 + \delta^2 X^2 + ... \end{aligned} \tag{58}$$

Taking into account the dependence of the parameters on the interface thickness δ, the phase-field equation (56) can be written as

$$0 = \tilde{M}_\phi \left[\tilde{\varepsilon}^2\phi_{zz} - \tilde{W}_A g'(\phi) - \delta\left((1-X)A_A + XA_B\right)30g(\phi)\right] \tag{59}$$

Substituting (58) into (59) and formally equating terms with equal powers of δ lead to the $O(1)$ equation

$$0 = \tilde{M}_\phi(\tilde{\varepsilon}^2\phi^0_{zz} - \tilde{W}_A(2\phi^0 - 6{\phi^0}^2 + 4{\phi^0}^3)) \tag{60}$$

It is known that this equation has a solution

$$\phi^0(z) = 0.5\left(1 + \tanh\frac{z}{2\sqrt{2}}\right) \tag{61}$$

assuming solid on the left ($\phi(-\infty) = 0$) and liquid on the right ($\phi(\infty) = 1$). For stationary profiles, the diffusion equation (55) gives

$$\int_{-\infty}^{\infty} \frac{d}{dz}\left(\ln\frac{X}{1-X} + p(\phi)(A_B(T^0) - A_B(T^0))\right)dz = 0 \tag{62}$$

where T^0 is independent of z. Evaluation of the integral results in

$$\left[\ln\frac{X}{1-X}\right]_{solid}^{liquid} = A_A(T) - A_B(T) = \frac{V_m}{R}\left(L_A\left(\frac{1}{T} - \frac{1}{T_m^A}\right) - L_B\left(\frac{1}{T} - \frac{1}{T_m^B}\right)\right) \tag{63}$$

Hence, we obtained the first relation for the solid and liquid compositions and temperature. The second relation is calculated through the phase-field equation. Subtracting (60) from (59) and collecting terms, which contain δ yields

$$\mathcal{L} \equiv \tilde{\varepsilon}^2\phi^1_{zz} - \tilde{W}_A(2 - 12\phi^0 + 12{\phi^0}^2)\phi^1 = 30g(\phi^0)((1-X^0)A_A + X^0A_B) \equiv H \tag{64}$$

Since ϕ^0_z is a solution to the homogeneous equation $\mathcal{L}\psi = 0$, the Fredholm alternative theorem implies that a necessary condition for the solution of

$$\mathcal{L}\phi^1 = H \tag{65}$$

is that ϕ^0_z be orthogonal to H, i.e.,

$$\int_{-\infty}^{\infty} 30g(\phi^0)\left[(1-X^0)A_A + X^0A_B\right]\phi^0_z dz = 0 \tag{66}$$

In order to calculate the integral we express ϕ^0_z from (55)

$$\phi^0_z = \frac{X^0_z}{30g(\phi^0)(A_A - A_B)X^0(1-X^0)} \tag{67}$$

This gives the desired relation in terms of usual variables, with X_L and X_S denoting the limits of X from the two directions,

$$[\ln(1-X)]_{solid}^{liquid} = -A_A(T) = -\frac{V_m}{R}L_A\left(\frac{1}{T}-\frac{1}{T_m^A}\right) \tag{68}$$

Manipulating with expressions (63), (68) provides the liquidus and solidus lines as shown in Fig.4.1

$$X_S = \frac{1-exp(-A_A)}{exp(-A_B)-exp(-A_A)} \tag{69}$$

$$X_L = \frac{1-exp(-A_A)}{1-exp(A_B-A_A)} \tag{70}$$

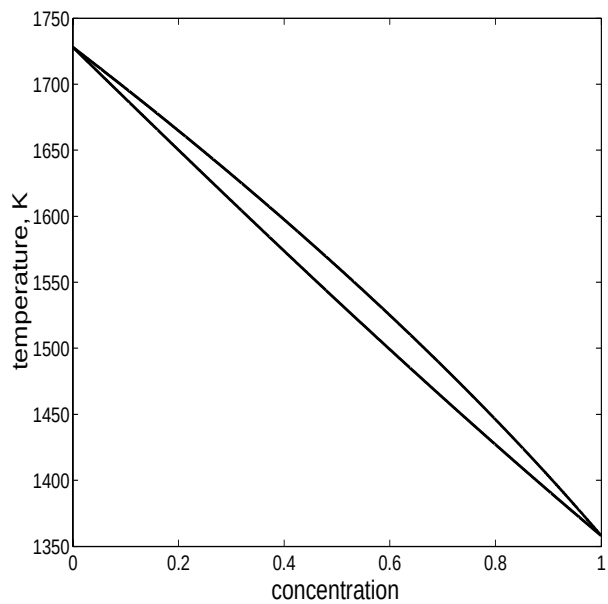

FIGURE 4.1. The phase diagram of Ni-Cu alloy.

The given relations are identical to those obtained via the common tangent construction presented in [**87**].

4.3. Anisotropy

For many materials, including metals, the surface energy and the kinetic coefficient depend on orientation of the phase boundary. These effects were not taken into account in the derivation outlined in Section 4.1.1. Since anisotropy has a crucial impact on the shape of microstructures it is necessary to modify the phase-field equations to account for anisotropy. The most widely used method to include anisotropy is to assume that the parameter ε_ϕ in eq.(4) depends on the orientation of the interface with respect to the frame of reference through the anisotropic surface energy

$$\sigma = \sigma_0\eta(\vec{n}) \tag{71}$$

Then the variational derivative in eq.(11) must be recalculated

$$\begin{aligned}\frac{\delta S}{\delta \phi} &= \frac{\partial s}{\partial \phi} + \nabla \cdot (\eta(\vec{n})\nabla\phi) + \frac{\partial}{\partial x}\left(|\nabla\phi|^2\eta(\vec{n})\frac{\partial\eta(\vec{n})}{\partial\phi'_x}\right) \\ &+ \frac{\partial}{\partial y}\left(|\nabla\phi|^2\eta(\vec{n})\frac{\partial\eta(\vec{n})}{\partial\phi'_y}\right) + \frac{\partial}{\partial z}\left(|\nabla\phi|^2\eta(\vec{n})\frac{\partial\eta(\vec{n})}{\partial\phi'_z}\right)\end{aligned} \tag{72}$$

The choice of the anisotropy function $\eta(\vec{n})$ strictly depends on the modeled microstructure. In the case of three dimensional dendritic growth the common choice is [**34**]

$$\eta(\vec{n}) = (1-3\gamma)\left[1 + \frac{4\gamma}{1-3\gamma}\frac{(\phi'_x)^4 + \left(\phi'_y\right)^4 + (\phi'_z)^4}{|\nabla\phi|^4}\right] \tag{73}$$

which reduces to the standard four-fold variation of η in two dimensions

$$\eta(\theta) = 1 + \gamma\cos(4\theta) \tag{74}$$

where γ is the strength of the anisotropy and $\theta = \arctan(\phi'_y/\phi'_x)$ gives an approximation of an angle between the interface and the orientation of the crystal lattice. With this method of including anisotropy, an asymptotic analysis for the interface width approaching zero, yields the same form of the anisotropic Gibbs-Thompson equation that is employed for sharp interface theories [**17**]. The anisotropic Gibbs-Thompson equation requires $\sigma + \sigma''$ to be positive, which results in the restriction on the value of $\gamma < 1/15$, implying that we may use only mild values of anisotropy for simulating dendrites.

In other cases, such as faceted morphologies, highly anisotropic interfacial properties are required. When $\sigma + \sigma''$ changes sign, this gives rise to orientations that are forbidden and a crystal interface with missing orientations. Formation of flat sides when the polar plot of the anisotropy function has a narrow minimum or a cusp can be predicted by the Wulff construction [**64**], which determines an equilibrium shape of a crystal. Strong anisotropy of the kinetic coefficient [**65**] and the interfacial energy [**66**] were studied in a case of faceted solidification. An example of such an anisotropy function would be

$$\eta(\theta) = 1 + \gamma|\sin(\theta)| \tag{75}$$

This function is non-differentiable at the cusps $\theta = n\pi$ and needs to be regularized [**66**]. Strong anisotropy of the surface energy was implemented for modeling growth of Widmanstätten plates, as described in Paper 4.

4.4. Noise

Dendrites have complex shapes due to the appearance of secondary sidebranches behind the growing tips of primary stalks [**68**]. The physical origin of the sidebranching is small noise perturbations, initially localized at the tip. Amplification of these perturbations to a macroscale along the sides of a steady-state needle crystal leads to giving birth to the sidebranches. The sidebranches consequently appear behind the tip, which implies presence of a continious source of noise at the tip. The experimental results [**67**] indicate that the thermal noise, originating

from microscopic thermal fluctuations inherent in the bulk matter, is responsible for the appearance of the sidebranches.

Typically noise is included into phase-field models in a rather *ad hoc* manner. Kobayashi [**69**] introduced noise by adding a term which is evaluated using a random number generator and showed that sidebranching strongly depends on the strength of noise. Other studies [**41, 30**], used a similar technique by including a noise term into the phase-field equation, thus simulating fluctuations only at the interface. However, these interfacial fluctuations give rise to the sidebranches only in the system with high driving forces (high undecooling and/or supersaturation).

Pavlik and Sekerka [**70**] derived stochastic forces due to thermodynamic fluctuations for anisotropic phase-field models. Based on general principles of irreversible thermodynamics, they showed that the stochastic forces are anisotropic. Gránásy et al [**57, 58**] demonstrated by means of the phase-field method that the thermal fluctuations in the melt are responsible for nucleation of crystalline particles. Karma and Rappel [**71**] incorporated thermal noise quantitatively into a phase-field model for pure solidification. They related the amplitude of noise to physical quantities. Two types of noise were considered in [**71**]: the non-conserved interface noise originating from the exchange of atoms between the two phases, and conserved bulk noise originating from fluctuations in the heat current in the solid and liquid phases. The authors demonstrated that for typical growth conditions at low undercooling the conserved noise is the most relevant one. The long-wavelength interface fluctuations driven by the conserved noise amplify to a macroscopic scale by the morphological instability on the sides of dendrites. In contrast, the non-conserved noise in the evolution equation for ϕ drives short-wavelength fluctuations that are damped and do not affect sidebranching. Consequently, at low undercooling the non-conserved noise can be left out to speed-up computations.

Theoretically, purely deterministic phase-field simulations of dendritic growth should produce needle-like dendrites with absent sidebranches. However, if the diffuse interface region is not properly resolved, e.g. a coarse finite difference mesh is used, calculations will usually exhibit sidebranching typical of real dendrites because discretization errors introduce noise into the calculations. Therefore, one should introduce noise into phase-field models in a controlled way, as in [**71**].

CHAPTER 5

Numerical solution of the phase-field equations

5.1. Finite Difference approach

Most numerical work with the phase-field model has been performed with Finite Difference discretization on uniform structured grids [**21, 31, 41, 57**]. This can be explained by the fact that the finite difference techniques are conceptually simple, and what is more, coding of a Finite Difference algorithms is straightforward and very compact. Typically second-order central differences are used, though application of more sophisticated stencils has been reported [**35**]. Temporal discretization of the time-derivatives can be done using explicit (e.g. Forward Euler, Runge-Kutta) or implicit (e.g. Backward Euler, Crank-Nicholson) methods. For the explicit schemes, the solution on the next time step can be explicitly formulated using the current approximation. For implicit schemes it is necessary to actually solve a large system of algebraic equations to update the solution. It is then not surprising that most of the studies of dendritic growth utilize the explicit schemes.

This approach works well when a single diffusion field is considered in the problem (e.g. thermal or solutal). Then the diffusion coefficient and phase-field mobility are typically of the same order, thus imposing similar demands on stability. Stability condition gives the relation between time step and grid spacing which must hold to prevent uncontrolled growth of errors. However, when several diffusion fields are included into the model, their diffusivity may differ by several orders of magnitude, imposing unreachable demands on the time-step. Consequently, implicit time discretizations are preferred for complex systems. Implicit time-steppings and their parallelization were studied in [**73**]. The Finite Difference methods lead to structured systems approximating PDEs which are easy to parallelize [**57, 72**]. A part of the simulations presented in Paper 5 was performed using parallel implementation of the explicit Finite Difference scheme. For dendritic growth, numerical experiments demonstrate that the Finite Difference codes are most efficient in the case of high driving forces, when diffusion length is small and dendritic microstructures are highly branched.

5.2. Methods based on adaptive grids

Diffuse interface methods for modeling microstructural evolution feature large scale separation. Commonly several orders of magnitude must be resolved: thickness of the phase boundary is of order nanometers, while characteristic features of a microstructure could only be observed on a scale of micrometers. This scale separation is the main computational drawback of the phase-field methods, often preventing results to be quantitative. On the other hand, the variations of the phase-field and diffusion fields are typically localized over the interfacial region.

This motivates one to use adaptive grids which would follow migration of the phase boundary. Adaptive Finite Element methods in combination with the phase-field models have been applied to simulate dendritic solidification of pure materials [**74**]. Provatas et al [**75**] have used a dynamic quad-tree data structure in their adaptive code. They get mostly quadrilateral elements, which are combined with triangular element to avoid hanging nodes. Tönhardt and Amberg [**60, 76, 77**] studied convective effects on dendritic growth using FEM on adaptive triangular grids. A Finite Element method on octagonal elements was used in a 3 dimensional refinement algorithm developed by Jeong [**78**]. A 3 dimensional solutal dendrite shown in Figure 1.1 was calculated by the thesis author using the isothermal approach [**41**]. The adaptive mesh consists of tetrahedra which are bisected according to an elegant recursive refinement algorithm of Arnold [**79**].

Braun and Murray [**32**] have done calculations using a general adaptive Finite Difference technique coupled with a phase-field model. Recently, Lan et al [**80, 81**] applied Finite Volume method for simulating dendritic growth in 2 dimensions on adaptive quadrilateral grids. The benefit of applying adaptive Finite Volume methods is that hanging nodes do not represent a problem. Also these rather structured grids are potentially easy to partition for calculations in a parallel environment. Parallelization of adaptive Finite Element code in 2 and 3 dimensions was performed by Do-Quang et al [**82**]. In the code, dynamic mesh partitioning to achieve load balance is performed after every grid change. Part of the simulations reported in Papers 4 and 5 was performed by means of this parallel code. For the dendritic growth, application of adaptive grids is most beneficial at a low undercooling/supersaturation, since low driving forces result in a decreased velocity, an increased tip radius and a large diffusion length.

5.3. Finite-Difference-Diffusion-Monte-Carlo method

An interesting hybrid approach for diffusion-limited growth problems was proposed by Plapp and Karma [**83**]. Their idea is based on a multiscale diffusion Monte Carlo algorithm which allows off-lattice random walkers to take longer and computationally rare steps with increasing distance away from the phase boundary. The method was applied to simulate dendritic growth of a pure substance [**35**]. The computational domain is split into two parts: the first one contains solid phase and a thin layer of the liquid phase surrounding the interface, the second part contains the remaining liquid. The phase-field equations are solved by means of the Finite Differences in the first domain, while the large-scale diffusion field is represented by an ensemble of off-lattice random walkers and is evolved using the diffusion Monte Carlo method. The two solutions are connected at some distance from the moving interface. The method is essentially effective in the low undercooling limit where the dendrite tip radius is one or more orders of magnitude smaller than the characteristic spatial scale of variation of the surrounding thermal field. This makes the performance of the method similar to the performance of the adaptive Finite Elements approach.

Acknowledgments

My supervisor Dr. Gustav Amberg deserves a lot of thanks and should be specially commended for his time, guidance and encouragement. I am very grateful to him for giving me the opportunity and freedom to carry out this study at KTH. His insight and inspiration, as well confidence in my work, helped me a lot in developing of my thesis.

I am greatly thankful to Professor John Ågren from the Department of Material Science for his ideas, comments and fruitful discussions.

I would like to thank Dr. James Warren for ensuring my pleasant stay at the National Institute of Standards and Technology, USA.

I am also appreciative to Gunilla Kreiss, Krister Andersson, Joakim Odquist and Henrik Strandlund for interesting discussions during my study. Special thanks to Minh Do-Quang, whose amazing parallel code helped me to perform some of my research. During all the years I enjoyed very much the benevolent atmosphere at the Department of Mechanics, thanks to my colleagues.

Finally and most important, I sincerely thank my friends and my family for their unconditional love and support.

Financial support was provided by the Swedish Research Council (VR).

Bibliography

[1] G.P.Ivantsov, Thermal and diffusional processes in crystal growth I, *Growth of crystals*, 1,1956,76-85, Thermal and diffusional processes in crystal growth II, *Growth of crystals*, 3,1959,53-60

[2] J.S.Langer, Instabilities and pattern formation in crystal growth, *Reviews of modern physics*, 52,1980,1-28

[3] W.Kurz and D.J.Fisher, Fundamentals of Solidification, *Trans Tech Publications*, 1986

[4] W.W.Mullins and R.F.Sekerka, Stability of a planar interface during solidification of a dilute binary alloy, *Journal of applied physics*, 35, 1964, 444-451

[5] W.W.Mullins and R.F.Sekerka, Morphological stability of a particle growing by diffusion or heat flow, *Journal of applied physics*, 34, 1963, 323-329

[6] R.Triverdi and W.Kurz, Morphological stability of a planar interface under rapid solidification conditions, *Acta metall.*, 34, 1985, 1663-1670

[7] S.R.Coriell and R.F.Sekerka, The effects of the anisotropy of surface tension and interface kinetics on morphological stability, *Journal of crystal growth*, 34, 1976, 157-163

[8] S.M.Allen and J.W.Cahn, A microscopic theory for antiphase boundary motion and its application to antiphase domain coarsening, *Acta metallurgica*, 27, 1979, 1085-1095

[9] J.W.Cahn and J.E.Hilliard, Free energy of a nonuniform system, I: Interfacial free energy, *J. Chem. Phys.*, 28, 1957, 258-267

[10] J.S.Langer, in Directions in condensed matter physics, edited by G.Grinstein and G.Mazenko (World Scientific, Singapore, 1986), p.165

[11] G.J.Fix, in Free Boundary Problems: Theory and Applications, edited by A.Fasano and A.Primicerio (Piman, Boston, 1983), Vol.II, p.580

[12] J.B.Collins and H.Levin, Diffuse interface model of diffusion-limited crystal growth, *Physical review B*, 31, 1985, p.6119

[13] G.Caginalp and P.Fife, Phase-field methods for interfacial boundaries, *Physical review B*, 33, 1986, p.7792

[14] G.Caginalp and P.Fife, Higher-order phase-field models and detailed anisotropy, *Physical review B*, 34, 1986, p.4940

[15] J.S.Langer and R.F.Sekerka, Theory of Departure from Local Equilibrium at the Interface of a Two-Phase Diffusion Couple, *Acta Metall*, 23, 1975, 1225-1237

[16] G.Caginalp and J.Jones, A derivation and analysis of phase field models of thermal alloys, *Annals of physics*, 237, 1995, 66-107

[17] G.B.McFadden, A.A.Wheeler, R.J.Braun, S.R.Coriell and R.F.Sekerka, Phase-field models fro anisotropic interfaces, *Physical review E*, 48,1993,2016-2024

[18] W.J.Boettinger, J.A.Warren, C.Beckermann and A.Karma, Phase-field simulation of solidification, *Annual review of materials research*, 32,2002,163-194

[19] L-Q.Chen, Phase-field models for microstructure evolution, *Annual review of materials research*, 32,2002,113-140

[20] W.J.Boettinger, S.R.Coriell, A.L.Greer, A.Karma, W.Kurz, M.Rappaz and R.Trivedi, Solidification microstructures: recent developments, future directions, *Acta Materialia*, 48,2000,43-70

[21] R. Kobayashi, Simulations of Three Dimensional Dendrites, *Pattern Formation in Complex Dissipative Systems, ed. S.Kai, World Sci. Pub. Singapore*, 1992, 121-128

[22] R.Kobayashi, Numerical Approach to Three-Dimensional Dendritic Solidification, *Experimental Mathematics*, 3(1), 1994, 59-81

[23] D.Juric and G.Tryggvason, A front-tracking method for dendritic solidification, *Journal of computational physics*, 123, 1996, 127-148

[24] R.F.Almgren, Variational algorithms and pattern formation in dendritic solidification, *Journal of computational physics*, 106, 1993, 337-354

[25] A.Schmidt, Computation of three dimensional dendrites with finite elements, *Journal of computational physics*, 125, 1996, 293-312

[26] S.Chen, B.Merriman, S.Osher and P.Smereka, A Simple Level Set Method for Solving Stefan Problems, *Journal of Computational Physics*, 135(1), 1997, 8-29

[27] S.Osher and J.A.Sethian, Fronts propagating with curvature-dependent speed: Algorithms based on Hamilton-Jacobi formulations, *Journal of computational physics*, 79, 1988, 12-49

[28] Y.-T.Kim, N.Goldenfeld and J.Dantzig, Computation of dendritic microstructures using a level set method, *Physical review E*, 62, 2000, 2471-2474

[29] S.-L.Wang, R.F.Sekerka, A.A.Wheeler, B.T.Murray, S.R.Coriell, R.J.Braun and G.B.McFadden, Thermodynamically-consistent phase-field models for solidification, *Physica D*, 69, 1993, 189-200

[30] A.A.Wheeler, B.T.Murray and R.J.Schaefer, Computation of dendrites using a phase field model, *Physica D*, 66,1993,243-262

[31] B.T.Murray, A.A.Wheeler and M.E.Glicksman, Simulations of experimentally observed dendritic growth behavior using a phase-field model, *Journal of crystal growth*, 154, 1995, 386-400

[32] R.J.Braun and B.T.Murray, Adaptive phase-field computations of dendritic crystal growth, *Journal of crystal growth*, 174, 1997, 41-53

[33] A.Karma and W-J.Rappel, Phase-field method for computationally efficient modeling of solidification with arbitrary interface kinetics, *Physical review E*, 53, 1996, 3017-3020

[34] A.Karma and W-J.Rappel, Quantitative phase-field modeling of dendritic growth in two and three dimensions, *Physical review E*, 57, 1998, 4323-4349

[35] J.Bragard, A.Karma, Y.H.Lee and M.Plapp, Linking phase-field and atomistic simulations to model dendritic solidification in highly undercooled melt, *Interface science*, 10, 2002, 121-136

[36] A.A.Wheeler, W.J.Boettinger and G.B.McFadden, Phase-field model for isothermal phase transitions in binary alloys, *Physical review E*, 45,1992, 7424-7439

[37] A.A.Wheeler, W.J.Boettinger and G.B.McFadden, Phase-field model of solute trapping during solidification, *Physical review E*, 47, 1993, 1893-1909

[38] W.J.Boettinger, A.A.Wheeler, B.T.Murray and G.B.McFadden, Prediction of solute trapping at high solidification rates using a diffuse interface phase-field theory of alloy solidification, *Materials science and engineering*, A178, 1994, 217-223

[39] N.A.Ahmad, A.A.Wheeler, W.J.Boettinger and G.B.McFadden, Solute trapping and solute drag in a phase-field model of rapid solidification, *Physical review E*, 58,1998,3436-3450

[40] I. Loginova, J. Odqvist, G. Amberg and J. Ågren, The phase-field approach and solute drag modeling of the transition to massive $\gamma \to \alpha$ transformation in binary Fe-C alloys, *Acta Materialia*, 51, 2003, 1327-1339

[41] J.A.Warren and W.J.Boettinger, Prediction of dendritic growth and microsegregation patters in a binary alloy using the phase-field method, *Acta metall. metar.*, 43,1995,689-703

[42] W.J.Boettinger and J.A.Warren, The phase-field method: simulation of alloy dendritic solidification during recalescence, *Metallurgical and materials transactions A*, 27A,1996,657-668

[43] W.J.Boettinger and J.A.Warren, Simulation of cell to plane front during directional solidification at high velocity, *Journal of crystal growth*, 200,1999,583-591

[44] J.A. Warren and B.T. Murray, Ostwald Ripening and Coalescence of a Binary Alloy in Two Dimensions using a Phase-Field Model, *Modeling and Sim. in Matls Sci.*, 4, 1996, 215-229.

[45] Z.Bi and R.F.Sekerka, Phase-field model of solidification of a binary alloy, *Physica A*, 261, 1998, 95-106

[46] I.Loginova, G.Amberg and J.Ågren, Phase-field simulations of non-isothermal binary alloy solidification, *Acta materialia*, 49, 2001, 573-581

[47] A.Karma, Phase-field formulation for quantitative modeling of alloy solidification, *Physical review letters*, 87, 2001, 115701

[48] J.C.Ramirez and C.Beckermann, Quantitative modeling of binary alloy solidification with coupled heat and solute diffusion via the phase-field method, *presented at the 41st AIAA Aerospace Sciences Meeting, Reno, Nevada*, 2003

[49] L.-Q. Chen, W. Yang, Computer simulation of the domain dynamics of a quenched system with a large number of nonconserved order parameters: The grain-growth kinetics, *Physical Review B*, 50, 1994, 15752

[50] I. Steinbach, F. Pezzolla, B. Nestler, M. BeeBelber, R. Prieler, G.J. Schmitz, J.L.L. Rezende, A phase field concept for multiphase systems, *Physica D*, 94, 1996, 135-147

[51] C.E.Krill III and l.Q.Chen, Computer simulation of 3-D grain growth using a phase-field model, *Acta materialia* , 50, 2002, 3057-3073

[52] R.Kobayashi, J.A.Warren and W.C.Carter, A Simple Continuum Model of Grain Boundaries, *Physica D*, 140, 141-150 (2000)

[53] J.A.Warren, R.Kobayashi and W.C.Carter,Modeling Grain Boundaries Using a Phase-field Technique, *J. Cryst. Growth*, 211, 18-20 (2000)

[54] J.A.Warren, W.C.Carter and R.Kobayashi, A Phase Field Model of the Impingement of Solidifying Particles, *Physica A*, 261, 159- (1998).

[55] R.Kobayashi, J.A.Warren and W.C.Carter, Vector-valued Phase Field Model for Crystallization and Grain Boundary Formation, *Physica D*, 119, 415-423 (1998)

[56] R.Kobayashi, J.A.Warren and W.C.Carter, Mathematical Models for Solidification and Grain Boundary Formation, *ACH-Models in Chemistry*, 135, 287-295 (1998)

[57] L.Gránásy, T. Börzsönyi and T. Pusztai, Nucleation and bulk crystallization in binary phase field theory, *Phys. Rev. Lett* 88, 2002, 206105

[58] L.Gránásy, T. Börzsönyi and T. Pusztai, Crystal nucleation and growth in binary phase-field theory, *Journal of crystal growth*, 237-239, 2002, 1813-1817

[59] J.A. Warren, I. Loginova, L. Gránásy, T. Börzsönyi and T. Pusztai, Phase Field Modeling of Alloy Polycrystals,*Proceedings of Modeling Casting and Advanced Solidification Processes X, edited by D. Stefanescu, J. A. Warren, M. Krane and M. Jolly*, 2003.

[60] R.Tönhardt and G.Amberg, Simulation of natural convection effects on succinonitrile crystals, *Physical review E*, 62, 2000, 828-836

[61] C.Beckermann, H.-J.Diepers, I.Steinbach, A.Karma and X.Tong, Modeling melt convection in phase-field simulations of solidification, *Journal of computational physics*, 154, 1999, 468-496

[62] G.Caginalp and Xie, Phase-field and sharp-interface alloy models, *Physica Review A*, 48, 1993, p1897-1909

[63] T.Suzuki, M.Ode, S.G.Kim and W.T.Kim, Phase-field model of dendritic growth, *J. Crystal Growth* , 237-239, 2002, 125-131

[64] S.H.Davis, Theory of Solidification *Cambridge University Press*, 2001

[65] T.Uehara and R.F.Sekerka, Phase-field simulations of faceted growth for strong anisotropy of kinetic coefficient, *Journal of crystal growth*, 254, 2003, 251-261

[66] J.M.Debierre, A.Karma, F.Celestini and R.Guerin, Phase-field approach for faceted solidification, *cond-mat/0302368*

[67] A.Dougherty, P.D.Kaplan and J.P.Gollub, Development of side branching in dendritic crystal growth, *Phys. Rev. Lett.*, 58, 1987, 1652

[68] C.Huang and M.E.Glicksman, Fundamentals of Dendritic Solidification: I. Steady State Tip Growth, *Acta materialia*, 29, 1981, 701, Fundamentals of Dendritic Solidification: I. Development of Sidebranch Structure, *Acta materialia*, 29, 1981, 717

[69] R.Kobayashi, Modeling and numerical simulations of dendritic crystal growth, *Physica D*, 63, 1993, 410-423

[70] S.G.Pavlik and R.F.Sekerka, Forces due to fluctuations in the anisotropic phase-field model of solidification, *Physica A*, 268, 1999, 283-290

[71] A.Karma and W-J.Rappel, Phase-field model of dendritic sidebranching with thermal noise, *Physical review E*, 60, 1999, 3614-3625

[72] W.L.George and J.Warren, A parallel 3D dendritic growth simulator using the phase-field model, *Journal of Computational physics*, 177,2002,264-283

[73] C.Andersson, Phase-field simulation of dendritic solidification, *Doctoral thesis*, KTH, 2002

[74] R.Tönhardt, Convective effects on dendritic solidification, *Doctoral thesis*, KTH, 1998

[75] N.Provatas, N.Goldenfeld and J.Dantzig, Adaptive mesh refinement computation of solidification microstructures using dynamic data structures, *Journal of computational physics*, 148, 1999, 265-290

[76] R.Tönhardt and G.Amberg, Phase-field Simulation of Dendritic Growth in a Shear Flow, *J. Crystal Growth* 194, 1998, 406-425

[77] R.Tönhardt and G.Amberg, Dendritic growth of randomly oriented nuclei in a shear flow, *J. Crystal Growth*, 213, 2000, 161-187

[78] J-H.Jeong, N.Goldenfeld and J.A.Dantzig, Phase-field model for three-dimensional dendritic growth with fluid flow, *Physical review E*, 64, 2001, 041602

[79] D.N.Arnold and A.Mukherjee, Tetrahedral bisection and adaptive finite elements, *Grid Generation and Adaptive Algorithms, M. Bern, J. E. Flaherty, and M. Luskin, eds., IMA Volumes in Mathematics and its Applications*, 113, 1999, pp. 29-42.

[80] C.W.Lan, C.M.Hsu and C.C.Liu, Efficient adaptive phase-field simulation of dendritic growth in a forced flow at low supercooling, *Journal of crystal growth*, 241, 2002, 379-386

[81] C.W.Lan and Y.C.Chang, Efficient adaptive phase-field simulation of directional solidification of a binary alloy, *Journal of crystal growth* , 250, 2003, 525-537

[82] M.Do-Quang, I.Loginova and G.Amberg, Application of parallel adaptivity to simulation of materials processes, in preparation

[83] M.Plapp and A.Karma Multiscale Finite-Difference-Diffusion-Monte-Carlo method for simulating dendritic growth, *Journal of computational physics*, 165, 2000, 592-619

[84] I.Steinbach, F.Pezzolla, B.Nestler, M.Seesselberg, R.Prieler, G.J.Schmitz and J.L.L.Rezende, A phase field concept for multiphase systems, *Physica D*, 94, 1996, 135 - 147

[85] B.Nestler and A.A.Wheeler, A Multi-phase-field Model of Eutectic and Peritectic Alloys: Numerical Simulation of Growth Structures, *Physica D* 138, 2000, 114-133

[86] M.Plapp and A.Karma, Eutectic colony formation: A stability analysis *Physical review E*, 60, 1999, 6865-6889

[87] J.F.McCarthy, Phase diagram effects in phase field models of dendritic growth in binary alloys, *Acta material*, 45, 1997, p4077-4091

[88] Y.Wang and A.G.Khachaturyan, Three-dimensional phase field model of low-symmetry martensitic transformation in polycrystal: simulation of ζ_2' martensite in AuCd alloys,*Acta materialia*, 49, 2001, 2309-2320

[89] Artemev, Y.Wang and A.G.Khachaturyan,Three-dimensional phase field model and simulation of martensitic transformation in multilayer systems under applied stresses ,*Acta materialia*, 48, 2000, 2503-2518

[90] S.Semenovskaya and A.G.Khachaturyan, Development of ferroelectric mixed states in a random field of static defects,*Journal of applied physics*, 83, 1998, 5125-5136

[91] Y.L.Li, S.Y.Hu, Z.K.Liu and L.Q.Chen, Phase-field model of domain structures in ferroelectric thin films *Applied physical letters*, 78, 2001, 3878-3880

[92] H.Garcke and B.Nestler, A mathematical model for grain growth in thin metallic films, *Math. Models and Methods in Applied Sciences* 10(6), 2000, 895 - 921

[93] A.Karma, D.A.Kessler and H.Levine, Phase-Field Model of Mode III Dynamic Fracture *Physical review letters*, 87, 2001, 045501

[94] J.E.Guyer, W.J.Boettinger, J.A.Warren and G.B.McFadden, Phase field modeling of electrochemistry I: Equilibrium *cond-mat/0308173*; Phase field modeling of electrochemistry II: Kinetics *cond-mat/0308179*

Paper 1

P1

Pergamon

Acta mater. 49 (2001) 573–581

Acta MATERIALIA

www.elsevier.com/locate/actamat

PHASE-FIELD SIMULATIONS OF NON-ISOTHERMAL BINARY ALLOY SOLIDIFICATION

I. LOGINOVA[1]*, G. AMBERG[1] and J. ÅGREN[2]

[1]Department of Mechanics, KTH, 100 44 Stockholm, Sweden and [2]Department of Materials Science and Engineering, KTH, 100 44 Stockholm, Sweden

(Received 27 June 2000; received in revised form 18 October 2000; accepted 23 October 2000)

Abstract—A phase-field method for two-dimensional simulations of binary alloy solidification is studied. Phase-field equations that involve both temperature and solute redistribution are formulated. The equations are solved using the finite element method with triangular elements on unstructured meshes, which are adapted to the solution. Dendritic growth into a supersaturated melt is simulated for two temperature regimes: (a) the temperature is prescribed on the boundary of the computational domain; and (b) the heat is extracted through the domain boundary at a constant rate. In the former regime the solute redistribution is compared with the one given by an isothermal model. In the latter case the influence of the size of the computational domain and of the heat extraction rate on dendritic structure is investigated. It is shown that at high cooling rates the supersaturation is replaced by thermal undercooling as the driving force for growth.

Keywords: Phase-field; Kinetics; Diffusion

1. INTRODUCTION

Over the last 10 years the phase-field method has been extensively used for simulations of dendritic growth. In the phase-field method a new variable $\phi(x, y, t)$ is introduced to indicate the physical state of the system at each point. ϕ takes on constant values in solid and liquid and changes steeply but smoothly over a thin transition layer that plays the role of the classical sharp interface. The governing equation coupled with modified transport equations are applied in all of space without distinguishing between the phases. This permits simulations of growing morphologies without explicitly tracking the phase boundaries.

Solidification of a binary mixture has been studied by Caginalp *et al*. [5, 8]. It is shown that the phase-field equations reduce to the traditional sharp interface models in the limit when the thickness of the interfacial region δ vanishes. At the same time computations demonstrate that the phase-field methods produce an interface close to the sharp interface problem even for relatively large δ.

Despite the great success in predicting qualitatively realistic microstructures, the phase-field method has only been applied to very simple systems. Typically heat flow during solidification of pure substances or isothermal diffusion in binary alloys obeying ideal solution thermodynamics have been studied. However, from a technological point of view, it would be valuable to perform simulations on real alloys, which are usually multicomponent and have complex thermodynamic interactions.

Warren and Boettinger [1] derived a phase-field model for isothermal solidification of a binary alloy, applying constant diffusivities within the solid and liquid phases, and performed two-dimensional simulations of dendritic growth into a highly supersaturated liquid. This model has been explored in several papers, for example, [9–12]. A desirable extension of the model is to study the effect of heat flow due to release of latent heat. However, the numerical implementation is not trivial since the temperature and solute evolution occurs on completely different time-scales. A simplified approach was proposed in Ref. [4], where the spatial variation of the temperature is neglected and the heat equation is replaced by a heat balance of an imposed heat extraction rate and the latent heat release rate.

The present report is part of a project where the ultimate goal is to apply the phase-field method to simulate processing of real alloys. As a first step, the phase-field formulation [1] is applied, with the major difference being that simultaneous heat flow and dif-

* To whom all correspondence should be addressed. Fax: +46-8-796-9850.

E-mail address: irina@mech.kth.se (I. Loginova)

1359-6454/01/$20.00
PII: S1359-6454(00)00360-8

fusion are taken into account. The paper is organized as follows: Section 1 gives an overview of the model derivation; numerical aspects are presented in Section 2; in the next two sections results of truly non-isothermal calculations of dendritic growth for two temperature regimes are presented and discussed.

2. MATHEMATICAL MODEL

In this section the phase-field model given in Ref. [1] is considered with modifications accounting for temporal and spatial evolution of the temperature field. The formulation is based on an entropy functional

$$S = \int_{\Omega}\left(s(\phi,x_{\mathrm{B}},e)-\frac{\epsilon^2}{2}|\nabla\phi|^2\right)\mathrm{d}\Omega \tag{1}$$

where the thermodynamic entropy density s is a function of the phase-field variable ϕ varying smoothly between 0 in the solid and 1 in the liquid, the mole fraction x_{B} of a solute B in solvent A and the internal energy density e, and Ω is a spatial region occupied by a mixture.

Anisotropy is included in the system because the phase change kinetics depends upon the orientation of the interface

$$\epsilon = \bar{\epsilon}\eta = \bar{\epsilon}(1 + \gamma\cos k\beta) \tag{2}$$

where $\bar{\epsilon}$ is related to the surface energy σ and interface thickness, γ is the magnitude of anisotropy in the surface energy, k specifies the mode number and the expression $\beta = \arctan(\phi_y/\phi_x)$ gives an approximation of the angle between the interface normal and the orientation of the crystal lattice.

The evolution of the non-conserved phase-field variable is governed by

$$\dot{\phi} = M_{\phi}\frac{\delta S}{\delta\phi} \tag{3}$$

where M_{ϕ} is related to the interfacial mobility. The evolution of x_{B} and e is governed by the normal conservation laws

$$\frac{\dot{x}_{\mathrm{B}}}{V_{\mathrm{m}}} = -\nabla\cdot\mathbf{J}_{\mathrm{B}} \tag{4}$$

$$\dot{e} = -\nabla\cdot\mathbf{J}_e \tag{5}$$

where V_{m} is the molar volume. The diffusional flux $\mathbf{J}_{\mathrm{B}}$ and the heat flux $\mathbf{J}_e$ are given by the linear laws of irreversible thermodynamics

$$\mathbf{J}_B = L^{\mathrm{A}}_{\mathrm{BB}}\nabla\frac{\delta S}{\delta x_{\mathrm{B}}} + L^{\mathrm{A}}_{\mathrm{B}e}\nabla\frac{\delta S}{\delta e} \tag{6}$$

$$\mathbf{J}_e = L^{\mathrm{A}}_{e\mathrm{B}}\nabla\frac{\delta S}{\delta x_{\mathrm{B}}} + L^{\mathrm{A}}_{ee}\nabla\frac{\delta S}{\delta e} \tag{7}$$

$L^{\mathrm{A}}_{\mathrm{BB}}$ and L^{A}_{ee} are related to the inter-diffusional mobility of B and A and the heat conduction, respectively. The coefficient $L^{\mathrm{A}}_{\mathrm{B}e} = L^{\mathrm{A}}_{e\mathrm{B}}$ describes the cross effects between heat flow and diffusion and will be neglected. The second law requires M_{ϕ}, $L^{\mathrm{A}}_{\mathrm{BB}}$ and L^{A}_{ee} to be positive. It should be emphasized that the gradients $\nabla(\delta S/\delta x_{\mathrm{B}})$ and $\nabla(\delta S/\delta e)$ are to be evaluated isothermally and under fixed composition, respectively. The variational derivatives in equations (6) and (7) are given by

$$\frac{\delta S}{\delta x_{\mathrm{B}}} = \frac{\partial s}{\partial x_{\mathrm{B}}} = -\frac{\mu_{\mathrm{B}}-\mu_{\mathrm{A}}}{TV_{\mathrm{m}}} \tag{8}$$

$$\frac{\delta S}{\delta e} = \frac{\partial s}{\partial e} = \frac{1}{T} \tag{9}$$

where T is the temperature and the quantity on the right-hand side of equation (8) is known as the inter-diffusion potential in binary substitutional alloys. The chemical potentials μ_{A} and μ_{B} under the assumption of an ideal mixture have the following form

$$\mu_{\mathrm{A}} = {}^{\circ}\mu_{\mathrm{A}}(\phi, T) + RT\ln(1-x_{\mathrm{B}}) \tag{10}$$

$$\mu_{\mathrm{B}} = {}^{\circ}\mu_{\mathrm{B}}(\phi, T) + RT\ln x_{\mathrm{B}} \tag{11}$$

The expressions of the molar Gibbs energy for pure materials are presented as in Ref. [7]

$$\frac{{}^{\circ}\mu_{\mathrm{A}}}{V_{\mathrm{m}}} = W_{\mathrm{A}}g(\phi)T + [e^{\mathrm{s}}_{\mathrm{A}}(T^{\mathrm{A}}_{\mathrm{m}})-c_{\mathrm{A}}T^{\mathrm{A}}_{\mathrm{m}} + p(\phi)\Delta H_{\mathrm{A}}]\left(1-\frac{T}{T^{\mathrm{A}}_{\mathrm{m}}}\right)-c_{\mathrm{A}}T\ln\frac{T}{T^{\mathrm{A}}_{\mathrm{m}}} \tag{12}$$

$$\frac{{}^{\circ}\mu_{\mathrm{B}}}{V_{\mathrm{m}}} = W_{\mathrm{B}}g(\phi)T + [e^{\mathrm{s}}_{\mathrm{B}}(T^{\mathrm{B}}_{\mathrm{m}})-c_{\mathrm{B}}T^{\mathrm{B}}_{\mathrm{m}} + p(\phi)\Delta H_{\mathrm{B}}]\left(1-\frac{T}{T^{\mathrm{B}}_{\mathrm{m}}}\right)-c_{\mathrm{B}}T\ln\frac{T}{T^{\mathrm{B}}_{\mathrm{m}}} \tag{13}$$

where $g(\phi) = \phi^2(1-\phi)^2$ and W_{A}, W_{B} are constants. $e^{\mathrm{s}}_{\mathrm{A}}(T^{\mathrm{A}}_{\mathrm{m}})$ and $e^{\mathrm{s}}_{\mathrm{B}}(T^{\mathrm{B}}_{\mathrm{m}})$ are the energy densities of pure

solid A and B at their melting points T_m^A and T_m^B, respectively. ΔH_A and ΔH_B are the heats of fusion per volume, c_A and c_B are the heat capacities and R is the gas constant. $p(\phi)$ is a smoothing function, chosen such that $p'(\phi) = 30g(\phi)$.

The phase-field equation (3) in the present model is used as derived in Ref. [1]

$$\dot{\phi} = M_\phi \bar{\epsilon}^2 \left[\nabla\cdot(\eta^2 \nabla\phi) - \frac{\partial}{\partial x}\left(\eta\eta_\beta' \frac{\partial\phi}{\partial y}\right) + \frac{\partial}{\partial y}\left(\eta\eta_\beta' \frac{\partial\phi}{\partial x}\right)\right] - M_\phi((1-x_B)H_A + x_B H_B) \tag{14}$$

where

$$H_A(\phi, T) = W_A g'(\phi) + 30g(\phi)\Delta H_A\left(\frac{1}{T} - \frac{1}{T_m^A}\right) \tag{15}$$

$$H_B(\phi, T) = W_B g'(\phi) + 30g(\phi)\Delta H_B\left(\frac{1}{T} - \frac{1}{T_m^B}\right)$$

The diffusion equation is now obtained by combining equations (4), (6), (8) and (10)–(13). However, as pointed out earlier, the gradient $\nabla(\delta S/\delta x_B)$ must be evaluated isothermally, therefore the diffusional flux may be written

$$\mathbf{J}_B = L_{BB}^A \left[-\frac{R}{x_B(1-x_B)}\nabla x_B + (H_A(\phi, T) - H_B(\phi, T))\nabla\phi \right] \tag{16}$$

Comparison of equation (16) with the normal Fick's law of diffusion gives that

$$L_{BB}^A = D\frac{x_B(1-x_B)}{RV_m} \tag{17}$$

where D is the normal Fickian coefficient of interdiffusion of A and B. In this case the so-called thermodynamic factor is unity because the ideal solution is assumed. The final diffusion equation is then obtained by combining equations (4), (16) and (17) and takes the form

$$\dot{x}_B = \nabla\cdot D\left[\nabla x_B + \frac{V_m}{R} x_B(1-x_B)(H_B(\phi, T) - H_A(\phi, T))\nabla\phi \right] \tag{18}$$

The diffusion coefficient is postulated as a function of the phase-field variable

$$D = D_S + p(\phi)(D_L - D_S) \tag{19}$$

where D_S, D_L are the classical diffusion coefficients in the solid and liquid, respectively.

To complete the derivation of the model, the internal energy density is postulated according to Ref. [5]

$$e = (1-x_B)e_A + x_B e_B \tag{20}$$

The internal energy densities of pure materials under the assumption of equal solid and liquid heat capacities are

$$e_A = e_A^s(T_m^A) + c_A(T - T_m^A) + p(\phi)\Delta H_A \tag{21}$$

$$e_B = e_B^s(T_m^B) + c_B(T - T_m^B) + p(\phi)\Delta H_B$$

Inserting equation (20) into equation (5) with $L_{ee}^A = KT^2$ implies that the heat equation has the form

$$\bar{c}\dot{T} + 30g(\phi)\Delta\tilde{H}\dot{\phi} + N\dot{x}_B = \nabla\cdot K\nabla T \tag{22}$$

where the following formulae are introduced

$$\tilde{c} = (1-x_B)c_A + x_B c_B \tag{23}$$

$$\Delta\tilde{H} = (1-x_B)\Delta H_A + x_B\Delta H_B \tag{24}$$

and $N = \partial e/\partial x_B$. Similar to the heat capacity and the latent heat of fusion of the mixture the thermal conductivity of the mixture is approximated by a weighted sum of conductivities of the pure materials

$$K = (1-x_B)K_A + x_B K_B \tag{25}$$

Again, equal solid and liquid thermal conductivities of both materials are assumed. Following Ref. [8], the heat equation is simplified by dropping the $\dot{x}_B$ term

$$\bar{c}\dot{T} + 30g(\phi)\Delta\tilde{H}\dot{\phi} = \nabla\cdot K\nabla T \tag{26}$$

A similar heat equation was derived in Ref. [12] for the case of a dilute alloy.

3. NUMERICAL ISSUES

For convenience, the governing equations (14), (18) and (26) are transformed into dimensionless form. Length and time have been scaled with a reference length $l = 0.94\delta$ and the diffusion time l^2/D_L, respectively. The non-dimensional temperature is

defined as $\theta = (T-T^*)/\Delta T$, where T^* is the temperature of the liquidus associated with an initial solute composition.

In the present phase-field formulation the interface thickness is treated as an input parameter. From a physical point of view, it is desirable to take δ close to the capillary length $l_0=7.1\times10^{-10}$ m. However, this requires extremely dense grids and time-consuming computations. To validate the choice of δ, the steady growth of a dendrite tip was investigated for $\delta=4.9\times10^{-8}$, 1.7×10^{-8}, 4.5×10^{-9} and 2.2×10^{-9} m. The same rate of convergence of the liquid concentration at the interface x_B towards the sharp interface theory prediction x_B^{SI} was obtained here, as that reported in Ref [1]. The dendrite tip speed for these values of δ is 1.2, 1.0, 0.94, and 0.93 cm/s, respectively. With $\delta=4.9\times10^{-8}$ m, as chosen for the present calculations, the tip speed thus varies $<30\%$ when the interface thickness is reduced by a factor of 20, almost down to the nominal value. This indicates that the phase-field method produces an interface reasonably close to the sharp interface problem even for relatively large δ.

Following Ref. [1] a Ni–Cu alloy is chosen for the simulations. All the phase-field parameters are related to the physical properties of the alloy and given in Ref. [1]. The physical data used in the calculations are presented in Table 1. The magnitude of anisotropy γ is 0.04 and $k=4$ employs four-fold symmetry, which allows one to reduce computational costs by performing calculations only in one-fourth of the domain.

The whole region initially contains supersaturated (0.86) and undercooled ($\Delta T=20.5$K) melt, specifically for the alloy composition $x_B^o = 0.4083$ and $T=1574$K, except for a small nuclei of a circular shape with non-dimensional radius $r_0=2$, placed in the centre of the domain. The initial distribution of ϕ is based on the solution of one-dimensional phase-field equation for isothermal coexistence of liquid and solid at a planar interface of a pure metal

$$\phi(x, y, 0) = \frac{1}{2}\left[1 + \tanh\left(\frac{\sqrt{x^2 + y^2}-r_0}{2\sqrt{2}}\right)\right] \quad (27)$$

Zero Neumann boundary conditions for x_B and ϕ are imposed at the boundaries. The boundary conditions for temperature will be defined later.

It was shown in Ref. [1] that stochastic noise introduced into the phase-field model causes fluctuations at the solid/liquid interface, that leads to the development of a dendritic structure. According to Refs. [13,14] the physical origin of the noise is stochastic forces appearing in the system due to thermodynamic fluctuations near the dendrite tip. The noise is included as proposed in Ref. [1] by modifying the phase-field equation

$$\dot{\phi}\rightarrow\dot{\phi}-M_\phi\alpha r16g(\phi)((1-x_B)H_A + x_BH_B) \quad (28)$$

where r is a random number distributed uniformly between -1 and $+1$, a new number is generated for every point of the grid, at each time-step. α is an amplitude of the fluctuations taken as 0.4.

A specific feature of binary alloy solidification is that the changes of x_B and ϕ are highly localized over the solid/liquid interface. The width of the interface is much smaller than the other length scales, which makes the use of an adaptive unstructured mesh beneficial. Initially the computational domain is spatially discretized with large triangular elements and then the interface region gets the highest resolution. As the interface evolves during the computation the mesh is adaptively changed by splitting or merging the elements according to an error-function

$$\mathrm{Err}\approx\int_{\Gamma_{el}}(\nabla\phi + \nabla\theta + 25\phi\nabla x_B)\cdot\bar{n}\mathrm{d}\Gamma + 100\int_{\Omega_{el}}\phi^2(1-\phi)^2\mathrm{d}\Omega \quad (29)$$

where Ω_{el} is the area of an element and Γ_{el} is its boundary with normal $\bar{n}$. This technique provides accurate results with a minimum number of elements. For more details the reader is referred to Ref. [6].

The system of non-dimensional equations is transformed into a discrete problem by the use of Galerkin formulation of the finite element method, with linear basis functions. The time derivatives are discretized by a first order finite difference approximation, the diffusion terms are made implicit and when it is possible the other terms are also chosen implicitly. Although the numerical scheme is quite stable, the time-step is chosen significantly below the stability limit to satisfy an accuracy requirement. A Fortran code was developed by means of FemLego [2,3] which performs automatic code generation from a high-level Maple specification.

The numerical scheme was verified on the isothermal model, equations (14) and (18). A square computational domain of non-dimensional size 750×750 is used in the simulations. Minimum and maximum mesh resolution was defined as a compromise between number of gridpoints and an implicit numerical noise produced by the model. With 0.625 and 10 no secondary sidebranches are developed

Table 1. Physical data for Ni, Cu

	Nickel(A)	Copper (B)
T_m (K)	1728	1358
ΔH (J/m^3)	2350×10^6	1728×10^6
σ (J/m^2)	0.37	0.29
D_L (m^2/s)	10^{-9}	10^{-9}
D_S (m^2/s)	10^{-13}	10^{-13}
c [J/(Km^3)]	5.42×10^6	3.96×10^6
K [J/(Ksm)]	84.0	200.0

when $\alpha=0$. The steady-state growth velocity of the dendrite tip was chosen as a reliable quantity to define time-step. It was found that with $\Delta t=0.2$ the numerical scheme gives an error of the tip speed ca 3%. Solute redistribution obtained for isothermal calculations is given in Fig. 1.

4. TEMPERATURE FIXED ON THE BOUNDARY

To complete the model describing cooling of a melt with growing nuclei, thermal boundary conditions are to be specified. Different types of boundary conditions determine different thermal regimes affecting the temperature variation in space. In this section equations (14), (18) and (26) are solved with $T=1574$K as initial and boundary conditions for the heat equation. This is done in order to fit the non-isothermal temperature regime to the isothermal case. The results of this simulation are shown in Figs 2 and 3.

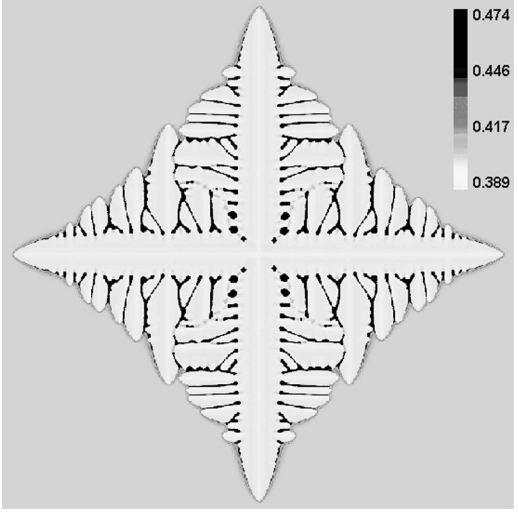

Fig. 1. Concentration field, isothermal model. Time is 2.75 ms.

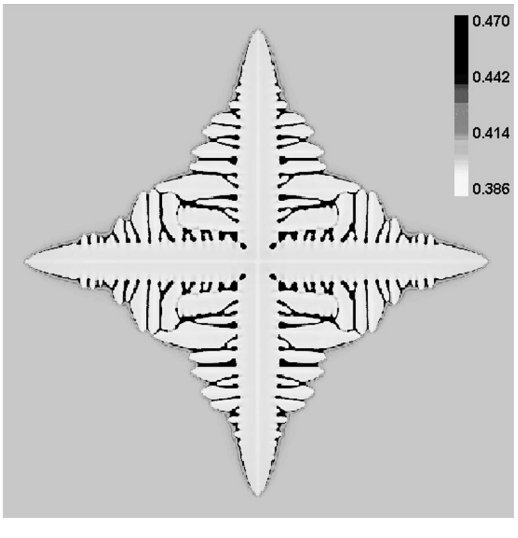

Fig. 2. Concentration field given by the non-isothermal model with temperature fixed on the boundary. All the physical and phase-field parameters are the same as in isothermal calculations. Time is 2.75 ms. The color scheme uses yellow–red palette in grey scale for low and high concentration values, respectively.

As one would expect, the temperature does not vary much, neither in time nor in space, for example, the spatial temperature difference does not exceed 1.6K all the time (Fig. 4). However, comparison of the solute patterns (Figs 1 and 2) shows that the composition behaviour is very sensitive to even small changes in the temperature field. Increased melt temperature reduces sources of instability, which leads to less developed structure of the non-isothermal dendrite. The length of the primary arms is about 6% less than the corresponding one calculated under isothermal conditions. The solute diffusion length is larger compared to the isothermal growth, as well as spacing of interdendritic liquid pockets. The value of the composition at the solid/liquid interface is decreased since the operating point in the phase diagram has moved to the left due to the increased temperature.

Figure 3 demonstrates spatial redistribution of the temperature field with imposed interface location at time 2.75 ms. As predicted by the Gibbs–Thomson condition, the tips are the coldest parts of the dendrite due to the large curvature here. The location of the hottest point during the crystal growth varies and in general corresponds to one of the tips of those sidebranches which grow towards each other and form a closed liquid pocket. Melt in this pocket is of highest temperature due to release of latent heat by these growing sidebranches. The less sharp the sidebranch tip, the higher temperature of the sidebranch.

The maximal value of the system temperature as a function of time is given in Fig. 4. The curve is slightly oscillating because the temperature is taken at different grid points wherever the maximum value occurs. The local peaks occur when two or more sidebranches growing towards each other merge and stop growing and consequently to produce the latent heat. Then another sidebranch surrounded by hot melt starts to release more latent heat than the others and becomes the hottest place in the system. Fig. 5 shows the area of the dendrite tip with imposed isotherms, which are refracted over the interface. This reflects the change of the temperature gradient owing to the release of latent heat.

The results presented in this section indicate clearly that for a supersaturated binary alloy the development of dendritic patterns is governed mainly by solute diffusion, but the temperature variation alters significantly the morphology of the microstructure.

5. RECALESCENCE CALCULATIONS

This section represents the results obtained for simulations of dendritic solidification in the thermal

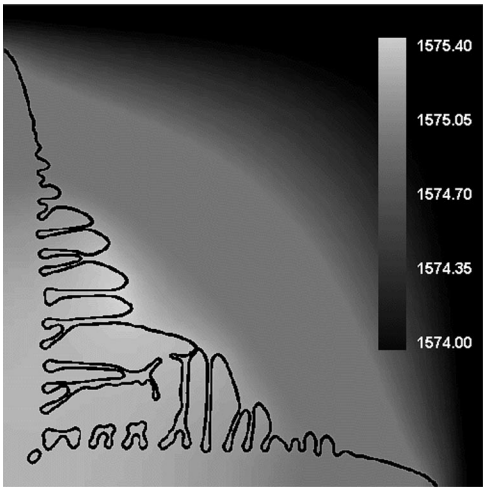

Fig. 3. Temperature field corresponding to the solute redistribution in Fig. 2. The lighter color, the higher the temperature. The solid/liquid interface is shown as a band where $0.1<\phi<0.9$. Time is 2.75 ms.

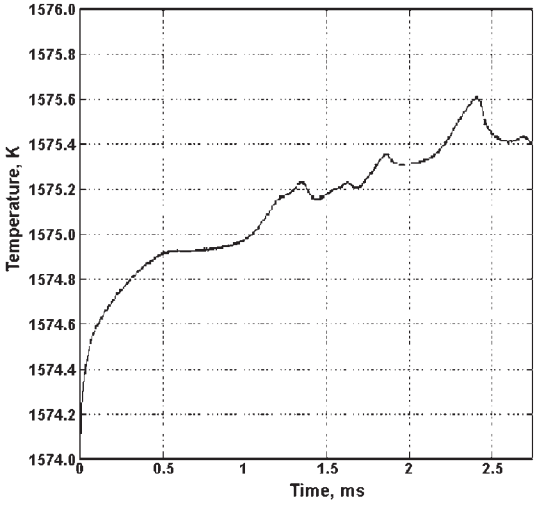

Fig. 4. Maximal temperature of the system vs time, minimal temperature $T=1574$K is kept on the boundary all the time.

regime when a heat flux is extracted from the domain. This regime is modeled in two ways: (a) the isothermal model is coupled with a heat balance [4] which neglects temperature variations in space

$$\frac{\mathrm{d}T}{\mathrm{d}t} = -\dot{T} + \frac{\Delta\tilde{H}}{\tilde{c}}\frac{\mathrm{d}}{\mathrm{d}t}\left[\frac{1}{S}\int_S \phi(x, y, t)d\mathrm{S}\right] \qquad (30)$$

where $\dot{T}$ is the cooling rate, S is the area of the domain, $\Delta\tilde{H}$ and $\tilde{c}$ are evaluated for the composition far away from the interface; (b) non-isothermal model with Neumann boundary conditions for the heat equation. The heat flux Q imposed on the outer boundary is related to $\dot{T}$ by $Q = \frac{\tilde{c}\dot{T}a}{4}$, where a is the side length of the computational domain.

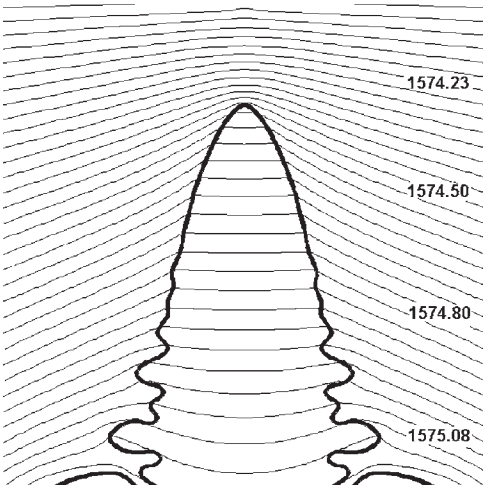

Fig. 5. Location of isotherms near the dendrite tip. The picture corresponds to the run in Fig. 3.

There is a lot of numerical and physical issues, which should be investigated for these types of simulations. In these calculations the effect of the cooling rate and the size of the domain is analyzed. The computations are performed in two square domains 6.9×10^{-5} and 2.28×10^{-5} m on a side (which will be referred to as "large" and "small" boxes), for three cooling rates: 2.1×10^{3}, 3.4×10^{4}, and 1.3×10^{5} K/s. In order to keep the same non-dimensional geometry, $\delta=1.62\times10^{-8}$ m is chosen for the "small" box.

Figure 6(a and b) shows the temperature–time history for all cooling rates, in the "big" and "small" box, respectively. Three curves represent each simulation: two dashed lines show the minimal and maximal value of the system temperature calculated by the non-isothermal model, the solid line is $T(t)$ obtained through the heat balance [equation (30)]. It is necessary to note that $T(t)$ calculated by the isothermal approach differs significantly (2K as the worst) from the short-term $T(t)$ dependence in Fig. 6 in Ref. [4]. $T(t)$ is very sensitive to the choice of numerical as well as physical parameters which were not unambiguously defined in Ref. [4].

In general, both the models give a similar $T(t)$ behaviour. Initially, at the highest cooling rates (3.4×10^{4} and 1.3×10^{5} K/s) the temperature falls down because the composition needs more time to be changed and to cause solidification. As a crystal starts to grow, the latent heat release increases the temperature, that is, recalescence occurs. For the lowest cooling rate, the initial growth of the nuclei is fast enough to overcome the imposed heat extraction rate and, hence, the temperature–time curve initially has a positive slope. $T(t)$ given by the isothermal model initially approximates an average temperature, but later the latent heat of fusion is released faster, and therefore, for all three cooling rates the time evolution is faster. As a result, the isothermal model gives an overestimated values of the temperature.

Comparison of the dashed curves in Fig. 6(a and

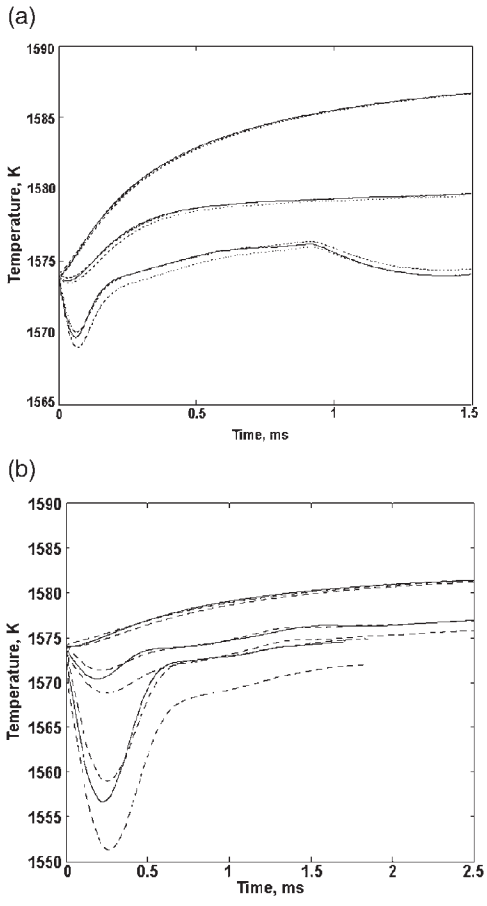

Fig. 6. Temperature–time dependence for the boxes of size 2.28×10^{-5} m (a) and 6.9×10^{-5} m (b). Results for the cooling rates 2.1×10^{3}, 3.4×10^{4}, and 1.3×10^{5} K/s are shown from top to bottom.

b) obtained for the same cooling rates shows the influence of the domain size. In outline, at the same time the temperature of the melt in the "large" box has a lower value than the temperature in the "small" domain. This feature can be explained by the fact that a larger box contains fewer nuclei per area, and thus, less latent heat is produced in the box. It is interesting to notice that a larger computational domain and higher heat extraction rate cause greater spatial variations of the temperature field. The maximum temperature alteration is ca 9° in the "large" box and 1.2° in the "small" one. The tendency of a slightly decreasing difference of maximum and minimum temperature as time goes is due to reducing fraction of melt. Therefore, the assumption made in Ref. [4] about absence of the temperature gradient in space can be accepted for a small computational domain with a low imposed heat extraction rate, but in other cases spatial variation of the temperature field should be taken into account.

The calculated growth morphologies vary significantly among the three cooling rates and the computational domains. Solute patterns and corresponding temperature fields are presented in Figs 7 and 8. Comparing these figures one should remember that the real side sizes of the boxes differ by a factor of three. At the lowest cooling rate [Figs 7(e) and 8(e)] the temperature rise reduces the melt undercooling which gives the least developed crystal. In this case the solidification is driven by solute change in both phases, solid and liquid. The higher the heat extraction rate, the greater the influence of the size of the computational domain on the crystal growth. While the dendritic morphology calculated in the "small" box [Fig. 7(c)] consists only of primary stalks with no perturbation on the interface, the corresponding morphology in the "large" box [Fig. 8(c)] has well developed secondary arms. It should be noted, that due to the high value of heat extraction rate the interface stays planar (which gives the crystal a diamond shape) before perturbations appear at the interface and secondary sidebranches start to develop.

The most intriguing morphology is presented in Fig. 8(a) and obtained for the highest cooling rate in the "large" domain. The morphology growth exhibits an almost circular shape with cells developing at the later times. The explanation is that for very high cooling rate, the solidification of a binary alloy is governed mainly by the heat transfer. When a melt freezes quickly, composition does not have time to be changed and to cause instability. The presence of solute trapping in this simulation is observed when the interface velocity V reaches its maximum value of 0.03 m/s, which corresponds to the largest undercooling of the melt. The partition ratio at the moment is $c_S/c_L = 0.97$, as opposed to an equilibrium value of 0.85.

The solute trapping effect in the phase-field models was studied in Ref. [15]. It was shown that for a planar interface the solute trapping occurs when the solute diffusion length ahead of the interface is comparable with the interface thickness $D_I/V\sim\delta$ where $D_I = D(\phi = 0.5)$. For the δ used in the calculations this gives $V=0.01$ m/s. The simulations of directional solidification [16] demonstrate that the interface remains stable for velocities above 0.024 m/s. Hence, qualitatively, the growth behaviour of the dendrite is consistent with the significant solute trapping.

It should be concluded that a crystal morphology depending on the heat extraction rate varies from smooth primary stalks without secondary arms (low cooling rate) to well-developed dendritic structure to planar or cellular shape at extremely high cooling rate.

6. CONCLUSIONS

The presented results are thought to be a first attempt to model non-isothermal dendritic solidification of a binary alloy. Removing the isothermal assumption makes the computations much more time consuming, due to the large difference between thermal and mass diffusivities.

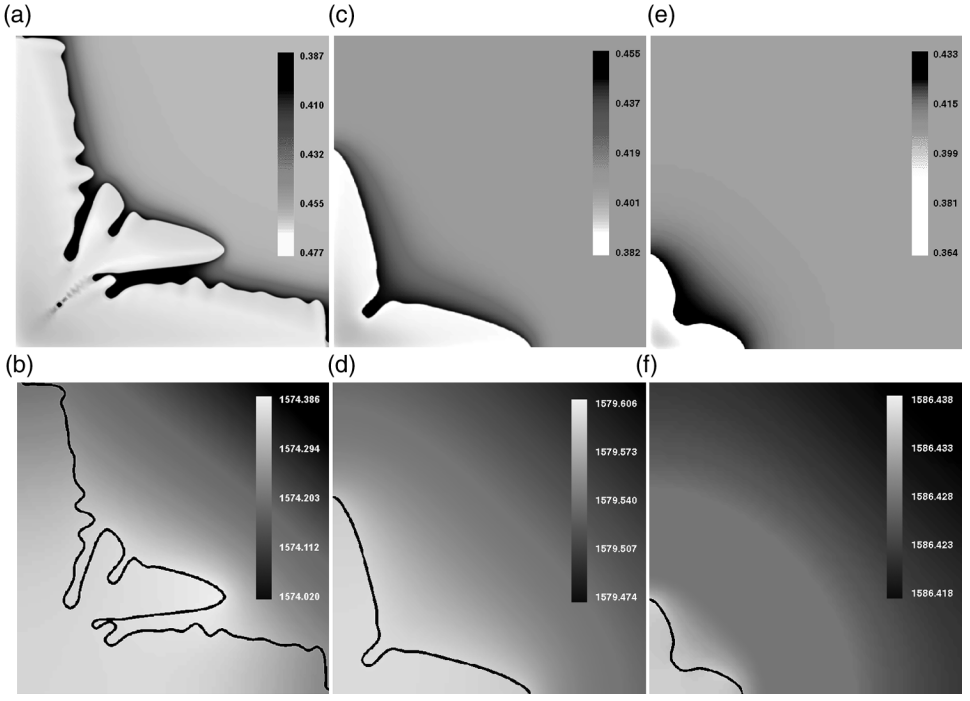

Fig. 7. Solute and temperature redistributions (top and bottom rows, respectively) obtained in the "small" box (2.28×10^{-5} m), for the cooling rates 1.3×10^5, 3.4×10^4 and 2.1×10^3 K/s varying from the left column to the right one. Time is 1.4 ms. The concentration and the temperature fields employ the same color scheme as in Figs. 2 and 3, respectively. The black line shown with the temperature field represents the location of the solid/liquid interface.

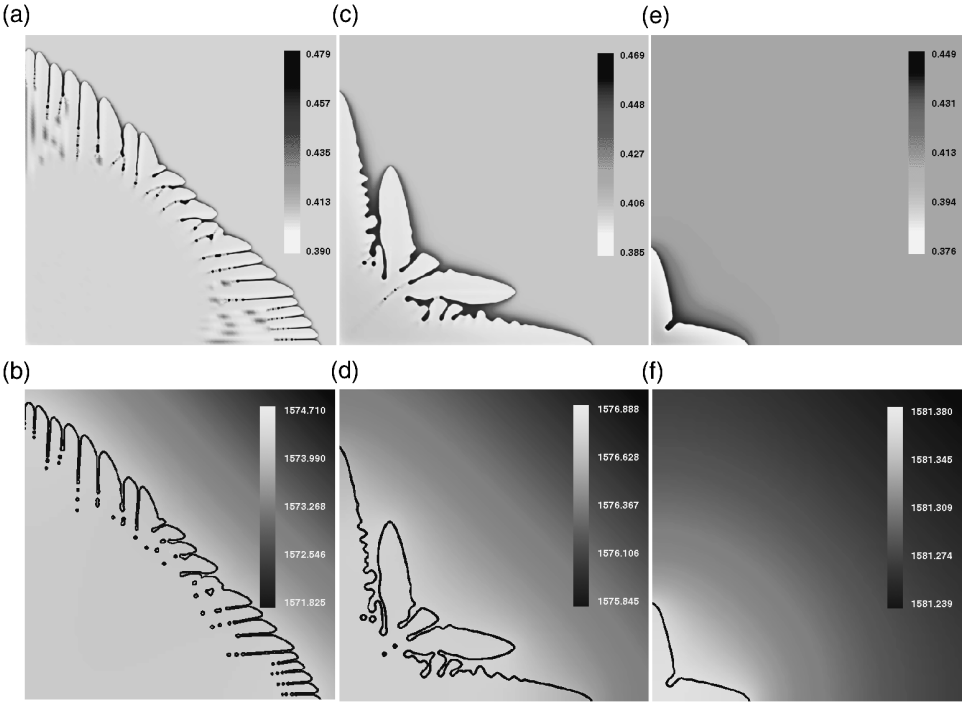

Fig. 8. Solute and temperature redistributions (top and bottom rows, respectively) obtained in the "large" box (6.9×10^{-5} m), for the cooling rates 1.3×10^5, 3.4×10^4 and 2.1×10^3 K/s varying from the left column to the right one. (a) and (b) are given at time 1.7 ms, while the others are at 2.5 ms.

For low cooling rate and many nuclei the spatial temperature variation is small and may be neglected, and thus the isothermal approach is applicable. However, the non-isothermal effect becomes visible for higher cooling rate and fewer nuclei, when the spatial temperature difference is not small compared to the difference between solidus and liquidus in the phase diagram.

On increasing the cooling rate, the growth eventually becomes governed by thermal diffusion rather than redistribution of solute. Due to limitations on the width of the diffuse interface the results for the highest cooling rate, showing strong solute trapping, may not be quantitatively correct. However, qualitatively the predicted behaviour is in agreement with what is expected at high cooling rates.

Acknowledgements—This work was supported by the Swedish Research Council for Engineering Science (TFR).

REFERENCES

1. Warren, J. A. and Boettinger, W. J., *Acta metal.*, 1995, **43**, 689.
2. Amberg, G., http://www.mech.kth.se/~gustava/femLego/.
3. Amberg, G., Tönhardt, R. and Winkler, C., *Math. Comput. Simulation*, 1999, **49**, 257.
4. Boettinger, W. J. and Warren, J. A., *Metall. Mater. Trans.*, 1996, **27A**, 657.
5. Caginalp, G. and Jones, J., *Ann. Phys.*, 1995, **237**, 66.
6. Tönhardt, R. and Amberg, G., *J. Crystal Growth*, 1998, **194**, 406.
7. Wang, S. -L., Sekerka, R. F., Wheeler, A. A., Murray, B. T., Coriell, S. R., Braun, R. J. *et al.*, *Physica D*, 1993, **69**, 189.
8. Caginalp, G. and Xie, W., *Phys. Rev. A*, 1993, **48**, 1897–1909.
9. Warren, J. A. and Murray, B. T., *Modeling Simulation Mater. Sci. Engng*, 1996, **4**, 215.
10. McCarthy, J. F., *Acta mater.*, 1997, **45**, 4077.
11. Warren, J. A., *IEEE Computational Science and Engineering*, 1995, **2**, 38.
12. Conti, M., *Phys. Rev. E*, 1997, **55**, 765.
13. Pavlik, S. G. and Sekerka, R. F., *Physica A*, 1999, **268**, 283.
14. Karma, A. and Rappel, W. J., e-print cond-mat/990201.
15. Ahmad, N. A., Wheeler, A. A., Boettinger, W. J. and McFadden, G. B., *Phys. Rev. E*, 1998, **58**, 3436.
16. Boettinger, W. J. and Warren, J. A., *J. Crystal Growth*, 1999, **200**, 583.

Paper 2

P2

Phase Field Modeling of Alloy Polycrystals

James A. Warren[1], Irina Loginova[2], László Gránásy[3],
Tamás Börzsönyi[3], Tamás Pusztai[3]

[1] Metallurgy Division and Center for Theoretical and Computational Materials Science
National Institute of Standards and Technology, Gaithersburg, MD 20899
[2] Department of Mechanics, KTH, SE-10044, Stockholm, Sweden
[3] Research Institute for Solid State Physics and Optics,
H-1525 Budapest, POB 49, Hungary

Abstract

Recent results using a phase field model of polycrystalline alloy dynamics are presented, using two numerical techniques: adaptive grids and parallel grids. The growth of alloy dendrites, and their subsequent impingement to form grain boundaries is demonstrated within the model, and topics for future research are discussed.

---

1. Introduction

Phase field models of solidification have enjoyed wide application in recent years because of the ease with which complex microstructures can be simulated with only a small set of differential equations derived from basic thermodynamics principles. [1, 2, 3, 4]. Phase field models are a subclass of the more generic diffuse interface models which are based on a functional representation of the free energy density in terms of specifiable field parameters $\{\phi_1(\vec{x}), \phi_2(\vec{x}, \ldots, \phi_N(\vec{x})\}$, where, for example, ϕ_i is an order parameter for a crystalline phase (i.e., Allen-Cahn [5]). The free energy density is expanded around the homogeneous (i.e. absence of gradient) free energy density, $f(\phi_i)$, with the addition of a penalty for interfaces (where $\nabla\phi_i \neq 0$.)

The traditional phase field model of solidification of a binary alloy material starts from the free energy

$$\mathcal{F} = \int dV \left[f(\phi, c) + \frac{\alpha^2}{2}\Gamma^2(\nabla\phi) \right], \tag{1}$$

where $f(\phi, c, T)$ is the homogeneous free energy density of an alloy of concentration c and temperature T in the solid ($\phi = 1$) and liquid ($\phi = 0$). The free energy density f, interpolates between the two bulk phases, and has the shape of a double well in ϕ, with minima (equilibrium) at $\phi = 0, 1$. The stationary states of the functional $\mathcal{F}[\phi, c, T]$ represent equilibrium values of ϕ. The time-evolution of this system can be written as local equations that are cast in terms of the functional gradients of $\mathcal{F}$ [6]. The calculations considered in this paper will be for an isothermal alloy, and thus we will ignore the temperature in subsequent discussions. Similar models of phase field statics and dynamics of alloys have been presented elsewhere, but with a focus on different phenomenology [7, 8, 9, 10]).

In Eqn. 1 the gradient energy coefficient α determines the magnitude of the penalty induced by the presence of interfaces. The competition between the desire of the system to remain in one of the bulk phase minima of f (liquid or solid) and the cost of high gradients results in a finite interface width. The function Γ also contains any anisotropy of the crystalline energy at the liquid-solid interface [11].

The phase field model given by Eqn. 1 has produced faithful simulations of solidification by using a single order parameter to identify a liquid and a solid phase. However, ideally the evolution of a *crystalline phase* - whether during solidification and impingement, coarsening, grain growth, or sintering - should not omit the physical effects of crystalline orientation, or of misorientation at grain boundaries. Recent work has allowed phase field models of solidification to be extended to include the effects of grain boundaries [12, 13, 14, 15, 16] and in particular, one of these models [12, 14, 17, 18] (and its extensions) has been used to produce polycrystalline microstructures of alloy dendrites. In this proceeding we will present a brief overview of the alloy model of grain growth, show some of the application areas, and show some of the methods by which solution is obtained.

2. The Model

We introduce the model of Kobayashi *et al* [12] as our starting point, modified to include alloy effects:

$$\mathcal{F} = \int dV \left[f(\phi, c) + \frac{\alpha^2}{2}\Gamma^2(|\nabla\phi|, \theta - \psi) + sg(\phi)|\nabla\theta| + \frac{\epsilon^2}{2}h(\phi)|\nabla\theta|^2 \right]. \quad (2)$$

In comparison with Eqn. 1, two terms have been added to Eqn. 2, associated with the energy cost of a grain boundary. Specifically, we have introduced an order parameter θ that represents the local orientation measured with respect to a fixed axis (in two dimensions) of the crystal lattice. The values of θ span $-\pi/N < \theta \leq \pi/N$, where N is the rotational symmetry of the underlying two-dimensional crystal lattice. The parameter ψ is defined as the direction of a normal to the level sets to ϕ, i.e. $\tan(\psi) = (\partial\phi/\partial y)/(\partial\phi/\partial x)$. The parameters s and ϵ are coupling constants and g and h are specified as ϕ^2, although quite generally they need only be monotonically increasing functions of ϕ. The monotonic nature of g and h is required if the effects of crystalline orientation are to be reduced or eliminated in the liquid phase.

The homogeneous free energy $f(\phi, c)$ takes a form introduced in elsewhere [8, 10]. As noted, in addition to the double well in ϕ, $f(\phi, c)$, in each phase the properties of an ideal solution are assumed, with parameters taken from the Ni-Cu system (c is the concentration of Cu.)

3. Solutions using adaptive grids

The above free energy, using the standard approach of irreversible thermodynamics, can be postulated to have the following relaxational dynamics:

$$\dot{\phi} = -M_\phi \frac{\delta F}{\delta \phi} \quad (3)$$

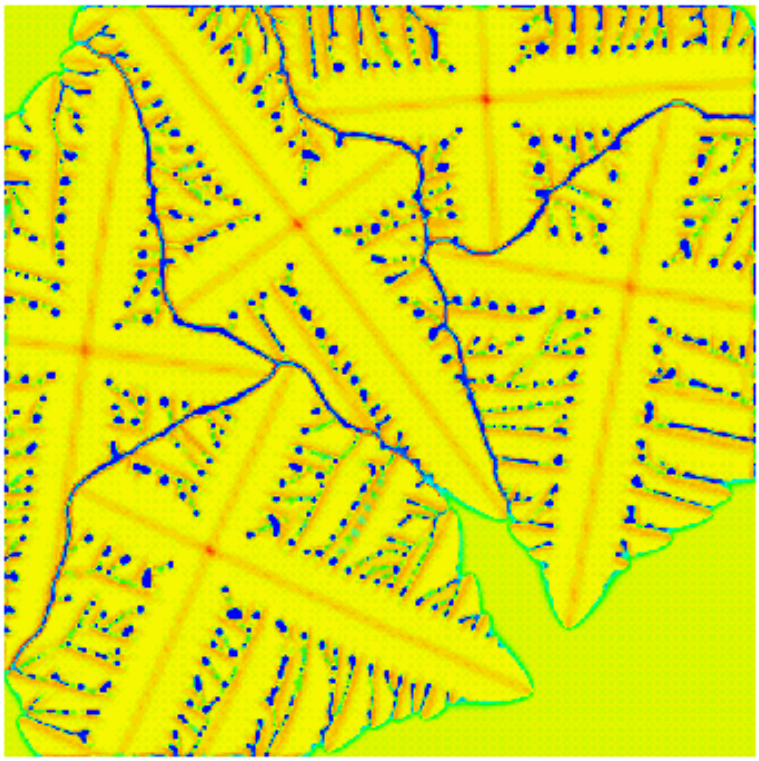

(a)

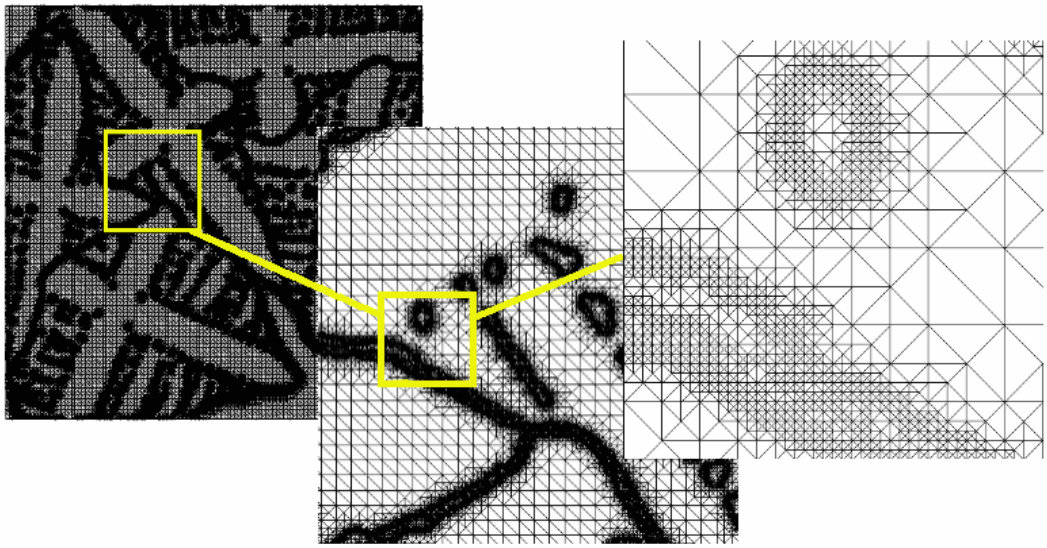

(b)

FIGURE 1. (a) Here we show a calculation on an adaptive grid of five simultaneously nucleated grains of differing orientation. The hues are the concentration of Cu in a Ni matrix (as in [10]). The dendrites grow towards impingement, but coalescence is inhibited by the energy cost of a forming grain boundary. The high resolution (and therefore high accuracy of the calculation) of the interface is shown in part (b), where the computational grid is shown, and two levels of magnification by a factor of three.

$$\dot{c} = \nabla \cdot \left(M_c \nabla \frac{\delta F}{\delta c} \right) \tag{4}$$

$$P\phi^2\dot{\theta} = -\frac{\delta F}{\delta \theta} \tag{5}$$

where $M_\phi(c)$ and $M_c(\phi)$ are mobilities and P is a function of $|\nabla\theta|$ ensuring a constant value of θ in the non-interface regions

$$P\left(\epsilon_\theta |\nabla\theta|\right) = 1 - e^{-\beta_1 \epsilon_\theta |\nabla\theta|} + \frac{\beta_2}{\epsilon} e^{-\beta_1 \epsilon_\theta |\nabla\theta|} \tag{6}$$

where β_1 and β_2 are constants. The variational derivatives in the right-hand sides of (3)-(5) can be evaluated as follows

$$\dot{\phi} = -M_\phi \left(\frac{\partial f}{\partial \phi} - \alpha^2 \sum_{k=1}^{2} \frac{\partial}{\partial x_k} \left(\Gamma \frac{\partial \Gamma}{\partial \phi_{x_k}} \right) + 2s\phi|\nabla\theta| + \epsilon_\theta^2 \phi |\nabla\theta|^2 \right) \tag{7}$$

$$\dot{c} = \nabla \cdot \left(M_c \left(\frac{\partial^2 f}{\partial c^2} \nabla c + \frac{\partial^2 f}{\partial c \partial \phi} \nabla \phi \right) \right) \tag{8}$$

$$P\left(\epsilon_\theta |\nabla\theta|\right) \phi^2 \dot{\theta} = \nabla \cdot \left[\phi^2 \left(\frac{s}{|\nabla\theta|} + \epsilon_\theta^2 \right) \nabla\theta \right] \tag{9}$$

For the details in the equations (7) and (8) the reader is referred to equations (3.1)-(3.9) in Ref.[10]. The factors of ϕ^2 in the equation (9) come from a desire for symmetry when the polar vector (ϕ, θ) is given a Cartesian representation $(\phi\cos\theta, \phi\sin\theta)$ [12]

Using the **femLego** framework[1], we are able to solve the above equations on adaptive grids, which are dynamically adjusted to variations of the solutions. In Fig. 1a we see a dendritic microstructure, with five nuclei introduced at $t = 0$. The dendrites grow towards impingement, but solute buildup and misorientation at the grain boundaries prevent coalescence. Fig. 1b shows the grid automatically generated by the **femLego** software [19]. As is evinced by the fineness of the mesh, this method allows for highly accurate solutions, and its properties under a variety of simulational environments are still being explored.

4. Solutions using parallel grids

Adaptive grid calculations are not trivially parallelizable because of necessary inhomogeneities introduced to increase the grid density where it is most needed. Using a fixed grid opens up another approach to solving the above equations: using a parallel grid system. One of the major advantages of parallel computations is the increase in size and decrease in real time over which large simulations can be done. For the study coarsening, nucleation or any other effect requiring good statistics, a large simulation requiring many nuclei must be implemented.

The model described in previous sections was modified to incorporate nucleation of crystalline particles [14], as opposed to the simultaneous introduction of nuclei

[1] available for free at http://www2.mech.kth.se/~gustava/femLego/ or http://www.ctcms.nist.gov

used above. This has been achieved by extending the orientation field to the liquid (where it is random and fluctuates). This notion of an ordered liquid is founded on the observation liquids have short range order. Note, that the evolution of crystalline atomic order (structural ordering) leads to the definition of crystal orientation as well (orientational ordering), i.e., they are two intimately related aspects of crystallization. In our model the phase and orientation fields are strongly coupled to mimic this, thus the structural and orientational ordering take place simultaneously at the crystal-liquid interface.

With these changes, our phase field model has been adapted for parallel processing using the message passing interface (MPI) protocol. This and the use of a GNU/Linux PC cluster consisting of 36 nodes allow us to perform large-scale simulations of nucleation and growth (e.g., on a 7000x7000 grid, yielding ≈ 720 dendritic particles; see Fig. 2), which provide satisfactory statistics for determining the Avrami-Kolmogorov exponent p, that characterizes the time evolution of solidification: $X(t) = 1 - \exp[-(t/t_0)^p]$ [20]. Here X is the solidified fraction and t_0 is a time constant. For the familiar Ni-Cu system (at $T = 1574$ K, and 0.8 supersaturation), we obtained $p \approx 3$ that satisfies the $p = 1 + d$ relationship (d is the number of dimensions), expected for constant nucleation and growth rates. This approach has been adapted to the regular solution model using interaction parameters that reproduce the Ag-Cu phase diagram. With its flower-like eutectic particles, the solidification patterns from the simulations (Fig. 3) closely resemble to those seen in laser melting experiments on Al-Si [21].

If orientational ordering is slow, a uniform orientation cannot be established along the perimeter of the particles, and polycrystalline particles form. (Note that in the case of low symmetry molecules orientational ordering might be the rate limiting factor for growth). It is worth mentioning that during this process the governing equations automatically take into account the free energy penalty for creating grain boundaries. Due to the intrinsic mechanism for nucleating new grains, our approach is able to model complex polycrystalline structures [22] such as spherulitic multidomains seen in polymeric [23] or electro-deposited systems [24].

5. Future directions

In this proceedings we have attempted to demonstrate the power of two complementary techniques for computing alloy microstructures using a phase field method. It is unlikely that either method will be designated superior, but instead each will find application in areas where the benefits of each method are evinced. The adaptive grid method promises high accuracy, and applicability to physically realistic parameter regimes, while the parallel approach allows for enormous calculations, yielding statistically significant results for studies such as nucleation and coarsening. It is likely that these methods can be unified under certain circumstances, resulting in a powerful tool-set for the prediction of microstructures.

References

[1] J. B. Collins and H. Levine, Diffuse interface model of diffusion-limited crystal growth, Physical Review B, vol. 31, pp. 6119-6122, 1985.

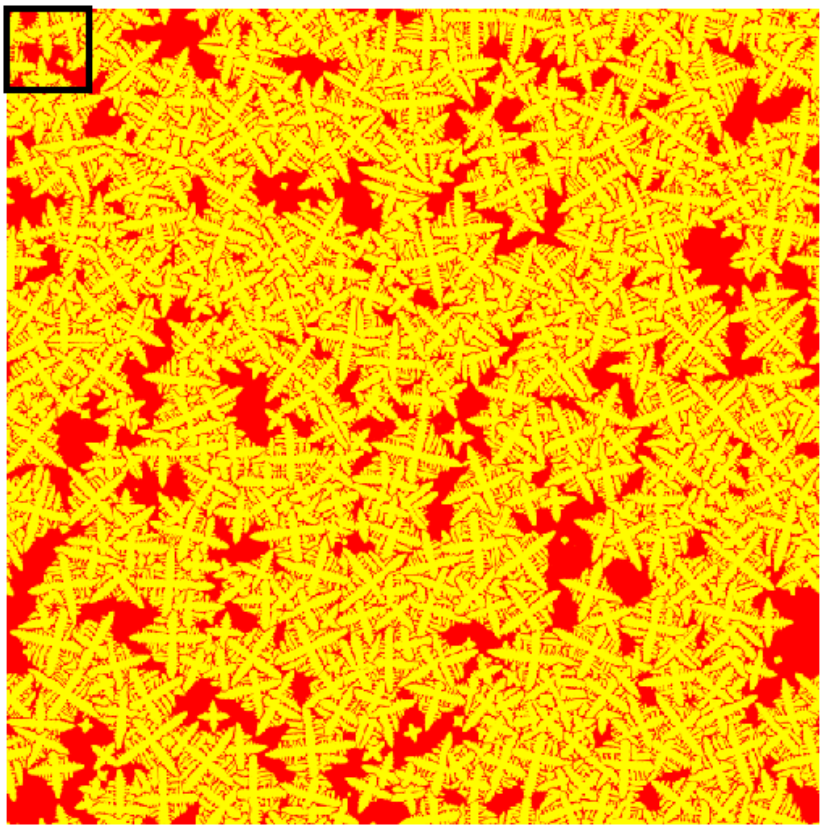

(a)

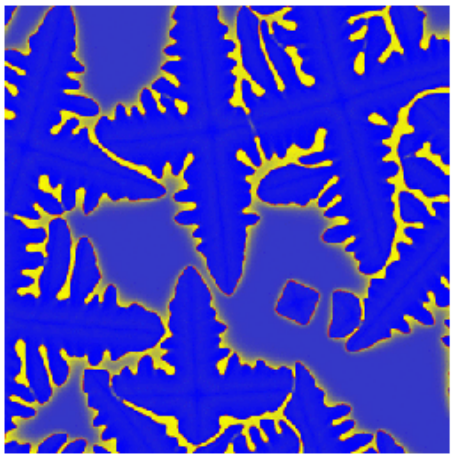

(b)

FIGURE 2. Here we show a calculation on a very large two dimensional grid (7000x7000). The calculation is optimally done on a parallel machine in order to render the computation in less than a month. In (a) the whole computational domain is shown for the phase field, while the concentration profile is shown in (b) for a the region bounded by the small box in (a).

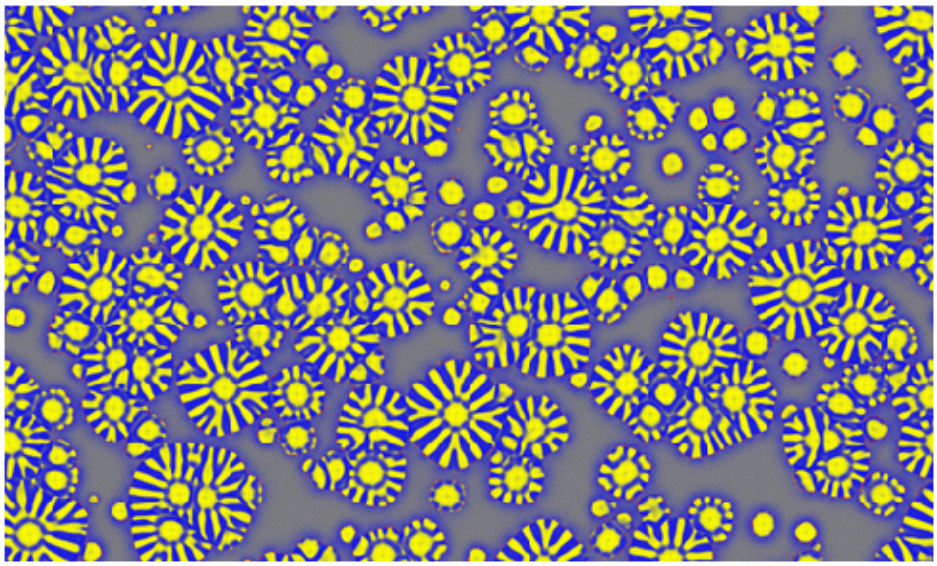

(a)

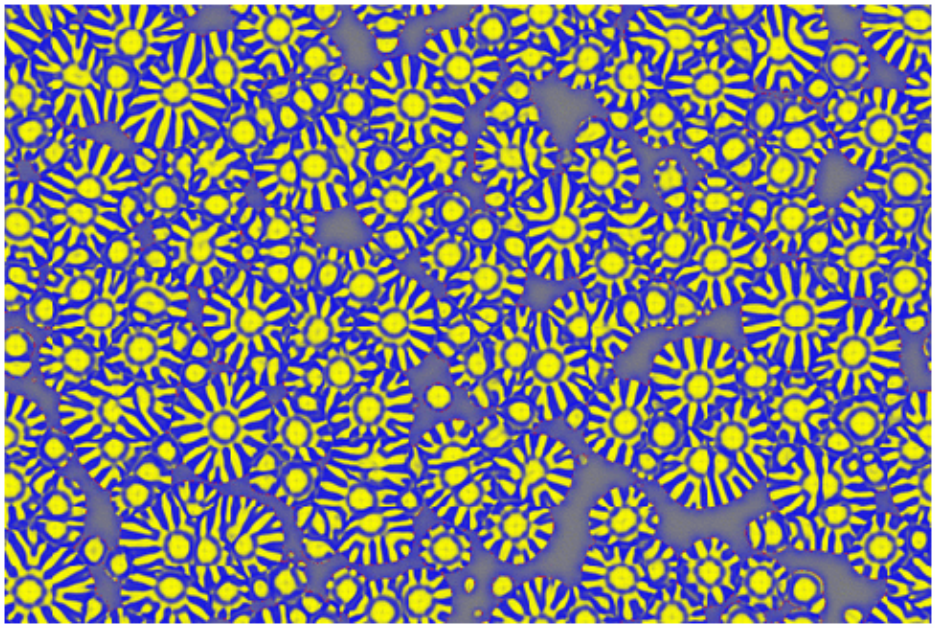

(b)

FIGURE 3. As a demonstration of additional techniques, we show a calculation of flower-like eutectic growth for a simple model Al-Cu system. In (a) we show a 1000x600 computation with 10% anisotropy in the surface energy anisotropy while in (b) we have a 1000x667 calculation with 5% anisotropy.

[2] J. S. Langer, Models of pattern formation in first-order phase transitions, in Directions in Condensed Matter Physics (G. Grinstein and G. Mazenko, eds.), p. 164, Philadelphia: World Scientific, 1986.
[3] G. Caginalp in Applications of Field Theory to Statistical Mechanics (L. Garrido, ed.), p. 216, Berlin: Springer, 1985.
[4] S.-L. Wang, R. F. Sekerka, A. A. Wheeler, B. T. Murray, S. R. Coriell, R. J. Braun, and G. B. McFadden Physica D, vol. 69, p. 189, 1993.
[5] S. M. Allen and J. W. Cahn, Microscopic theory for antiphase boundary motion and its application to antiphase domain coarsening, Acta Metall. Mater., vol. 27, no. 6, pp. 1085-95, 1979.
[6] W. C. Carter, J. E. Taylor, and J. W. Cahn, Variational methods for microstructural evolution, JOM, vol. 49, pp. 30-36, 1997.
[7] A. A. Wheeler, W. J. Boettinger, and G. B. McFadden Phys. Rev. A, vol. 45, p. 7424, 1992.
[8] A. A. Wheeler, W. J. Boettinger, and G. B. McFadden Phys. Rev. E, vol. 47, p. 1893, 1993.
[9] W. J. Boettinger and J. A. Warren, The phase field method:simulation of alloy dendritic solidification during recalescence, Met. Trans. A, vol. 27A, pp. 657-669, 1996.
[10] J. A. Warren and W. J. Boettinger Acta Met. et Mater., vol. 43, pp. 689-703, 1995.
[11] A. A. Wheeler and G. B. McFadden, A ξ-vector formulation of anisotropic phase-field models: 3d asymptotics, Euro. Journal of Applied Mathematics, vol. 7, pp. 367-381, 1996.
[12] R. Kobayashi, J. A. Warren, and W. C. Carter, A continuum model of grain boundaries, Physica D, vol. 140, pp. 141-150, 2000.
[13] L. Q. Chen and W. Yang, Computer simulation of the domain dynamics of a quenched system with a large number of nonconserved order parameters: The grain-growth kinetics, Phys. Rev. B, vol. 50, pp. 15752-6, 1994.
[14] L. Gránásy, T. Börzsönyi, and T. Pusztai, Nucleation and bulk crystallization in binary phase field theory, Phys. Rev. Lett., vol. 88, pp. art. no. 206105, 2002.
[15] M.Rappaz, A. Jacot, and W. J. Boettinger, Last stage solidification of alloys : a theoretical study of dendrite arm and grain coalescence, Metall. Transactions, p. in press, 2002.
[16] A. Jacot and M. Rappaz, A pseudo-front tracking technique for the modeling of solidification microstructures in multi-component alloys, Acta Materialia, vol. 50, pp. 1909-1926, 2002.
[17] A. E. Lobkovsky and J. A. Warren, Sharp interface limit of a phase field model of crystal grains, Phys. Rev. E, vol. 63, p. 051605, 2001. [18] W. J. Boettinger, J. A. Warren, C. Beckermann, and A. Karma, Phase field simulation of solidification, Annual Reviews of Materials Research, vol. 32, pp. 163194, 2002.
[19] G. Amberg, R. Tohardt, and C. Winkler, Finite element simulations using symbolic computing, Mathematics and Computers in Simulation, vol. 49, pp. 149165, 1999.
[20] J. W. Christian, The Theory of Transformations in Metals and Alloys. Pergamon, Oxford, 1981.
[21] D. R. Allen, M. Gremaud, and J. H. Perepezko Mater Sci. Eng. A, vol. 173, pp. 226-228, 1997.
[22] L. Gránásy, T. Börzsönyi, and T. Pusztai in Proc. Int. Workshop on Computational

Physics 2002 (H. Emmerich and B. Nestler, eds.), p. in press, Dresden: Springer, 2002.
[23] H. Keith Kolloid-Z. Z. Polymere, vol. 231, p. 421, 1966.
[24] V. Fleury Nature, vol. 390, p. 145, 1997.

Paper 3

P3

Pergamon

Available online at www.sciencedirect.com

SCIENCE DIRECT®

Acta Materialia 51 (2003) 1327–1339

Acta MATERIALIA

www.actamat-journals.com

The phase-field approach and solute drag modeling of the transition to massive $\gamma \rightarrow \alpha$ transformation in binary Fe-C alloys

I. Loginova [a], J. Odqvist [b,*], G. Amberg [a], J. Ågren [b]

[a] *Department of Mechanics, KTH, 100 44 Stockholm, Sweden*
[b] *Department of Materials Science and Engineering, KTH, 100 44 Stockholm, Sweden*

Received 18 April 2002; accepted 25 October 2002

Abstract

The transition between diffusion controlled and massive transformation $\gamma \rightarrow \alpha$ in Fe–C alloys is investigated by means of phase-field simulations and thermodynamic functions assessed by the Calphad technique as well as diffusional mobilities available in the literature. A gradual variation in properties over an incoherent interface, having a thickness around 1 nm, is assumed. The phase-field simulations are compared with a newly developed technique to model solute drag during phase transformations. Both approaches show qualitatively the same behavior and predict a transition to a massive transformation at a critical temperature below the T_0 line and close to the $\alpha/\alpha + \gamma$ phase boundary. It is concluded that the quantitative difference between the two predictions stems from different assumptions on how the properties vary across the phase interface yielding a lower dissipation of Gibbs energy by diffusion in the phase-field simulations. The need for more detailed information about the actual variation in interfacial properties is emphasized.

Keywords: Diffusion; Thermodynamics; Gibbs energy; Dissipation; Interfacial properties

1. Introduction

If austenite (γ) in low-carbon iron alloys is quenched to sufficiently low temperatures, but still above the martensite start temperature M_s, it will be decomposed by a massive transformation that yields a characteristic blocky or massive microstructure. The massive transformation is partitionless like the martensitic transformation, i.e. it does not involve any composition change, and thus long-range diffusion is unnecessary. The growth of massive ferrite (α) occurs with a constant growth rate that is more or less independent of crystallographic orientation relationships in contrast to the martensitic transformation. Thermodynamically a partitionless transformation $\gamma \rightarrow \alpha$ is possible below the T_0 temperature, at which α and γ of the same composition have same Gibbs energy. However, at what temperature the massive transformation really becomes kinetically possible has been a matter of considerable controversy over the years. It may be argued that if the interfacial reac-

* Corresponding author. Fax: +46-8-100411.
E-mail address: joakim@met.kth.se (J. Odqvist).

1359-6454/03/$30.00
doi:10.1016/S1359-6454(02)00527-X

tions of the migrating α/γ are rapid enough the interface will be essentially in thermodynamic equilibrium, the so-called local equilibrium hypothesis. In that case the transition to a massive mode of transformation would occur when the undercooling is so large that the composition of the parent γ falls on the $\alpha/\alpha + \gamma$ phase boundary of the binary Fe–C phase diagram. On the other hand it has been claimed that the massive transformation may occur far inside the $\alpha + \gamma$ two-phase field. The subject and the different viewpoints were recently discussed in an extensive review by Hillert [1]. He emphasized that the interactions between solutes and the migrating phase interface are essential in order to understand the transition to the massive mode of transformation. It is thus necessary to analyze the so-called solute drag effect in detail. Hillert and Sundman [2] were first to show by simulation that the solute drag effect during solidification of binary alloys predicts a transition to a partitionless mode of solidification at high undercoolings. Their approach was to solve a steady state diffusion equation over the interfacial region and evaluate the part of the available driving force that is dissipated by diffusion. Diffusion in the parent liquid was treated analytically by a Zener–Hillert type of approach. Ågren et al. [3,4] replaced the diffusion profile inside the phase interface with a single representative composition and were able to model the transition between Widmanstätten growth of α into γ and a partitionless mode of transformation at high supersaturations.

Over the last decade the phase-field approach has been tremendously successful in predicting microstructures during solidification [5] and solid state transformations [6]. In this approach the interface between two phases is treated as a region of finite width having a gradual variation of the different state variables, i.e. the diffuse interface model. So far, neither the actual properties of the interface nor the thermodynamic and kinetic properties of the alloys have been emphasized. The attention has mainly been drawn to the capability of the method to predict very realistic microstructures and the treatment of the interface has been regarded as a mathematical "trick" to solve the difficult moving boundary problem.

Nevertheless, the physical pictures behind the solute drag modeling and the phase-field approach are very similar. Of course, the similarity is usually less evident because the interface thickness used in the numerical phase-field calculations has been much too large to have any physical significance. However, recently Ahmad et al. [7] compared the phase field model with various solute-drag models and they found that under steady-state conditions the two approaches are indeed very similar and the phase-field calculations will exhibit both solute trapping (massive growth) and solute-drag effect. Their results thus suggest that the phase field approach is capable of treating the transition to massive transformation as well as solute drag effects provided that the interface is given realistic properties.

The purpose of the present report is to apply the phase-field method to the $\gamma \rightarrow \alpha$ transformation in binary Fe–C and demonstrate that a transition to massive transformation is predicted during isothermal growth if reasonable properties are given to the α/γ phase interface. The predictions will be compared with a newly developed technique to model solute drag and we shall investigate under what conditions the two approaches are qualitatively or even quantitatively consistent. No comparison will be made with other solute-drag treatments e.g. sharp-interface models.

The main purpose is thus to study the situation at the phase interface and all calculations will be made for a one-dimensional geometry although the phase-field formulation is readily extended to the full three-dimensional geometry.

2. Phase field formulation of the $\gamma \rightarrow \alpha$ transformation in Fe–C

The phase-field formulation of the isobarothermal $\gamma \rightarrow \alpha$ transformation is based on the Gibbs energy functional:

$$G = \int_{\Omega} \left(\frac{G_m(\phi, u_C, T)}{V_m} + \frac{\varepsilon^2}{2} |\nabla \phi|^2 \right) d\Omega \tag{1}$$

where G_m denotes the Gibbs energy per mole of substitutional atom and V_m is the molar volume per

substitutional atom and will be approximated as constant, Φ is the phase-field variable taken 0 in α and 1 in γ. The u-fraction u_C is defined from the normal mole fraction of C, x_C as

$$u_C = \frac{x_C}{1-x_C} \tag{2}$$

As already mentioned, the temperature T is assumed constant all over the whole system. However, it may of course vary in time but heat conduction is assumed so rapid that all temperature gradients can be neglected. The molar Gibbs energy G_m is postulated as a function of the phase-field variable:

$$G_m = (1-p(\phi))G_m^\alpha + p(\phi)G_m^\gamma + g(\phi)W \tag{3}$$

where

$$g(\phi) = \phi^2(1-\phi)^2 \tag{4}$$

$$p(\phi) = \phi^3(10-15\phi + 6\phi^2) \tag{5}$$

and the choice of the parameter W will be discussed later. G_m^α and G_m^γ denote the normal Gibbs energy functions of the α and γ phases and are taken from the assessment of Gustafson [8]. The complete expressions are given in Appendix A. It should be mentioned that $g(\phi)$ and $p(\phi)$ have been chosen so that $dp/d\phi = 30g(\phi)$.

The evolution of the phase-field variable Φ is governed by the Cahn–Allen equation [9]

$$\dot{\phi} = -M_\phi\frac{\delta G}{\delta\phi} = -M_\phi\left(\frac{1}{V_m}\frac{\partial G_m}{\partial\phi}-\varepsilon^2\nabla^2\phi\right) \tag{6}$$

The kinetic parameter M_ϕ is related to the interfacial mobility as will be shown later.The evolution of the concentration field is governed by the normal diffusion equation. When u-fractions are used and the molar volume is approximated as constant the normal diffusion equation can be rewritten as

$$\frac{\dot{u}_C}{V_m} = -\nabla\cdot J_C \tag{7}$$

The diffusional flux of carbon J_C is given by the Onsager linear law of irreversible thermodynamics:

$$J_C = -L''\nabla\left(\frac{\delta\, G}{\delta\, u_c}\right) \tag{8}$$

The quantity $\delta G/\delta u_C$ is the normal chemical potential of C denoted by μ_C. If the so-called gradient terms are neglected we have$\partial\, G_m/\partial\, u_C = \mu_C$ and Eq. (8) may be expanded in terms of the concentration and phase-field gradients

$$J_C = -\frac{1}{V_m}D_C\nabla u_C - L''\frac{\partial^2 G_m}{\partial u\partial\phi}\nabla\phi \tag{9}$$

The first term corresponds to the normal Fick's law and we may thus identify the normal diffusion coefficient of C as

$$D_C = V_m L''\frac{\partial^2 G_m}{\partial u_C^2} \tag{10}$$

The second-order derivative corresponds to Darken's thermodynamic factor and the parameter L'' is related to the diffusional mobility [10] M_C by means of

$$L'' = \frac{u_C}{V_m}y_{Va}M_C \tag{11}$$

where y_{Va} denotes the fraction of vacant interstitials, i.e. 1-u_C for γ and $y_{Va} = 1-u_C/3$ for α. For a given C content the fraction of vacancies would thus depend on the character of the phase, i.e. it will depend on the phase-field variable. We have postulated

$$u_C y_{Va} = (1-p(\phi))u_C(1-u_C/3) + p(\phi)u_C(1-u_C) \tag{12}$$

The diffusional mobility in the two phases could differ by several orders of magnitude, therefore we have chosen the following combination:

$$M_C = (M_C^\alpha)^{1-p(\phi)}(M_C^\gamma)^{p(\phi)} \tag{13}$$

For substitutional solutes the mobility in the center of the interface is most probably much higher than in the any of the crystalline phases. For interstitial solutes like carbon it may not be much higher and the approximation represented by Eq. (13) may not be too crude. The mobilities of carbon in α and γ were taken from Ågren [11,12]. The complete expressions are given in Appendix B.

3. Solute drag modeling of the $\gamma \rightarrow \alpha$ transformation in Fe–C

In the solute drag modeling the thickness (δ) of the interface is considered small enough compared to the curvature of the interface to approximate the diffusion field inside the interface as planar, see e.g. in ref. 2. The steady-state solution of Eq. (7) will be a good approximation inside the interface because it is so much thinner than the distance it travels. Eq. (7) takes the form

$$\frac{v}{V_m}(u_C - u_C^{\alpha}) = J_C \tag{14}$$

where v is the interface migration rate. The flux is given by Eqs. (8) or (9) and is set to 0 in the growing α phase. For a given combination of v and u_C^{α} the solution of Eq. (14) yields a concentration profile across the interface and thus also the C content on the γ side of the interface, i.e. $u_C^{\gamma/\alpha}$.

The dissipation of Gibbs energy due to diffusion inside the interface, expressed per mole of Fe and defined as positive, is given by

$$\Delta G_m^{diff} = -\frac{V_m}{v}\int_{\delta} J_C \frac{d\mu_C}{d\,z} dz \tag{15}$$

By combining Eqs. (14) and (15) and making use of $\partial\, G_m / \partial\, u_C = \mu_C$ one obtains

$$\Delta G_m^{diff} = -\int_{\delta} (u_C - u_C^{\alpha}) \frac{d\,\partial\, G_m}{d\,z\,\partial\, u_C} dz \tag{16}$$

In order to perform calculations the variation in thermodynamic properties and mobility inside the phase interface must be known. In the solute drag theory G_m is postulated as a function of both distance and composition. Several choices are possible. One choice is to use Eqs. (3) and (13) inside the interface but rather than Eqs. (4) and (5) one simply postulates that $g(\phi) = 0$ and $p(\phi) = z/\delta$. This approach was taken by Hillert and Sundman [2] and will be used in the present report.

The interface has a finite mobility due to interfacial friction and often a linear relation between interface migration rate and driving force is observed experimentally, i.e.

$$v = \frac{M}{V_m}\Delta G_m^i \tag{17}$$

where ΔG_m^i is the driving force needed to move the interface and M is the interfacial mobility. ΔG_m^i is defined positive for a spontaneous reaction and is the Gibbs energy dissipated by the interface friction. The total Gibbs energy dissipated in the interface is thus given by the sum of ΔG_m^{diff} and ΔG_m^i. The dissipation must be supplied from the total driving force available over the interface. It is given per mole of atoms and expressed in terms of the individual chemical potentials on p. 152 in ref. [13]. By instead introducing the Gibbs energy per mole of Fe, G_m, and its first derivative we obtain

$$\Delta G_m^{tot} = G_m^{\gamma} - G_m^{\alpha} - (u_C^{\gamma/\alpha} - u_C^{\alpha}) \frac{\partial G_m^{\gamma}}{\partial\, u_C^{\gamma}} \tag{18}$$

where ΔG_m^{tot} is defined as positive for the considered reaction to occur. For a given migration rate v we may, by combining Eqs. (9), (14) and (16)–(18) find the u_C^{α} and $u_C^{\gamma/\alpha}$ that makes the dissipated Gibbs energy exactly matchΔG_m^{tot}. In the limit of low migration rates u_C^{α} and $u_C^{\gamma/\alpha}$ will approach the local equilibrium values predicted by the phase diagram but at high velocities they will approach each other.

The solute-drag modeling of the interfacial reactions may be combined with a treatment of C diffusion in γ ahead of the interface. By such an approach it is possible to describe the gradual deviation from local equilibrium as the interface migration rates increases. In principle such modeling could be based on numerical methods as in the DICTRA software [14] or semi-analytical methods as the Green function formalism used recently by Enomoto [15]. For the sake of simplicity we will here take a simpler approach based on the linear-gradient approximation. For the thickening of a grain-boundary precipitate it yields the following expression

$$v = \frac{D}{2\ell} \frac{(u_C^{\gamma/\alpha} - u_C^{\gamma\infty})^2}{(u_C^{\alpha} - u_C^{\gamma/\alpha})(u_C^{\alpha} - u_C^{\gamma\infty})} \tag{19}$$

where ℓ is half the thickness of the grain-boundary precipitate and $u_C^{\gamma\infty}$ is the carbon content in γ far away from the interface, i.e. the initial content of

γ. By combining Eq. (19) with the previous result we may calculate the thickness corresponding to a given velocity. It should be emphasized that the solute drag calculations may be performed independently of the alloy composition $u_C^{\gamma\infty}$. As already mentioned, we then obtain u_C^{α} and $u_C^{\gamma/\alpha}$ as functions of migration rate v at a given temperature. For a particular alloy content $u_C^{\gamma\infty}$ we may use Eq. (19) to establish a relation between v and ℓ.

4. Approximate equivalence of the two approaches for Fe–C

In order to demonstrate the similarity between the phase-field and solute drag approaches Ahmad et al. [7] considered a planar case and the steady state formulation of the phase field, i.e.

$$\dot{\phi} = -v\frac{d\phi}{dz} \tag{20}$$

where $\dot{\phi}$ is given by Eq. (6). Their approach will now be applied to the $\gamma \rightarrow \alpha$ transformation and it will thus be slightly modified. However, for the convenience of the reader the derivation will now be given in some detail.

By multiplying both sides of Eq. (20) with $d\phi/dz$ and integrating across the interfacial region, with a thickness δ, we obtain

$$-\int_{\delta} M_{\phi}\left(\frac{1}{V_m}\frac{\partial G_m}{\partial \phi}\frac{d\phi}{dz} - \varepsilon^2\frac{d^2\phi}{dz^2}\frac{d\phi}{dz}\right)dz = -v\int_{\delta}\left(\frac{d\phi}{dz}\right)^2 dz \tag{21}$$

Applying integration by parts we find that the last term inside the left-hand side integral vanishes because $d\phi/dz = 0$ outside the interfacial region. The first term may be expanded because

$$\frac{dG_m}{dz} = \frac{\partial G_m}{\partial \phi}\frac{d\phi}{dz} + \frac{\partial G_m}{\partial u_C}\frac{du_C}{d\,z} \tag{22}$$

and Eq. (21) thus becomes

$$-\int_{\delta} M_{\phi}\frac{1}{V_m}\left(\frac{dG_m}{dz} - \frac{\partial G_m}{\partial u_C}\frac{du_C}{dz}\right)dz = -v\int_{\delta}\left(\frac{d\phi}{dz}\right)^2 dz \tag{23}$$

i.e.

$$-M_{\phi}\frac{1}{V_m}\left[(G_m^{\gamma} - G_m^{\alpha}) - \int_{\delta}\left(\frac{\partial G_m}{\partial u_C}\frac{du_C}{dz}\right)dz\right] = -v\int_{\delta}\left(\frac{d\phi}{dz}\right)^2 dz \tag{24}$$

Integrating Eq. (16) by parts and rearranging we find

$$\int_{\delta}\left(\frac{\partial G_m}{\partial u_C}\frac{du_C}{dz}\right)dz = (u_C^{\gamma/\alpha} - u_C^{\alpha})\frac{\partial G_m^{\gamma}}{\partial u_C} + \Delta G_m^{diff} \tag{25}$$

Inserting Eq. (25) in Eq. (24) and dropping the minus sign on both sides yield

$$M_{\phi}\frac{1}{V_m}\left[(G_m^{\gamma} - G_m^{\alpha}) - (u_C^{\gamma/\alpha} - u_C^{\alpha})\frac{\partial G_m^{\gamma}}{\partial u_C} - \Delta G_m^{diff}\right] = v\int_{\delta}\left(\frac{d\phi}{dz}\right)^2 dz \tag{26}$$

By comparing Eqs. (18) and (26) we find

$$M_{\phi}\frac{1}{V_m}[\Delta G_m^{tot} - \Delta G_m^{diff}] = v\int_{\delta}\left(\frac{d\phi}{dz}\right)^2 dz \tag{27}$$

The quantity inside parentheses on the left-hand side is clearly ΔG_m^i in Eq. (17) and it only remains to evaluate the integral on the right-hand side of Eq. (27). It should be emphasized that the left-hand side of Eq. (27) comes out as an exact result when steady state is assumed. The right-hand side is more difficult but Ahmed et al. assumed it was more or less independent of the quantities on the left-hand side and set

$$M_{\phi}\frac{1}{V_m}[\Delta G_m^{tot} - \Delta G_m^{diff}] = va \tag{28}$$

Comparing Eqs. (28) and (17) we may thus identify.

$$M = \frac{1}{a}M_{\phi} \tag{29}$$

where $a = \int_{\delta} (d\phi/dz)^2 dz$. For the simple case where we approximate the variation in ϕ as linear inside the interface we obtain $a = 1/\delta$. However, it should be emphasized that generally the interface thickness is less well defined for a diffuse interface than in solute drag modeling. In principle the interface extends over the whole region where ϕ varies, which is strictly $-\infty < z < \infty$ for the diffuse interface. Thus, the integration should be performed over that region. However, in practice it may yield sufficient accuracy to extend the integration over a finite region somewhat thicker than the thickness used in solute drag modeling. In the present case a more realistic variation in ϕ is given by the equilibrium solution of Eq. (6):

$$\phi = \frac{1}{2}\left[1 + \tanh\left(z/\sqrt{2}\delta\right)\right] \tag{30}$$

where $\delta = \varepsilon/\sqrt{W/V_m}$. By numerical integration over a the region $-3\delta < z < 3\delta$ and adopting Eq. (30) one obtains $a = 0.235/\delta$.

5. Physical parameters

As already mentioned, the complete set of thermodynamic and kinetic parameters for the Fe–C system is given in appendices A and B, respectively. The phase-field mobility M_ϕ is related to the conventional interfacial mobility M by means of Eq. (29). In the present study different choices of a will be tested. The interface thickness will be chosen as $\delta = 10^{-9}$ m. For a pure element the parameters W, ϵ, δ and the surface energy σ are related as follows [16]:

$$W = \frac{\sigma}{\delta} V_m \frac{6}{\sqrt{2}} \tag{31}$$

$$\sigma = \varepsilon\sqrt{\frac{W}{18V_m}} \tag{32}$$

i.e. $\varepsilon^2 = 3\sqrt{2}\sigma\delta$. With the surface energy $\sigma = 1$ J/m^2 and $V_m = 7\ 10^{-6}$ m^3 mol^{-1} we obtain W = 29.698 10^3 J/mol $\varepsilon^2 = 4.24\ 10^{-9}$ J/m. We shall assume that W and ϵ are independent of temperature and composition.

6. Numerical details

6.1. Phase-field simulations

The standard second order central difference in space and first order in time transform Eqs. (6) and (7) into a discrete problem. Zero Neumann boundary conditions are applied for both variables. The resulting non-linear systems of equations are solved using the Newton–Raphson method.

From the experimental observations, we expect two different regimes: "slow" growth, controlled by C diffusion in γ, and "fast" massive growth controlled by the interfacial reactions. During slow growth, we thus expect a parabolic behavior with an interface velocity v that is essentially proportional to $1/\sqrt{t}$ except for the later stages when impingement sets in and the system finally approaches the state of equilibrium. During the "fast" or partitionless growth, the solution should yield a single concentration spike traveling with constant velocity v until all the initial γ is transformed into α. In order to simulate these regimes the time step is adjusted to the interface dynamics according to

$$\Delta t = \frac{ch}{v} \tag{33}$$

where h is the space resolution in a uniform grid and c is the Courant number taken as 0.01. With this approach simulations of massive growth are performed with constant time step equal to its initial value $3.5\cdot 10^{-10}$ s. In the case of parabolic growth, the time step is gradually increased and at the final time, when the equilibrium is nearly achieved, Δt is 10^6 times larger than initially. The choice of the grid resolution was verified based on the known content of carbon in both phases at the equilibrium. With $h = 0.1125$ nm the relative error of equilibrium u_C is 1.2%. Another test is that the slope of the interface position vs $\sqrt{t}$ is a constant except for the later stages.

6.2. Solute drag simulations

The steady-state diffusion equation, i.e. Eq. (14), reduces to an ordinary differential equation for the

concentration of each solute over the interface. A variable order backward differentiation formula, usually referred to as Gear's method [17], is used to solve this differential equation. We have used the algorithm of Gear's method that is implemented in the HARWELL Subroutine Library [18].

7. Results

7.1. Phase-field simulations

Phase-field simulations were performed at a number of temperatures and alloy contents. The size of the system was 10 μm, corresponding to an austenite grain size of 20 μm if ferrite is formed at the austenite grain boundaries. As mentioned earlier, δ was chosen to be 10^{-9} m. Thus both the size of the system and the interface thickness were given physically realistic values. In a first set of calculations the parameter a in Eq. (29) was chosen as $1/\delta$, i.e. $M_\phi = M/\delta$ was applied in the phase-field equation.

The initial state was always homogeneous γ with a very thin layer of α (~ 4.5 nm) formed at the left side of the system. The composition of the initial layer of α was taken as $0.1 \cdot u_C^{\gamma\infty}$ if parabolic growth was expected. However, the composition of this layer does not affect the calculation because it is adjusted automatically during the first few time steps. In case of massive growth the initial composition was uniform over the domain.

As an example, Fig. 1 shows the concentration profile for an alloy with $u_C^{\gamma\infty} = 0.01$ at $T = 1093$ K and different instances $t = 1, 10, 20, \ldots, 60$ s. Fig. 2 shows the half thickness ℓ as a function of $\sqrt{t}$. As can be seen, the growth is indeed parabolic up to $t = 10$ s where impingement sets in. These results are in excellent agreement with DICTRA [14] simulations using the same set of data. The DICTRA simulations are based on a sharp interface model and local equilibrium at the interface. At the same temperature a completely different behavior is found for an alloy with $u_C^{\gamma\infty} = 0.001$. In this case the massive growth occurred with a constant growth rate of ca. 0.1 m/s until all γ was transformed into α. The concentration profile, a traveling wave, is shown in Fig. 3.

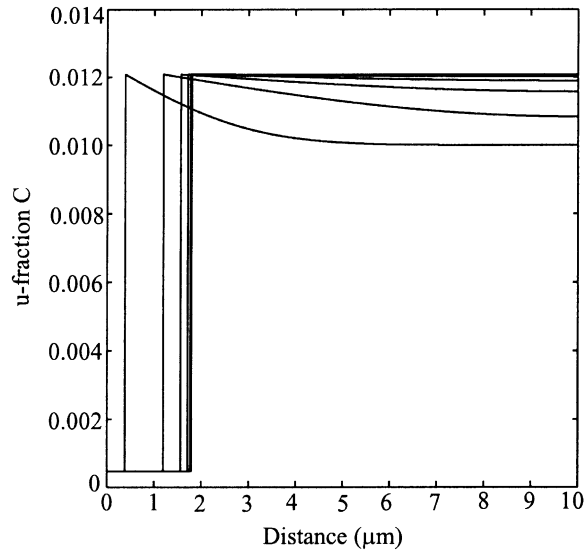

Fig. 1. Phase-field calculation of carbon concentration profiles at different instances, t = 1, 10, 20,… 60 s. $u_C^{\gamma\infty} = 0.01$ at $T = 1093$ K.

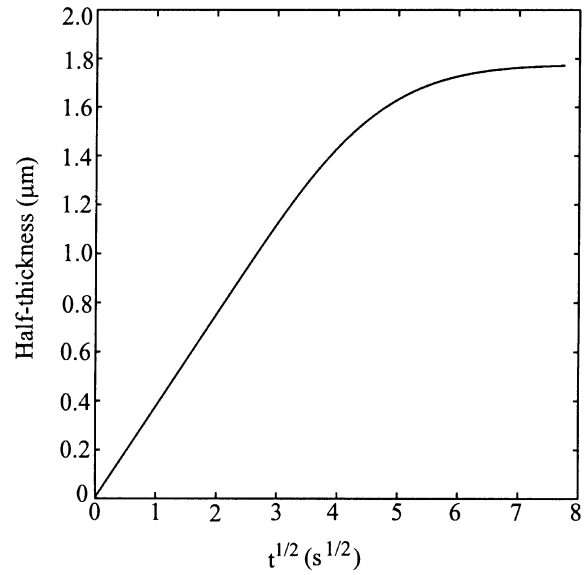

Fig. 2. Phase-field calculation of half-thickness of ferrite precipitate as function of $\sqrt{t}$.

By performing phase-field simulations for a large number of alloy compositions at each tem-

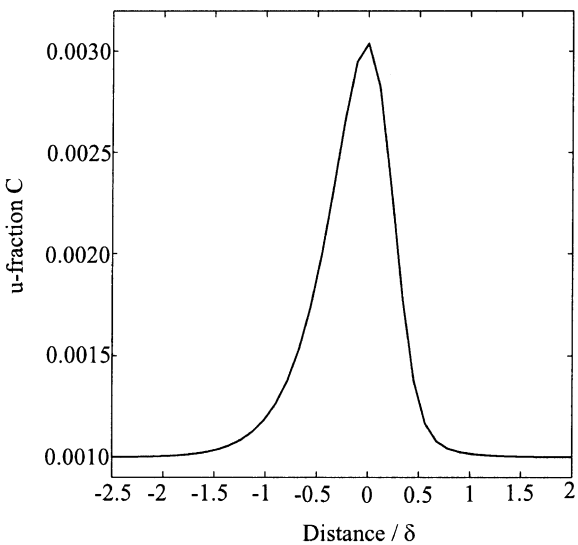

Fig. 3. Phase-field calculation of carbon concentration profile at interface during massive growth of ferrite, $v = 0.1$ m/s, for $u_C^{\infty} = 0.001$ at $T = 1093$ K.

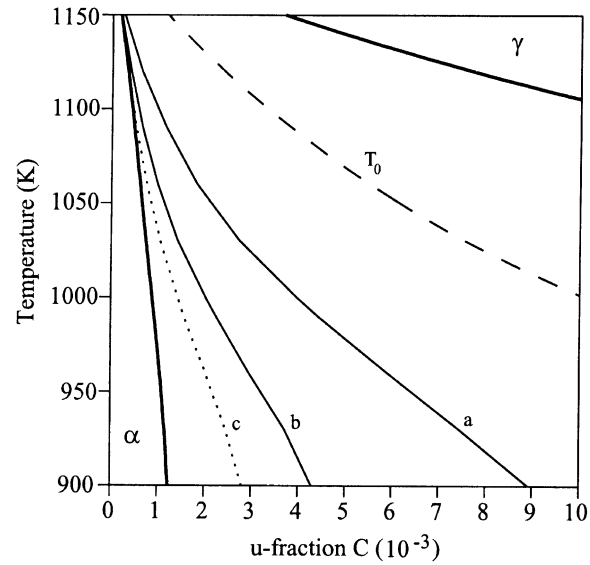

Fig. 4. Calculated Fe–C phase diagram with the T_0 line superimposed. Curves a and b are the critical compositions from phase-field simulations using different choices of M_ϕ: a) M/δ and b) $0.235M/\delta$. Curve c) is the critical composition from solute-drag simulations. M is given in Appendix B.

perature it is possible to establish a critical composition below which the massive growth occurs at that temperature. Of course the critical composition depends on the value of M_ϕ. In Fig. 4 we have superimposed, on a part of the calculated Fe–C phase diagram, curves a and b representing the critical composition calculated for two different choices of M_ϕ. The T_0 line, where the Gibbs energy of the γ and α phases have the same value for the same composition, has also been included in the diagram. The simulations also reveal that the interface velocity as well as the non-equilibrium partition coefficient k decrease when the alloy composition u_C^{∞} is increased and approaches the critical value. This behavior is in agreement with the velocity dependence on k discussed in [7].

7.2. Solute-drag simulations

Solute-drag simulations were now performed according to the approach outlined in section 3. For a given temperature and composition of the growing α Eq. (14) was solved for a series of interfacial velocities. For each velocity the C concentration profile across the phase interface as well as the C content of γ at the γ-side of the phase interface were obtained and the Gibbs energy dissipation due to diffusion, ΔG_m^{diff}, across the interface was subsequently obtained by integration of the concentration profile and adding the contribution due to interfacial friction, ΔG_m^{i}. From the C content on both sides of the interface the available driving force, ΔG_m^{tot}, was calculated using Eq. (18). At given temperature and composition of the growing α the total dissipated Gibbs energy, $\Delta G_m^{diff} + \Delta G_m^{i}$, and the available driving force may be plotted as functions of interfacial velocity. The general appearance of the two curves is shown in Fig. 5. The total dissipation, solid curve, starts from zero at low velocities, and grows due to dissipation caused by diffusion inside the interface, i.e. solute drag. After a maximum it decreases at high velocities but at very high velocities there is an increase due to the interfacial friction. If the interfacial mobility is low in comparison with the diffusivity inside the interface the dissipation caused by diffusion and friction may overlap and there will be no minimum. The available driving force derives from composition differences across the interface. At low velocities they will yield a negative value

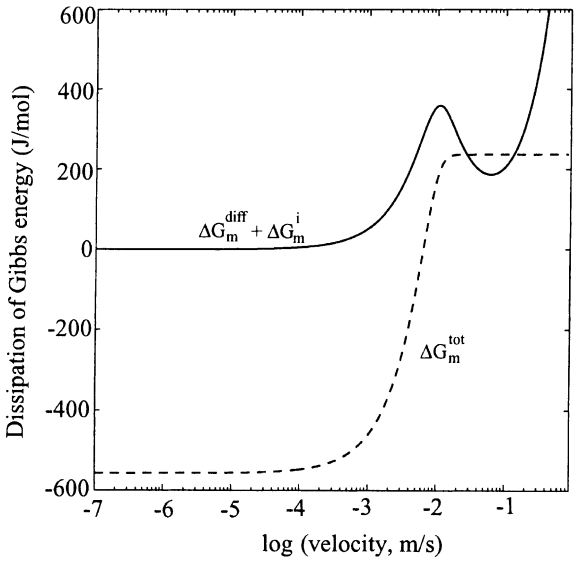

Fig. 5. Dissipated Gibbs energy by diffusion inside the interface as a function of interface velocity obtained by solute-drag theory. The solid line represents the dissipation inside the interface. The dashed line denotes available driving force over the interface.

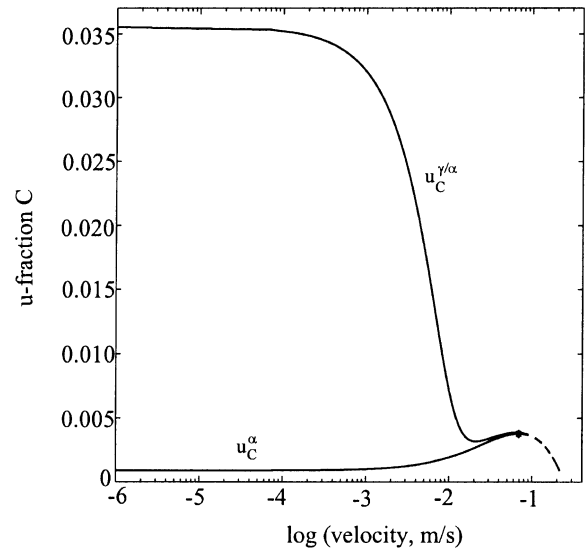

Fig. 6. Carbon contents on the α and γ side of the interface, u_C^{α} and $u_C^{\gamma/\alpha}$, as functions of growth rate corresponding to the intersections in Fig. 5. The dot denotes the highest C content that α could grow with.

if the α phase is chosen inside the equilibrium $\alpha + \gamma$ phase field. It stays constant until the composition on the γ side starts to decrease due to limited diffusion inside the interface. Then it increases and turns positive if it started from a negative value. At very high velocities it will approach the difference in Gibbs energy between α and γ when evaluated for the same C content, $u_C^{\gamma/\alpha} = u_C^{\alpha}$.

Figs. 5 and 6 are based on u_C^{α} values inside the $\alpha + \gamma$ phase field where the driving force starts from a negative value. From Fig. 5 it is evident that the curves must then intersect at an even number of points. We have found that two cases occur. Either the curves intersect at two points, one at a high velocity corresponding to partitionless growth and one at low velocity corresponding to slow growth controlled by C diffusion in γ, or they do not intersect at all. We have not found any cases where there are four but that could very well occur if carbon has a tendency to segregate to the interface. At the intersections the dissipation exactly matches the available driving force. On the left side of the low velocity intersection and on the right side of the high velocity intersection the available driving force is lower than required by the interfacial reactions. In the range between the two intersections the available driving force exceeds what is required for the interfacial reactions and this range thus represents physically possible states. Moreover, if we assume that Gibbs energy is only dissipated by diffusional processes and interfacial friction then the two intersections represent the only combinations of growth rate, u_C^{α} and $u_C^{\gamma/\alpha}$ that are physically possible. As we increase the C content of the growing α the two intersections move towards each other until they finally meet in a point of tangency between the two curves. At higher C contents of α no solution at all is obtained. If u_C^{α} values inside the α one-phase field had been chosen the dashed curve in Fig. 5, denoting the driving force, would have started from a positive value at low velocities. However, since we are primarily interested in the possibility of partionless growth in the two-phase field no such u_C^{α} values were considered. In Fig. 6 we have combined the information on growth rate, u_C^{α} and $u_C^{\gamma/\alpha}$ for the intersections from a large number of calculations. The parts stemming from the high-velocity intersections have been dashed. At low growth rate u_C^{α} and $u_C^{\gamma/\alpha}$ correspond to the

contents given by the phase diagram, i.e. local equilibrium is established, but they approach each other at higher growth rates. The point of tangency between the dissipation and driving force curves in Fig. 5 appears as a maximum on the curve for u_C^α denoted by the dot in Fig. 6 and the two curves have then got very close to each other. This maximum represents the highest C content that α could grow with. With a mobility according to Appendix B, the maximum C content of α fell close to the equilibrium phase boundary for α. However, the maximum C content and the corresponding growth rate depend on the properties of the interface. The higher the interfacial mobility, compared to the diffusivity, the higher the maximum content and the corresponding growth rate. In order to demonstrate clearly the general behavior the calculations presented in Fig. 6 were made using an interfacial mobility ten times larger than the one given in Appendix B. These calculations gave an α well inside the $\alpha + \gamma$ phase field and a growth rate about ten times higher. A calculation with the mobility 100 times larger than the one in Appendix B yields a maximum even closer to the thermodynamic limiting value, i.e. the T_0 line.

7.3. Effect of diffusion in γ and the transition to massive growth

We would now like to study the transition from partitional to partitionless growth and it will be necessary to investigate how γ of a given composition will transform to α. In the phase-field simulations such a transformation occurs when γ has a content below a critical limit, presented by curves a and b for different M_ϕ values, in Fig. 4. In order to investigate the predictions of solute drag theory it is necessary to account for C diffusion in γ ahead of the migrating γ/α interface. It should first of all be realized that the calculations for the interface were made under steady-state growth, which strictly implies that the transformation is partitionless. However, it has already been mentioned that the results could be used as a good approximation for non-steady state conditions, i.e. for partitional transformations.

We now apply Eq. (19) and take u_C^α and $u_C^{\gamma/\alpha}$ as functions of growth rate from Fig. 6, or similar diagrams calculated using different values of the interfacial mobility. For a given alloy we may thus establish a relation between half thickness ℓ and growth rate. The result of a series of such calculations is given in Fig. 7. The alloys having $u_C^{\gamma\infty} = 0.008$ and 0.005, respectively, are represented by the two curves at the bottom left corner of the diagram. When ℓ is close to zero in the very early stages, the assumption of local equilibrium predicts an infinitely high growth rate. From Fig. 6 and Eq. (19) it is obvious that this could never occur because as the growth rate becomes very high $u_C^{\gamma/\alpha}$ will approach u_C^α and the numerator in Eq. (19) becomes very small. It should be emphasized that Eq. (19) is only physically meaningful for $u_C^{\gamma/\alpha} > u_C^{\gamma\infty}$ when α grows with equal or lower C content than γ. In these two alloys ferrite will thus grow under partitioning with a very high but finite rate in the very early stages. For the alloy having $u_C^{\gamma\infty} = 0.003$ there is a similar curve to the left in Fig. 7 but, in addition, there is now a possibility of having a partitionless transformation because $u_C^{\gamma\infty}$ is lower than the maximum C content of α. The partitionless growth could then occur

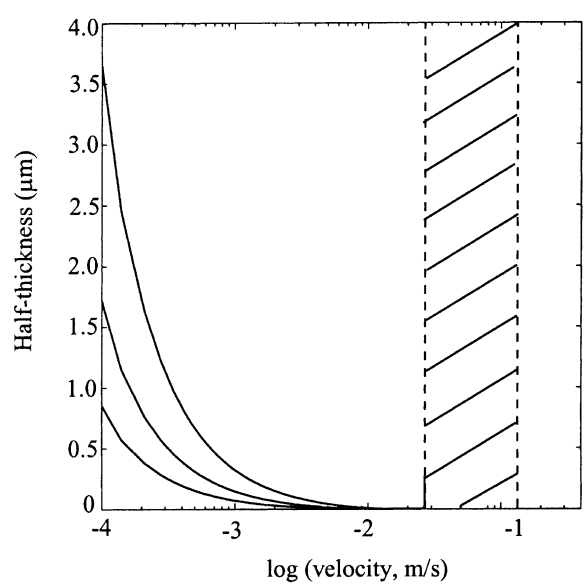

Fig. 7. Relation between half thickness ℓ and growth rate predicted from Eq. (19) and Fig. 6. Each curve holds for a different alloy content as indicated. The hatched area represents velocities where no physical solutions are possible.

with two different growth rates represented by the two sides of the hatched area in Fig. 7. However, as shown by Hillert [1] only the case of the highest growth rate represents a stable situation. The critical C content below which the transformation $\gamma \rightarrow \alpha$ is partitionless thus is the maximum of the u_C^α curve in Fig. 6. That value and corresponding values at other temperatures are plotted as curve c in Fig. 4.

7.4. Comparison between phase-field and solute-drag simulations

The critical C content was calculated as a function of temperature by means of the solute-drag theory and phase-field simulations. With the mobility taken according to Appendix B solute-drag theory predicts a critical composition close to the $\alpha/\alpha + \gamma$ phase boundary, see curve c in Fig. 4. Phase-field simulations using $M_\phi = M/\delta$ gave a critical composition almost in the middle between the T_0 temperature and the phase boundary, see curve a. However, it was argued in section 4 that a more realistic variation of ϕ should be taken into account when evaluating M_ϕ. The relation $M_\phi \cong 0.235\, M/\delta$ was then derived and the corresponding critical compositions are given by curve b. The discrepancy between solutedrag and phase-field simulations is much smaller for this choice of M_ϕ but is still not acceptable. However, even though Eq. (28) was obtained as an exact result it does not necessarily imply that the two approaches must give the same result because the diffusional mobilities and the thermodynamic properties have a different variation across the phase interface in the two approaches. In addition, in the phase-field method all thermodynamic and kinetic properties as well as all their derivatives with respect to distance are continuous over the whole region where ϕ is defined ($-\infty < z < \infty$). The interface is truly diffuse in this case. However, in the solute drag theory these properties vary piecewise linearly over the interface, i.e. already the first derivatives with respect to distance are discontinuous. Thus, both the concentration profile and the quantity ΔG_m^{diff} evaluated from the concentration profile using Eq. (16) will differ and as a consequence the part of driving force available to overcome the interface resistance will differ. In Fig. 8 the concentration profile has been plotted at 1000 K for the velocity 0.0122 $m\ s^{-1}$ and $u_C = 0.00201$. The dashed curve is obtained from the solute-drag calculations and the solid curve from phase field. In this case phase field and solute drag gave a diffusional dissipation of 150 and 232 $J\ mol^{-1}$, respectively. The total driving force, i.e. including the spike ahead of the interface, is 270 $J\ mol^{-1}$ in both cases. That driving force leaves 120 to overcome the interface friction in the phase-field simulation. From $M = 7.2\ 10^{-10}\ m^4 J^{-1} s^{-1}$ at 1000 K and $V_m = 7\ 10^{-6}\ m^3 mol^{-1}$ we obtain by means of Eq. (17) $v = 0.0123\ m\ s^{-1}$ in very good agreement with the phase field result. On the other hand, as can be seen from Fig. 8, this growth rate is not enough to make the transformation partitionless according to the solute-drag simulations and the driving force across the interface, excluding the spike in γ, is 265 $J\ mol^{-1}$ leaving only 33 $J\ mol^{-1}$ to overcome the interface friction. However, even if we neglect that slight decrease in driving force it is obvious that not enough driving force is left to overcome interface friction and we conclude that

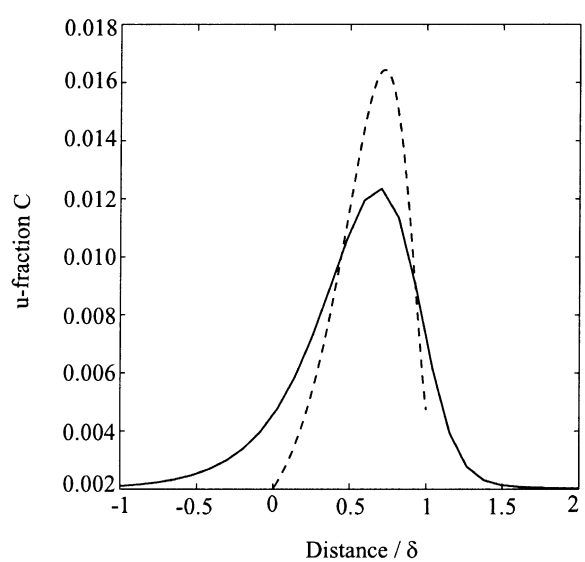

Fig. 8. Phase-field calculation of the concentration profile at $T = 1000$ K, $v = 0.0122\ m\ s^{-1}$, $u_C = 0.00201$ using $M_\phi \cong 0.235 M/\delta$ (solid curve). Solute-drag calculation of the concentration profile at the same temperature and $u_C^\alpha = 0.00201$ (dashed curve). M is given in Appendix B.

according to solute drag theory the alloy $u_C = 0.00201$ cannot grow partitionless at 1000 K.

We may thus conclude that the discrepancy in the predicted critical composition for massive transformation stems from a different variation in thermodynamic properties and mobilities across the interface in the two methods and that the interface is not as diffuse in the solute-drag theory as in the phase-field method. It should be emphasized though, when the interface velocity is so high that all the dissipation of Gibbs energy is due only to interfacial friction the two approaches give exactly the same results, provided that we choose the interfacial mobilities in a consistent way. This is simply because in Eq. (17) no assumptions about the variation of properties across the interface enter.

8. Conclusions

As shown recently by Ahmad et al. isobarothermal phase-field simulations predict a transition to partitionless transformation when the supersaturation is high enough. Here we have considered formation of ferrite from austenite in binary Fe–C alloys and compared a novel method to simulate the solute-drag effect with phase field simulations using an interfacial thickness in the order of atomic dimensions. The methods predict qualitatively the same behavior although the quantitative agreement is less good. However, if the kinetic parameter governing the evolution of the phase field is chosen consistent with the actual variation of the phase-field variable the discrepancy is much reduced. In fact, in the limit of no dissipation by diffusion exact agreement is obtained between the phase-field simulations and conventional modeling based on interfacial friction and an interfacial mobility. The reason that a discrepancy remains when there is diffusional dissipation is that different assumptions are made for the variation of properties across the interface in phase-field and solute-drag modeling, respectively. In the phase field method the variation is expressed as a function of the phase field variable, obtained from the solution of the phase-field equation, whereas in solute-drag modeling a function of distance is postulated. At present the detailed variation is unknown and thus one cannot say that one assumption is better than another. One thus needs to evaluate the variation in properties that best fit the experimental information on the critical temperature. Another possibility is to calculate the variation *ab initio*. Both these approaches will be explored in the near future.

Acknowledgements

The authors would like to thank professor Mats Hillert for valuable advice and stimulating discussions. This work was financed by the Swedish Research Council for Engineering Science and the Swedish Foundation for Strategic Research through the Brinell Centre.

Appendix A. Thermodynamic description of Fe–C system, from Gustafson [8].

$$G_m^\alpha = {}^0G_m^\alpha + \frac{u_C}{3}({}^0G_{FeC}^\alpha - {}^0G_{Fe}^\alpha) + 3RT\left\{\frac{u_C}{3}\ln\left(\frac{u_C}{3}\right) + \left(1-\frac{u_C}{3}\right)\ln\left(1-\frac{u_C}{3}\right)\right\} + \frac{u_C}{3}\left(1-\frac{u_C}{3}\right)L_{Cva}^\alpha + G_m^{mo} \quad \text{(A1)}$$

$$G_m^\gamma = {}^0G_m^\gamma + u_C({}^0G_{FeC}^\gamma - {}^0G_{Fe}^\gamma) + RT\{u_C\ln u_C + (1-u_C)\ln(1-u_C)\} + u_C(1-u_C)L_{Cva}^\gamma \quad \text{(A2)}$$

The quantities introduced in the expressions above are given functions of temperature:

$${}^0G_{Fe}^\alpha = 1224.83 + 124.134T - 23.5143T\ln T - 0.00439752T^2 - 5.89269\cdot 10^{-8}T^2 + 77358.5T^{-1} \quad \text{(A3)}$$

$${}^0G_{FeC}^\alpha - {}^0G_{Fe}^\alpha = 322050 + 75.677T \quad \text{(A4)}$$

$$L_{Cva}^\alpha = -190T \quad \text{(A5)}$$

$$G_m^{mo} = -6507.5\left(\frac{\tau^{-4}}{10} + \frac{\tau^{-14}}{315} + \frac{\tau^{-24}}{1500}\right) \quad \text{(A6a)}$$

if $\tau > 1$

$$G_m^{mo} = -9180.5 + 9.283T - 9309.8\left(\frac{\tau^4}{6} + \frac{\tau^{10}}{135} + \frac{\tau^{16}}{600}\right) \quad \text{(A6b)}$$

if $\tau < 1$

where $\tau = T/T_C$ and $T_c = 1043$ K is the Curie temperature.

$$^0G_{Fe}^{\gamma} = -237.57 + 132.416T - 24.6643T\ln T - 0.00375752T^2 - 5.89269\cdot10^{-8}T^3 + 77358.5T^{-1} \quad \text{(A7)}$$

$$^0G_{FeC}^{\gamma} - {}^0G_{Fe}^{\gamma} = 77207 - 15.877T \quad \text{(A8)}$$

$$L_{Cva}^{\gamma} = -34671 \quad \text{(A10)}$$

$$V_m = 7\ 10^{-6}\ m^3 mol^{-1} \quad \text{(A11)}$$

Appendix B Kinetic parameters for Fe–C

Diffusional mobility in α [11]:

$$RTM_C^{\alpha} = 0.02\cdot10^{-4}\exp\left(-\frac{10115}{T}\right)\exp\left\{0.5898\left[1 + \frac{2}{\pi}\arctan\left(14.985 - \frac{15309}{T}\right)\right]\right\} m^2 s^{-1} \quad \text{(B1)}$$

Diffusional mobility in γ [12]:

$$RTM_C^{\gamma} = 4.529\cdot10^{-7}\exp\left(-\left(\frac{1}{T} - 2.221\cdot10^{-4}\right)(17767 - u_C 26436)\right) m^2 s^{-1} \quad \text{(B2)}$$

Mobility of α/γ interface [19]:

$$M = 0.035\exp\left(-\frac{17700}{T}\right) m^4 J^{-1} s^{-1} \quad \text{(B3)}$$

References

[1] Hillert M. Metall. Mater. Trans. 2002;33A:2299–308.
[2] Hillert M, Sundman B. Acta Met. 1977;25(11).
[3] Ågren J. Acta Met. 1989;37:181.
[4] Liu Z-K, Ågren J. Acta Met. 1989;37:3157.
[5] Loginova I, Amberg G, Ågren J. Acta Mater. 2001;49:573.
[6] Artemev A, Jin Y, Khachaturyan AG. Acta Mater. 2001;49:1165.
[7] Ahmad NA, Wheeler AA, Boettinger WJ, McFadden GB. Phys. Rev. E 1998;58:3436–50.
[8] Gustafson P. Scand. J. Metall. 1985;14:259.
[9] Cahn JW, Allen SM. J. Phys. (Paris) Colloque 1977;C7:C7–C51.
[10] Andersson J-O, Ågren J. J. Appl. Phys. 1992;72:1350.
[11] Ågren J. Acta Met. 1982;30:841.
[12] Ågren J. Scripta Met. 1986;20:1507.
[13] Hillert M. Phase equilibria, phase diagrams and phase transformations—their thermodynamic basis. Cambridge, UK: Cambridge University Press, 1998.
[14] Borgenstam A, Engström A, Höglund L, Ågren J. J. Phase Equilibria 2000;21:269.
[15] Enomoto M. Acta Mater. 1999;47:3533.
[16] Boettinger WJ, Warren JW. Acta Metall. Mater. 1995;43:689.
[17] Gear CW. Numerical initial value problems in ordinary differential equations. Englewood Cliffs, NJ: Prentice-Hall, 1971.
[18] HARWELL Subroutine Library Specification, Computer Science and Systems Division, HARWELL Laboratory, Oxfordshire OX11 0RA, UK.
[19] Hillert M. Metall. Trans. A 1975;6A:5.

Paper 4

P4

On the formation of Widmanstätten ferrite in binary Fe-C - phase-field approach

Irina Loginova[(a)], John Ågren[(b)] and Gustav Amberg[(a)]

[(a)]Department of Mechanics, KTH, S-100 44 Stockholm, Sweden
[(b)]Department of Materials Science and Engineering, KTH, S-100 44 Stockholm, Sweden

Abstract

A phase-field method, based on a Gibbs energy functional, is formulated for $\gamma \to \alpha$ transformation in Fe-C. The derived phase-field model reproduces the following important types of phase transitions: from C diffusion controlled growth through Widmanstätten microstructures to massive growth without partitioning of C. Applying thermodynamic functions assessed by the Calphad technique and diffusional mobilities available in the literature, we study two-dimensional growth of ferrite side plates emanating from an austenite grain boundary. The morphology of the ferrite precipitates is defined by a highly anisotropic interfacial energy. As large values of anisotropy lead to an ill-posed phase-field equation we present a regularization method capable of circumvent non differentiable domains of interfacial energy.

---

1. Introduction

The transformation of austenite to ferrite upon cooling is one of the most studied and well documented subjects in physical metallurgy. Nevertheless, some aspects, which are technologically important as well as of fundamental interest, still remain less well understood and they often lead to controversies. It is generally accepted that at low undercooling more or less equiaxed and rather coarse ferrite particles form along austenite grain boundaries, so-called allotriomorphic ferrite. They grow with a rate controlled by carbon diffusion in austenite. Calculations based on carbon diffusion and local equilibrium at the austenite/ferrite phase interface yield growth rates that essentially agree with the experimentally observed ones. At higher undercoolings ferrite rather grows with a plate-like so-called acicular or Widmanstätten morphology, [**1**]. On the broad sides the austenite/ferrite phase interface is partly coherent and already a long time ago the K-S orientation relationship between austenite and ferrite was reported by Mehl et al. [**2**]. Analytical solutions based on carbon diffusion control and the Ivantsov solution seem capable of representing the experimentally observed growth rates if local equilibrium is assumed and proper account is taken for the effect of interfacial energy at the curved tip. At even higher undercooling the ferrite growth turns partitionless, i.e. there is no redistribution of carbon, and results in a characteristic blocky microstructure, so called massive transformation. The transition to partitionless transformation was recently analyzed by the present authors by means of the phase-field method and solute drag modeling [**4**]

For the transition from allotriomorphic to plate-like growth at least two different opinions have been expressed. Townsend and Kirkaldy [**5**] suggested that plates would develop from grain-boundary allotriomorphs by a morphological instability of a similar type as discussed by Mullins and Sekerka [**6**] during solidification. On the other hand Krahe et al. [**1**] argued that the coherent broad faces could only grow normal to themselves by the migration of growth ledges and when this process occurred by a sufficiently high rate, compared to the diffusion controlled growth of the allotriomorph, then a plate would evolve.

In this paper we shall investigate the morphological instability hypothesis for plate-like growth by means of the phase-field approach which is particularly suitable for modeling pattern formation during phase transformations. It has been very successful when studying the morphological instability during crystallization of a liquid and the subsequent dendritic growth, see for example [**19, 15**]. In this approach the interface between the phases is treated as a region of finite width having gradual variation of the different state variables. An additional variable, the phase-field, is introduced for the sole purpose of avoiding explicit tracking of the position of the evolving phase boundary. The derivation of the phase-field equations is based on thermodynamic principles; the coefficients of the equations are chosen to match the corresponding parameters in the conventional sharp-interface equations through asymptotic analysis.

The phase-field method has also been successfully applied when predicting microstructures during solid-state transformations [**21**] as well as other solid-state processes such as grain growth and coarsening [**20**], facet formation [**7, 13**], multicomponent interdiffusion [**18**] etc.

However, to the authors knowledge, the formation of Widmanstätten ferrite in binary Fe-C has not yet attracted the attention of the phase-field community. As mentioned, Odqvist et al [**4**] derived a phase-field model for $\gamma \to \alpha$ transformation in binary Fe-C. They performed one-dimensional simulations and demonstrated a transition between diffusion controlled and massive growth. A transition from diffusion controlled to a massive transformation is predicted when the temperature falls below the T_0 line and close to $\alpha/\alpha+\gamma$ phase boundary. In the present study we extend their phase-field approach [**4**] from one to two dimensions in order to investigate growth of Widmanstätten plates emanating from an austenite grain boundary. We introduce a highly anisotropic non-differentiable interfacial energy and describe its regularization and numerical treatment.

2. Phase-field model

The phase-field formulation of the isobarothermal $\gamma \to \alpha$ transformation is based on the Gibbs energy functional

$$G = \int_\Omega \left(\frac{G_m(\phi, u_C, T)}{V_m} + \frac{\epsilon^2}{2} |\nabla \phi|^2 \right) d\Omega \tag{1}$$

where G_m denotes the Gibbs energy per mole of substitutional atoms and V_m is the molar volume of substitutional atoms and will be approximated as constant, ϕ is the phase-field variable varying smoothly between 0 in ferrite and 1 in austenite.

The temperature T is assumed to be constant due to the rapid heat conduction. The u-fraction u_C is defined from normal mole fraction of C, x_C as

$$u_C = \frac{x_C}{1 - x_C} \tag{2}$$

The parameter ϵ is related to the interfacial energy σ and the interface thickness δ by means of $\epsilon^2 = 3\sqrt{2}\sigma\delta$ [**4**]. In the case of Widmanstätten plates the coherent broad sides should have quite a low interfacial energy whereas the more or less incoherent tip would have a much higher interfacial energy. The interfacial energy thus is highly anisotropic, i.e. it depends strongly on the orientation of the phase boundary

$$\sigma = \sigma_0 \eta(\theta) \tag{3}$$

where $\theta = \arctan(\phi_y/\phi_x)$ approximates the angle between the interface normal and the x axis. σ_0 is the maximum interfacial energy and is an input parameter. The anisotropy function $0 < \eta(\theta) \leq 1$ will be discussed in the following section. The thickness of the interface also varies with due to anisotropy. In general we expect a coherent interface to be much thinner than an incoherent interface. For the perfectly coherent interface the thickness would vanish. For simplicity we have chosen to represent the anisotropy in interface thickness with the same function, i.e.

$$\delta = \delta_0 \eta(\theta) \tag{4}$$

where δ_0 is the thickness of the incoherent interface and is taken as an input parameter. For the anisotropic case we thus have $\epsilon^2 = 3\sqrt{2}\sigma_0\delta_0\eta(\theta)^2$,

The molar Gibbs energy G_m is postulated as a function of the phase-field variable

$$G_m = (1 - p(\phi))\, G_m^\alpha + p(\phi) G_m^\gamma + g(\phi) W \tag{5}$$

where

$$g(\phi) = \phi^2 (1 - \phi)^2 \tag{6}$$

$$p(\phi) = \phi^3 (10 - 15\phi + 6\phi^2) \tag{7}$$

and the choice of the parameter W was described in [**4**]. Here we have assumed that it is constant and equal to the value of the incoherent interface, i.e. $W = 6\sigma_0 V_m/\sqrt{2}\delta_0$. G_m^α and G_m^γ denote the normal Gibbs energy of the α and γ phases and are taken from the assessment of Gustafson [**8**]. The complete expressions are given in Appendix A. The evolution of the non-conserved phase-field variable is governed by the Cahn-Allen equation [**12**]

$$\dot{\phi} = -M_\phi \frac{\delta G}{\delta \phi} = -M_\phi \left(\frac{1}{V_m} \frac{\partial G_m}{\partial \phi} - \epsilon^2 \nabla^2 \phi + \frac{\partial}{\partial x} \left(\epsilon \epsilon'_\theta \frac{\partial \phi}{\partial y} \right) - \frac{\partial}{\partial y} \left(\epsilon \epsilon'_\theta \frac{\partial \phi}{\partial x} \right) \right) \tag{8}$$

The kinetic parameter M_ϕ is related to the interfacial mobility M as $M_\phi = 0.235M/\delta$ [**4**]. Taking the derivative of G_m with respect to ϕ gives us the phase-field equation

$$\dot{\phi} = M_\phi \left(\epsilon^2 \nabla^2 \phi - \frac{\partial}{\partial x}\left(\epsilon\epsilon'_\theta \frac{\partial \phi}{\partial y}\right) + \frac{\partial}{\partial y}\left(\epsilon\epsilon'_\theta \frac{\partial \phi}{\partial x}\right)\right) + M_\phi \left(p'(\phi)\frac{G_m^\alpha - G_m^\gamma}{V_m} - g'(\phi)\frac{W}{V_m}\right) \tag{9}$$

The evolution of the concentration field is governed by the normal diffusion equation. Assuming approximately constant molar volume and introducing u-fractions the normal diffusion equation can be written as

$$\frac{\dot{u}_C}{V_m} = -\nabla \cdot J_C \tag{10}$$

The diffusional flux of carbon J_C is given by the Onsager linear law of irreversible thermodynamics

$$J_C = -L''\nabla\left(\frac{\delta G}{\delta u_C}\right) \tag{11}$$

If the gradient terms in Eq.(1) are neglected, we find $\delta G/\delta u_C = \partial G_m/\partial u_C$, which is the normal chemical potential μ_C of carbon. Eq.(11) may be expanded in terms of concentration and phase-field gradients

$$J_C = -\frac{1}{V_m} D_C \nabla u_c - L''\nabla \frac{\partial^2 G_m}{\partial u_C \partial \phi}\nabla\phi \tag{12}$$

The first term corresponds to the normal Fick's law and we may thus identify the normal diffusion coefficient of C as

$$D_C = V_m L'' \frac{\partial^2 G_m}{\partial u_C^2} \tag{13}$$

The second-order derivative corresponds to Darken's thermodynamic factor and the parameter L'' is related to the diffusional mobility M_C by means of

$$L'' = \frac{u_C}{V_m} y_{va} M_C \tag{14}$$

where y_{va} denotes the fraction of vacant interstitials, i.e. $1 - u_C$ for γ and $1 - u_C/3$ for α. For a given C content the fraction of vacancies would thus depend on the character of the phase, i.e. it will depend on the phase-field variable. We have postulated that

$$u_C y_{va} = (1 - p(\phi))\, u_C(1 - u_C/3) + p(\phi) u_C(1 - u_C) \tag{15}$$

Taking into account that the diffusional mobility in the two phases could differ by several orders of magnitude, we have chosen the following combination

$$M_C = (M_C^\alpha)^{1-p(\phi)}\,(M_C^\gamma)^{p(\phi)} \tag{16}$$

The mobilities of carbon in α and γ as functions of temperature and u_C are taken from Ågren [**9, 10**] and presented in Appendix B. Finally, substituting Eq.(11)-(16)

into Eq.(10), we obtain the diffusion equation

$$\begin{aligned} \dot{u}_C &= \nabla \cdot \Big[(M_C^\alpha)^{1-p(\phi)} \, (M_C^\gamma)^{p(\phi)} \, [(1-p(\phi))u_C(1-u_C/3) \\ &\quad + p(\phi)u_C(1-u_C)] \, \frac{1}{V_m} \left(\frac{\partial^2 G_m}{\partial u_C^2} \nabla u_C + \frac{\partial^2 G_m}{\partial u_C \partial \phi} \nabla \phi \right) \Big] \end{aligned} \tag{17}$$

3. Anisotropy of the interfacial energy

As mentioned, Widmanstätten growth is characterized by a strong anisotropy in the interfacial properties. Such strong anisotropy of the kinetic coefficient [**13**] and the interfacial energy [**7**] were recently studied in a case of faceted solidification. The facets are formed when the anisotropy function has a narrow minimum or a cusp in a certain direction. In solidification the amorphous liquid is usually isotropic and directions only need to be expressed relative the lattice of the growing crystal. In the case of a solid/solid transformation the situation is more complex because the anisotropy depends on the relative orientation of the crystalline lattices of the two phases as well as the orientation of the phase interface itself. For a two-dimensional case we thus need two parameters to represent the orientation of the interface. The parameter θ has already been introduced as the angle between the interface normal and the x axis. We now consider cases where the orientation relation between ferrite and austenite is such that it is always possible to have a good crystallographic fit along an interfacial plane having the angle θ_0 with the x axis. If a plate with coherent sides develops we expect it to grow with that angle toward the x axis. We have thus used a modified anisotropy function presented in [**7**]

$$\eta(\theta) = \frac{1}{1+\gamma}(1 + \gamma |cos(\theta - \theta_0)|) \tag{18}$$

In the above expression γ defines the amplitude of the anisotropy. It should be emphasized, that with this choice of the anisotropy function, see Eq. 3, the maximum interfacial energy that represents the incoherent part of the interface is simply σ_0, while the variation of γ only affects the minimum interfacial energy representing the coherent part, $\sigma_{min} = \sigma_0/(1+\gamma)$. For the simulations to be presented later we have rather arbitrarily taken $\sigma_0 = 1Jm^{-2}$.

One important aspect of applying strong anisotropy is to check for what values of γ the term $\eta + \eta''$ in the anisotropic extension of the Gibbs-Thomson relation remains positive [**17**]. Given this choice of the anisotropy function, $\eta + \eta'' = 1/(1+\gamma) > 0$ for any non-negative γ. This is true everywhere, except at the cusps $\theta - \theta_0 = n\pi/2$, where the first derivative $\eta'(\theta)$ is discontinuous. A way to circumvent this problem is to smooth the cusps by replacing $\eta(\theta)$ with a smooth function where of $\theta - \theta_0$ is close to $n\pi/2$. The regularized anisotropy function $\eta_r(\theta)$ is defined as follows

$$\eta_r(\theta) = \frac{1}{1+\gamma} \begin{cases} 1 + B + A\sin(\theta - \theta_0), & -\pi/2 \le \theta - \theta_0 \le -\pi/2 + \tilde{\theta} \\ 1 + \gamma\cos(\theta - \theta_0), & -\pi/2 + \tilde{\theta} < \theta - \theta_0 < \pi/2 - \tilde{\theta} \\ 1 + B - A\sin(\theta - \theta_0), & \pi/2 - \tilde{\theta} \le \theta - \theta_0 \le \pi/2 \end{cases} \tag{19}$$

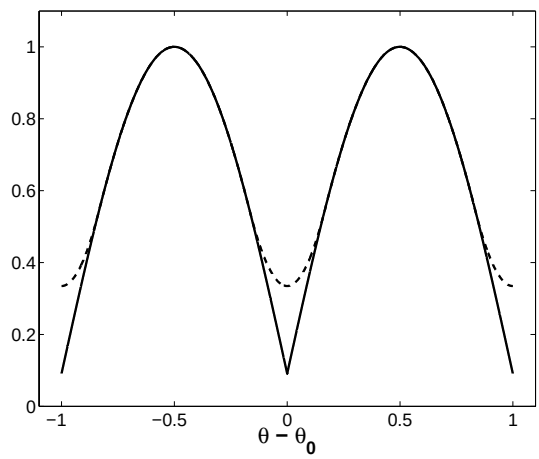

FIGURE 1. The solid plot represents the anisotropy function η calculated with $\gamma = 10$. The dashed line shows the corresponding regularized function η_r. A large angle $\tilde{\theta} = \pi/10$ was used in order to visualize the smoothing of the cusps.

with $A = \gamma \cos(\tilde{\theta})/\sin(\tilde{\theta})$ and $B = \gamma/\sin(\tilde{\theta})$, where $\tilde{\theta} = \pi/200$ is a smoothening angle. The anisotropy function and its regularization is illustrated in Fig.1

4. Numerical issues

For convenience, the governing equations Eq.(9) and (17) are transformed into dimensionless form. Length and time have been scaled with a reference length $l = 0.9\delta_0$ and the diffusion time $l^2/(RTM_C^\alpha)$, respectively. The non-dimensionalized equations are solved by the Finite Element method on adaptive unstructured grids. A first-order semi-implicit time scheme is used for the diffusion equation, while the phase-field equation demonstrates very stiff properties and needs to be solved with fully implicit time-stepping. The resulting system of non-linear equations is solved iteratively by the Newton-Raphson method. The complete Fortran/C/C++ code was generated automatically by the symbolic computational tool femLego [**14**]. The discretized problem was solved in parallel, typically on 8 processors with the dynamic load balancing performed after every grid refinement [**16**].

As it is characteristic for the phase transformations, the variation of u_C and ϕ are highly localized over the phase interface. The width of interface is much smaller than the other length scales in the system, which makes the use of mesh adaptivity beneficial. The mesh distribution follows the evolution of the interface: the phase boundary region has the highest resolution, while the rest of the domain is discretized with large triangles. In the present calculations, the smallest and largest grid resolution was $0.25l$ and $8l$, respectively. The choice of numerical parameters was verified by comparison with the results of 1D calculations [**4**] in the case of diffusion controlled and massive growth.

In the present simulations, the initial state of the system was homogeneous austenite, except for a thin layer of ferrite on the bottom of the domain. The initial composition of C in ferrite was always $u_C^{\alpha\infty} = 0.001$, whereas initial $u_C^{\gamma\infty}$ and

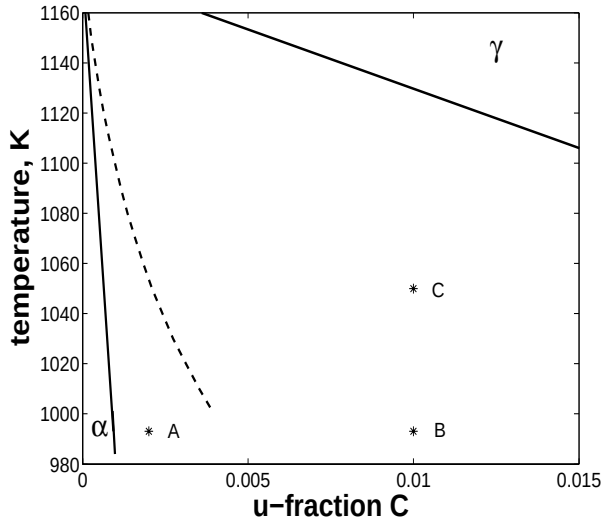

FIGURE 2. Fe-C phase diagram. The superimposed dashed line shows transition to partitionless transformation [**4**]. The points A,B and C specify the operating points for massive transformation, Widmanstätten plates and diffusion controlled growth, respectively.

the temperature differed (see Fig.2). Fig.2) shows the Fe-C phase diagram with imposed operating points for different types of phase transformations, discussed in the following sections. In order to observe growth of the precipitates, the phase boundary was perturbed from a planar shape with a single sinusoidal wave of length $12l$ and amplitude $6l$. Zero-flux boundary conditions were imposed for both variables.

5. Formation of Widmanstätten plates

5.1. Initiation. In all simulations a thin layer of ferrite was initially put along the x axis which we take as the prior austenite grain boundary. First, we study the initiation of a single Widmanstätten plate with $\theta_0 = \pi/2$, i.e. it will grow perpendicularly to the grain boundary. The simulations presented in this section were performed for $T = 993K$ and an alloy content of $u_C^{\gamma\infty} = 0.01$, i.e. 0.22 mass% C (point B in Fig.2). The results from a large number of simulations will now be summarized. First it should be emphasized that the anisotropies which will now be considered, $0 \leq \gamma \leq 100$ are much stronger than usually considered during dendritic solidification where γ is 3 or 4 orders of magnitude lower. The high anisotropy turns out to be the key to understand the initiation of Widmanstätten growth. Our simulations demonstrate that Widmanstätten plates will only develop if the interfacial energy of the coherent sides, i.e. $\sigma_0/(1+\gamma)$, is below a critical value, i.e. the anisotropy amplitude γ should be larger than $\gamma_{critical}$. If $\gamma < \gamma_{critical}$, the initial perturbation decays and we observe a classical diffusion controlled phase transformation with a planar interface, i.e. the grain boundary allotriomorph. It was also found, that the critical value of γ depends on δ_0, which is treated as an input parameter in the present phase-field formulation. We vary δ_0 from 10

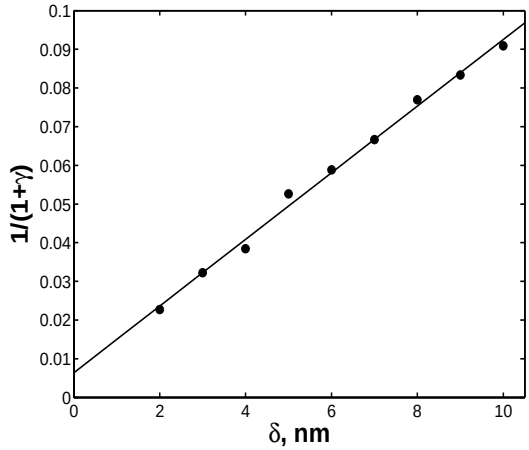

FIGURE 3. The maximal interfacial energy of coherent sides for Widmanstätten growth as function of δ_0. States above the line represent allotriomorphic growth and states below the line Widmanstätten growth.

nm down to 2 nm and for every case we find the smallest value of $\gamma_{critical}$ above which the Widmanstätten morphology is the stable growth mode. Fig.3 shows that $1/(1+\gamma_{critical})$ depends linearly on δ_0. Some discrepancy from the linear behavior of the data can be explained by the fact, that we used only integer values of γ to define $\gamma_{critical}$. The parameter $\gamma_{critical}$ varies from 43 to 10 for $\delta_0 = 2nm$ to $\delta_0 = 10nm$, respectively. A physically realistic value of δ_0 falls in the regime 0.5 - 1.5 nm. The numerical treatment of such very thin interfaces, which implies not only the use of highly dense grids but also solution of very stiff equations (since the properties of the system differ significantly in the two directions) is extremely time-consuming. Consequently, even with the sophisticated computational technique in use and high performance computers it is hardly possible to simulate large-scale problems for realistic interface thicknesses in a reasonable amount of time.

5.2. Characteristics of growth. The growth of a Widmanstätten plate for $\delta_0 = 5$ nm and $\gamma = 20$ is illustrated in Fig.4, where a time sequence of the phase boundary defined as $\phi = 0.5$ is presented. In agreement with experimental observations, e.g. [**22, 23**], the tip of the plate grows with a constant velocity, while the sides grow parabolically. After a short transition period, the plate propagates with a steady-state interface shape which can be divided into three distinct parts: a circular tip, planar sides diverging at a small angle and a bottom part, where the sides are parallel to each other. Except for the tip this shape is rather realistic. In micrographs the observed tip is much sharper than simulated, see Fig.13.

The phase-field and diffusion fields for the final time are presented in Fig.5. One observes the build-up of C in austenite at the sides and the increase of the diffusion length downwards from the tip. The distribution of the fields at the tip, Fig.6, deserves a special consideration. The large variation in the interface width (the width of the transition layer in the phase-field variable) can be explained by the fact that the interface width varies with orientation and is proportional to the

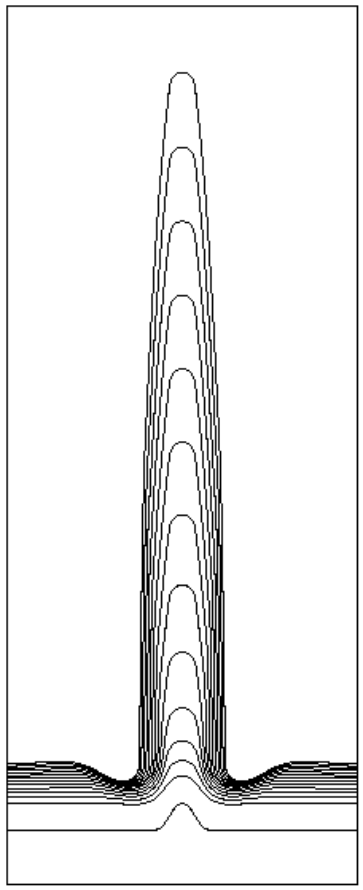

FIGURE 4. Time evolution of a Widmanstätten plate obtained with $\delta_0 = 5nm$ and $\gamma = 20$. The domain size is $0.8\mu m$ x $2\mu m$

anisotropy function $\eta(\theta)$ [**17**]. We can define the tip radius of the plate as the one of the isoline $\phi = 0.5$, however it would give us a value for the tip radius as $3 - 4\delta_0$, see Fig.8, which is smaller than the interface width in the direction of growth. This makes it inadequate to talk about the tip radius as such, but rather consider the tip as being sharp which is consistent with metallographic observations. One may then seriously question the applicability of the Gibbs-Thomson relation to Widmanstätten growth and the whole classical Zener-like theory where the tip radius plays the essential role. In the classical approach the Ivantsov solution yields the growth rate of the tip as inversely proportional to the tip radius rather than a unique rate and tip radius. When account is taken for the effect of interfacial energy by means of the Gibbs-Thomson relation one finds a critical radius below which the tip cannot grow and a radius at which the tip grows with a maximum rate. Usually one then assumes that the tip would grow with this maximum rate and the corresponding tip radius, the Zener maximum growth-rate hypothesis.

In our phase field calculation there is no need for such a hypothesis. As soon as the interface thickness δ_0 and the anisotropy are known the growth rate may be determined by the simulations. In Fig.7 the tip velocity is given as a function of

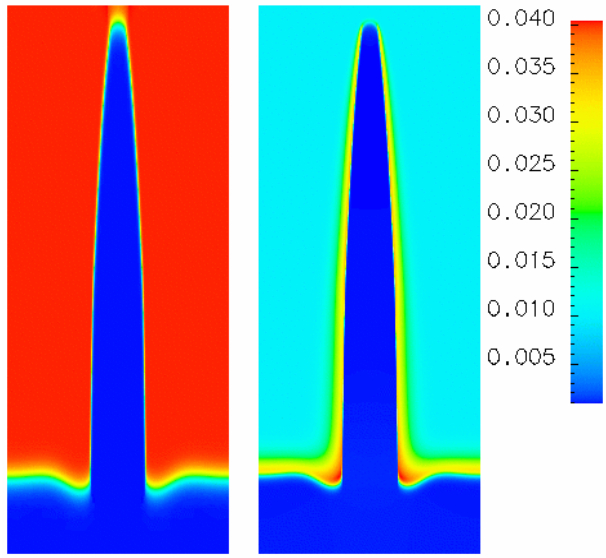

FIGURE 5. Distributions of the phase-field to the left and concentration to the right. The concentration field is supplied with the colormap, while for the phase-field blue color denotes ferrite and red color - austenite. The distributions correspond to the time evolution in Fig.4.

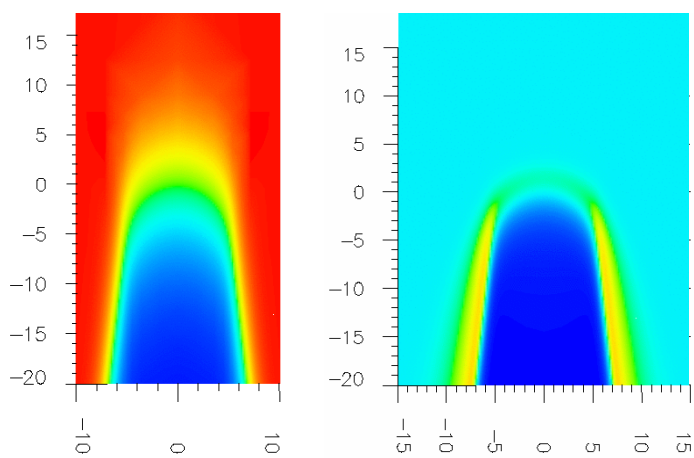

FIGURE 6. Distributions of the phase-field (left) and concentration (right) at the plate's top. The axis are given in δ_0. The colormaps are identical to ones in Fig.5

anisotropy for $\delta_0 = 5nm$, which is too large a value to be really realistic. Anyhow, we can read, for example, that the anisotropy of 0.05 would yield a growth rate around $0.4 \cdot 10^{-3} ms^{-1}$ and from Fig.8 that the tip radius would be $5\delta_0$. This growth rate should be compared with the experimentally reported [**22**] for a similar C content but a lower temperature, i.e. 973 K, which is $0.2 \cdot 10^{-3} ms^{-1}$. On the other hand, it is evident from Fig.3 that for a realistic interface thickness of $\delta_0 = 1nm$ we should have $\sigma_0/(1+\gamma) < 0.015$ in order to observe Widmanstätten growth.

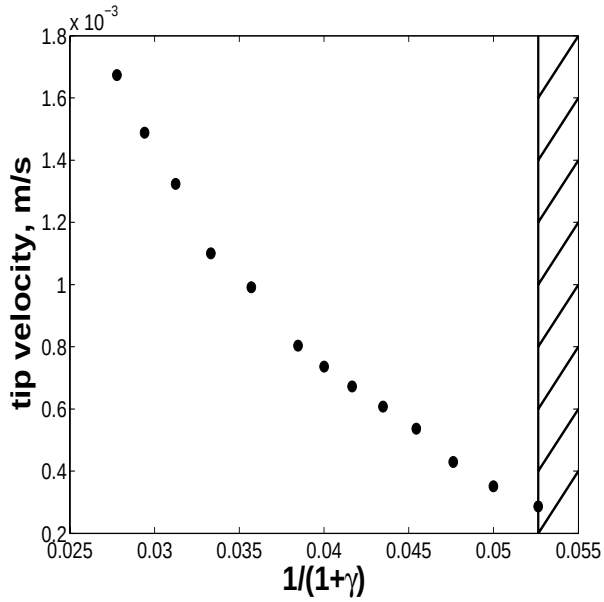

FIGURE 7. The tip velocity as a function of the interfacial energy obtained for $\delta_0 = 5nm$, $T = 993K$ and $u_C^{\gamma\infty} = 0.01$.

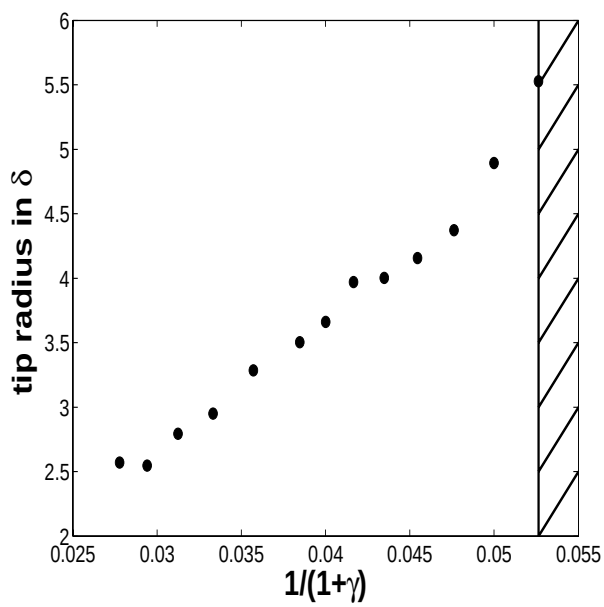

FIGURE 8. The tip radius as a function of the interfacial energy obtained for $\delta_0 = 5nm$, $T = 993K$ and initial $u_C^{\gamma\infty} = 0.01$.

Such high anisotropy would yield a growth rate one order of magnitude large than observed, see Fig.7.

We investigated the dependency of the tip velocity on the interface thickness and the interfacial energy of coherent sides. First, we fixed δ_0 as 5 nm and varied $1/(1+\gamma)$. We found that the tip velocity decays with increase of $1/(1+\gamma)$, Fig.7,

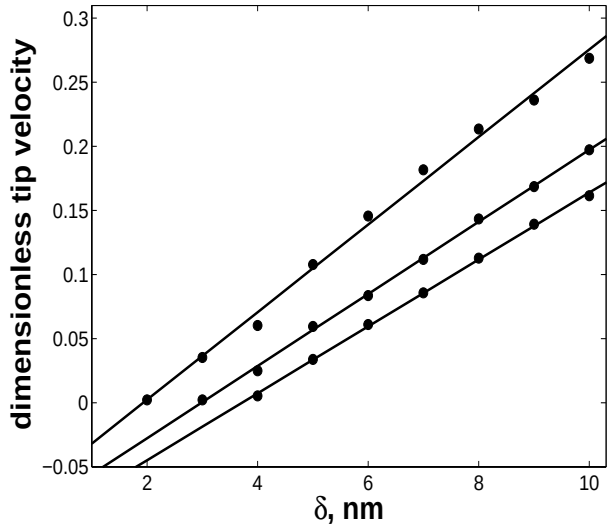

FIGURE 9. Variations of dimensionless tip velocity Vl/RTM_C^α with the interface thickness δ_0. The top, middle and bottom lines are obtained from the simulations with $1/(1+\gamma)$ equal to 0.021, 0.032 and 0.38, respectively. These are the critical values for the growth of Widmanstätten plates for δ_0 equal to 2, 3 and 4 nm, respectively

while the tip radius (defined for the isoline $\phi = 0.5$) increases, Fig.8. Second, we fixed three values of $1/(1+\gamma)$ allowing δ_0 to vary. The dimensionless velocity Vl/RTM_c^α shown in Fig.9 reduces as δ_0 approaches realistic physical values and increases with the decrease of the interfacial energy. For all the cases of $1/(1+\gamma)$, the dependence is linear. It is interesting to observe that extrapolation of the data to smaller values of δ_0 gives a negative velocity if the value of $1/(1+\gamma)$ is greater than $1/(1+\gamma_{critical})$ for those δ_0. This indicates that as realistic values for δ_0 are considered, i.e. in the order of 1 nm or less, then Widmanstätten plates can only grow if the anisotropy is large enough, i.e. $\gamma \cong 100$.

5.3. Growth of colonies. Additionally, we simulated the growth of a colony of Widmanstätten plates emanating from an austenite grain boundary. In order to initiate the growth of the precipitates, the phase boundary was initially disturbed by a combination of sinusoidal waves. The time sequence of the growth is presented in Fig.10. The precipitates are tilted with respect to the grain boundary by $\theta_0 = \pi/3$. One notice, that perturbations having larger wavelength start growing faster, while those of small wavelength may decay or grow significantly behind the others.

As a comparison, Fig.13 shows Widmanstätten ferrite plates that have developed from prior austenite grain boundaries in a low-alloy steel, white areas. The austenite matrix has subsequently transformed to pearlite upon cooling. One observes that though the simulated plates look very realistically, their sides are too smooth compared to the experimental plates. This is probably due to purely deterministic nature of the model. One can expect that modeling heat fluctuations in the system in a similar way it was done for dendritic growth [**24**] would reproduce even better the experimentally observed Widmanstätten morphologies.

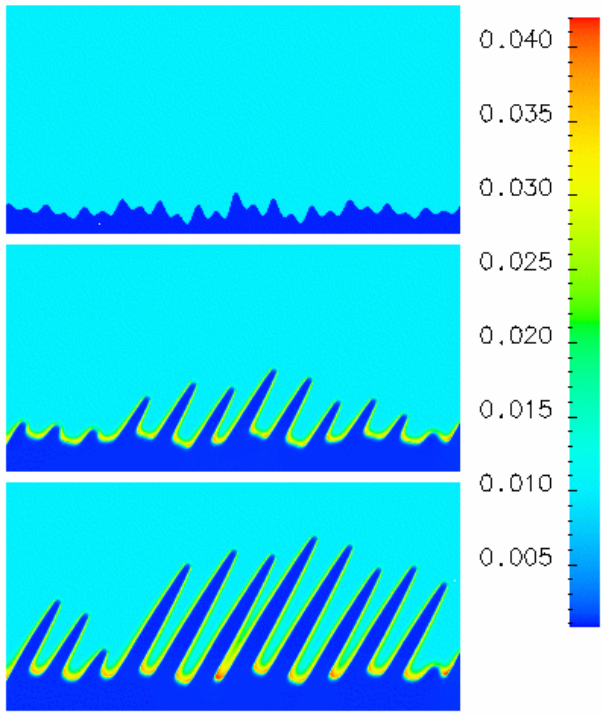

FIGURE 10. Colony of Widmanstätten plates. Concentration distribution calculated for $\delta_0 = 10nm$, $\gamma = 10$ in a box $2\mu m$ x $1\mu m$)

6. Transition between diffusion controlled and massive transformation

As it was shown in [**4**], depending on the initial content of C in austenite, the $\gamma \to \alpha$ phase transformation can be either diffusion controlled or massive. The latter occurs if the initial $u_C^{\gamma\infty}$ falls close to the $\alpha/\alpha + \gamma$ phase boundary. The massive transformation is partitionless, i.e. it does not involve any change of composition, thus a long-range diffusion is unnecessary. The time sequence of the concentration distribution presented in Fig.11 was obtained for $T = 993K$ and $u_C^{\gamma\infty} = 0.002$ (point A in Fig.2). As one observes, the initial perturbation of the interface does not develop into a Widmanstätten plate, but rather decays so that the interface becomes flat. The massive growth occurs with a constant growth rate until all of austenite is transformed into ferrite. The concentration profile in the vertical direction comprises a traveling spike which is spread over a distance of $5\delta_0$.

A completely different behavior is found for an alloy with $u_C^{\gamma\infty} = 0.01$ and $T = 1050K$ (point C in Fig.2). The concentration fields given in Fig.12 again demonstrate the disappearance of the initial disturbance. However, in this case, the excess carbon is build-up ahead of the interface and we observe diffusion-controlled growth. The interface velocity is essentially proportional to $1/\sqrt{(t)}$ except for the later stages when impingement sets in and the system finally approaches the state of equilibrium.

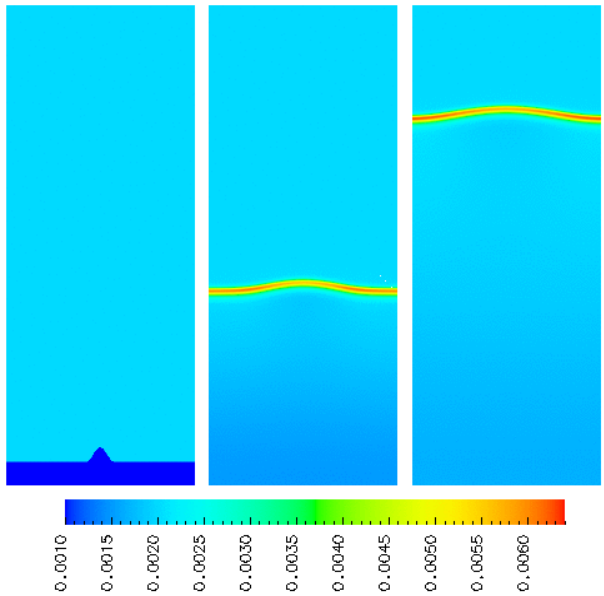

FIGURE 11. Partitionless growth. Concentration field obtained for $\delta_0 = 2nm$, $\gamma = 50$ in a box 0.32 x $0.8\mu m$. Initial conditions are $T = 993K$ and $u_C^{\gamma\infty} = 0.002$

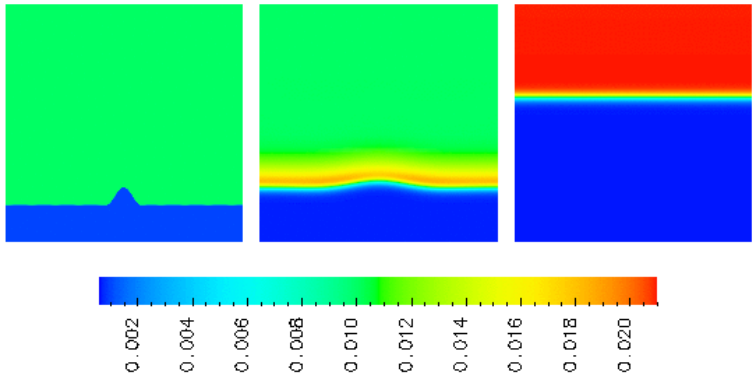

FIGURE 12. Diffusion controlled growth. Concentration field obtained for $\delta_0 = 5nm$, $\gamma = 19$ in a box 0.32 x $0.32\mu m$. Initial conditions are $T = 1050K$ and $u_C^{\gamma\infty} = 0.01$

7. Conclusions

Our simulations reveal that the anisotropy in the surface energy and interface thickness plays the key role in determining whether Widmanstätten growth is possible or not. For the supersaturation, i.e. temperature and C content, considered here a realistic thickness of the incoherent interface, i.e. somewhat lower than 1 nm, shows that γ must be greater than 100 in order for Widmanstätten plates to grow. It seems likely that higher supersaturation would require lower γ for Widmanstätten growth. This is the subject of further research. If Widmanstätten growth occurs, larger values of γ give sharper tips and higher tip velocities. A

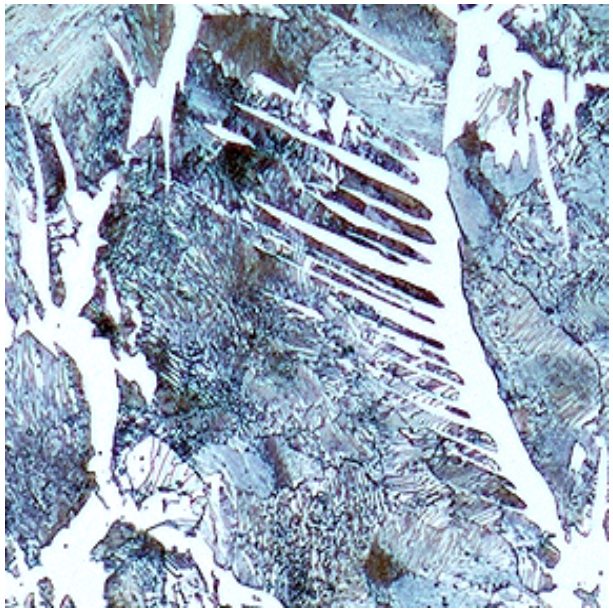

FIGURE 13. Experimentally observed Widmanstätten ferrite plates that have developed from prior austenite grain boundaries in a low-alloy steel, white areas.

lower anisotropy value would make the tip more blunt and yield a lower tip velocity. The tip radius, upon which the classical Ivantsov-based theory is built, vary approximately as proportional to anisotropy and for $\gamma \cong 100$ it is less than 1 nm, i.e. it is of atomic dimensions.

Our simulations thus indicate that the shape of a plate may be described as two parallel sides growing out from the allotriomorph to some distance and then two planar sides that meet in an atomistically sharp tip. Such a shape seems to be in better agreement with metallographic observations than the parabolic shape with its well defined tip radius predicted by the Ivantsov solution.

We also conclude that the present two-dimensional model predicts a transition to a massive transformation, in agreement with our previous study, if the supersaturation is large enough. We find it very encouraging that a single phase-field formulation is capable of predicting three different growth morphologies of ferrite, the allotriomorphic, Widmanstätten and massive growth.

Acknowledgments

This work was supported by the Swedish Research Council (VR).

Appendix A. Thermodynamic description of Fe-C system [8]

$$\begin{aligned} G_m^\alpha &= {}^0G_{Fe}^\alpha + \tfrac{u_C}{3}\left({}^0G_{FeC}^\alpha - {}^0G_{Fe}^\alpha\right) \\ &+ 3RT\left\{\tfrac{u_C}{3}\ln\left(\tfrac{u_C}{3}\right) + \left(\tfrac{1-u_C}{3}\right)\ln\left(1-\tfrac{u_C}{3}\right)\right\} \\ &+ \tfrac{u_C}{3}\left(1-\tfrac{u_C}{3}\right)L_{Cva}^\alpha + G_m^{mo} \end{aligned} \tag{20}$$

$$\begin{aligned} G_m^\gamma &= {}^0G_{Fe}^\gamma + u_C\left({}^0G_{FeC}^\gamma - {}^0G_{Fe}^\gamma\right) \\ &+ RT\left\{u_C \ln\left(u_C\right) + \left(1-u_C\right)\ln\left(1-u_C\right)\right\} \\ &+ u_C\left(1-u_C\right)L_{Cva}^\gamma \end{aligned} \tag{21}$$

The quantities introduced in the expressions above are given functions of the temperature

$$\begin{aligned} {}^0G_{Fe}^\alpha &= 1224.83 + 124.134T - 23.5143T\ln T - 0.00439752T^2 \\ &- 5.89269\cdot 10^{-8}T^3 + 77358.5T^{-1} \end{aligned} \tag{22}$$

$${}^0G_{FeC}^\alpha - {}^0G_{Fe}^\alpha = 322050 + 75.667T \tag{23}$$

$$L_{Cva}^\alpha = -190T \tag{24}$$

$$G_m^{mo} = -6507.7\left(\frac{\tau^{-4}}{10} + \frac{\tau^{-14}}{315} + \frac{\tau^{-24}}{1500}\right),\ \text{if } \tau > 1 \tag{25}$$

$$G_m^{mo} = -9180.5 + 9.723T - 9309.8\left(\frac{\tau^{4}}{6} + \frac{\tau^{10}}{135} + \frac{\tau^{16}}{600}\right),\ \text{if } \tau < 1 \tag{26}$$

where $\tau = T/T_C$ and T_C=1043 K is the Curie temperature.

$$\begin{aligned} {}^0G_{Fe}^\gamma &= -237.57 + 132.416T - 24.6643T\ln T - 0.00375752T^2 \\ &- 5.89269\cdot 10^{-8}T^3 + 77358.5T^{-1} \end{aligned} \tag{27}$$

$${}^0G_{FeC}^\gamma - {}^0G_{Fe}^\gamma = 77207.0 - 15.877T \tag{28}$$

$$L_{Cva}^\gamma = -34671 \tag{29}$$

Appendix B. Kinetic parameters for Fe-C

Diffusional mobility in α [**9**]

$$RTM_C^\alpha = 2\cdot 10^{-6}e^{-10115/T}\exp\left\{0.5898\left[1 + \frac{2}{\pi}\arctan\left(14.985 - \frac{15309}{T}\right)\right]\right\} m^2/s \tag{30}$$

Diffusional mobility in γ [**10**]

$$RTM_C^\gamma = 4.529\cdot 10^{-7}\exp\left(-\left(\frac{1}{T} - 2.221\cdot 10^{-4}\right)\left(17767 - u_C 26436\right)\right) m^2/s \tag{31}$$

Mobility of α/γ interface [**11**]

$$M = 0.035exp(-17700/T)\ m^4/J/s \tag{32}$$

References

[1] P.R. Krahe, K.R. Kinsman and H.I. Aaronson, *Acta Metallurgica*, 20, 1109-1121, 1972

[2] R.F. Mehl, C.S. Barret and D.W. Smith, *Trans. AIME*, 105, 215, 1935

[3] H.I.Aaronson, G.Spanos, R.A.Masamura, R.G.Vardiman, D.W.Moon, E.S.K. Menon and M.G.Hall, *Materials science and engineering B*, B32, 107-123, 1995

[4] I.Loginova, J. Odqvist, G.Amberg and J.Ågren, *Acta Materialia*, 51, 1327-1339, 2003

[5] R.D. Townsend and J.S. Kirkaldy, *ASM Trans. Quart.*, 61, 605-619, 1968

[6] W.W. Mullins and R.F. Sekerka, *J. Appl. Phys.*, 35, 444-451, 1964

[7] J. M. Debierre, A. Karma, F. Celestini, and R. Guerin,cond-mat/0302368

[8] P. Gustafson, *Scand. J. Metall*, 14, 259, 1985

[9] J. Ågren, *J. Acta Materialia*, 30, 841, 1982

[10] J. Ågren, *J. Scripta Met.*, 20, 1507, 1986

[11] M. Hillert, *M. Metall. Trans. A*, 6A, 5, 1975

[12] J.W.Cahn and S.M.Allen *J. Phys. (Paris) Colloque*, C7:C7-C51,1977

[13] T.Uehara and R.Sekerka *M. Metall. Trans. A*, 254,251-261,2003

[14] G.Amberg, http://www.mech.kth.se/ gustava/femLego

[15] I.Loginova, G.Amberg and J.Ågren, *Acta Materialia*, 49, 573-581, 2001

[16] , M.Do-Quan, I.Loginova and G.Amberg,"Application of parallel adaptivity to simulation of materials processes", unpublished

[17] G.B.McFadden, A.A.Wheeler,R.J.Braun,S.R.Coriell and R.Sekerka *Phyc. Rev. E*, 48,2016-2024,1993

[18] K.Wu,J.E.Morral and Y.Wang, *Acta Mater.*, 49, 3401-3408, 20

[19] A.Karma and W.J.Rappel, *Phys. Rev. E*, 53, 4323-4349, 1998

[20] R.Kobayahsi, J.A.Warren and W.C.Carter, *Physica D* , 150, 141-150, 2000

[21] A.Artemev, Y.Jin and A.G.Khachaturyan *Acta Mater.*, 49, 1165, 2001

[22] M. Enomoto, Mteall. and Mat. Trans. A, 25A, 1947-1955, 1994

[23] M. Hillert, Mteall. and Mat. Trans. A, 25A, 1957-1966, 1994

[24] A.Karma and W.J.Rappel,*Physical review E*, 60, 1999, 3614-3625

Paper 5

P5

Morphology diagram of thermal dendritic solidification by means of phase-field models in 2 and 3 dimensions

I.Loginova[a], H. M. Singer[b], J.H. Bilgram[b] and G.Amberg[a]

[(a)] Department of Mechanics, KTH, S-100 44 Stockholm, Sweden
[(b)]Laboratory for Solid State Physics, Swiss Federal Institute of Technology ETH, CH-8093 Zurich, Switzerland

Abstract

We have determined morphology diagrams in 2 and 3 dimensions for two different phase field models (Wheeler [**22**] and Karma [**20, 21**]) for the parameters undercooling and anisotropy of surface tension. The comparison with analytical predictions show a qualitative correspondence, however the predicted shape of the morphology boundary differs significantly from the shape found in our simulations. The two investigated models show the same quantitative behavior. Our simulations in 3D have shown that the shape of the morphology boundary is qualitatively similar to the one in 2D. However we find that the border is shifted by an amount of 0.32 on the anisotropy axis. Our simulated 3D structures show a qualitative correspondence to the ones we have found in *in situ* experiments with xenon.

1. Introduction

Pattern formation is a universal process in nature and technology. The understanding of the underlying physical processes of these self organizing systems is of vital interest in material science as well as theoretical physics. The growth of a single component crystal into its undercooled melt shows a wide variety of different structures. The best known morphology is the dendritic one, which is considered to be a prototype for a whole class of phenomena like snow crystals or cast metals as it evolves complex spatio-temporal structures far from equilibrium from initially homogeneous starting conditions. The governing equations for this system are known as the Stefan-problem [**1**] or sharp interface model:

$$\frac{\partial u}{\partial t} = D\nabla^2 u \tag{1}$$

$$v_n = D(\nabla u|_{solid} - \nabla u|_{liquid}) \cdot \hat{n} \tag{2}$$

$$u|_{interface} = \Delta - \beta v_n - d_0\kappa \tag{3}$$

where u denotes the dimensionless temperature field $u = (T - T_\infty)/(c_p/L)$, with T_∞ the far field temperature, the dimensionless undercooling $\Delta = (T_m - T_\infty)/(c_p/L) = \Delta T L/c_p$, where ΔT, c_p, L are undercooling, specific heat of the liquid, latent heat and T_m the equilibrium melting temperature respectively. Equation 1 corresponds to the classical diffusion equation. The domain is usually taken to be infinite so that no finite size boundary effects affect the growth of the crystal. The temperature of

the melt is assumed to be homogeneous $T_\infty < T_m$ at the beginning of the experiment and thermal diffusivity is the same in the crystal and in the melt ($D = D_s = D_l$). In order to initiate the growth of the crystal, a small seed at melting temperature is placed in the center of the domain.

The conservation of energy is taken into account by the continuity equation (eq.(2)). Eq.(3) is the well known Gibbs-Thomson relation which describes the temperature at the interface for the non-isothermal case. The interface temperature is dependent on the velocity of advancement (kinetic effect) and the local curvature. The parameters d_0 and β are the anisotropic capillary length and the anisotropic kinetic coefficient respectively. For small undercoolings $\Delta \ll 1$ the kinetic term is usually neglected. Usually fcc-structures are modeled, therefore a fourfold anisotropy is used.

The dendritic morphology is the most studied morphology. The first attempts to describe the dendrite tip analytically are due to Papapetrou [**3**] and Ivantsov [**2**]. In the absence of capillary and kinetic effects Ivantsov showed analytically [**2**] that a rotational paraboloid is a steady state solution of eqs.(1)-(3) in 2 and 3 dimensions. General reviews about dendritic solidification were given by Langer in [**4, 5**].

Brener et al. [**6, 7, 8**] tried in their mathematical studies for two dimensional single component systems to develop a description of a large class of patterns found in diffusional growth. They have constructed a morphology diagram and predicted possible transitions between the morphologies. The two shape controlling parameters are the undercooling (which controls the growth velocity) and the anisotropy (leading to non-axisymmetric growth). Although only qualitatively, Brener et al. established stability regions of dendrites and seaweed structures in 2 dimensions. They suggested the distinction of growth morphologies [**6**] by two different criteria: on one hand they distinguish between dendritic and seaweed (non-dendritic) structures. The second criterion is the distinction between compact and fractal growth. They consider dendrites as patterns with orientational order whereas seaweed structures are patterns without obvious orientational order. They define compact growth as growth with constant (albeit arbitrary) average density. Fractal structures are defined as patterns with self-similar or self-affine internal structure with a scaling range of at least one order of magnitude in length scales and non-constant average density. Their morphology diagram is given in figure 2. For $\Delta > 1$ the growth is governed by kinetics. The morphology discrimination takes place in the diffusion limited domain $\Delta < 1$. For high undercoolings and moderately low anisotropies compact and fractal seaweed is found. For moderately low undercooling and high anisotropies compact and fractal dendrites are to be found. It has been stated that doublon structures in 2D are the building blocks for seaweed growth [**7**].

In numerical studies with a phase-field model Kupferman et al. [**9**] and Ben-Amar et. al. [**10**] have established already a morphology diagram for 2 dimensions at high undercoolings ($\Delta = 0.6 - 0.9$) and anisotropies $\gamma = 0.0 - 0.4$. However they have used the model of Kobayashi [**11**] which was not shown to be quantitative, as far as we know. Furthermore their main emphasis was on the evolution of the envelope shape and not mainly on the classification of the different morphologies.

Experimentally both morphology types are found in 2 and 3 dimension. Dendrites in 2D were already analyzed by Papapetrou [**3**]. Glicksman et al. [**13**] were the first to grow dendrites in 3D. In quasi planar growth seaweed and doublon structures were found by Akamatsu and Faivre [**12**] in solutal growth with SCN and acetone. Only very recently Stalder and Bilgram [**14**] reported on the existence of doublons and seaweed in 3 dimensions. They were characterized by Singer [**15**].

2. Model

In order to refine the mathematical (asymptotic) predictions of Brener et al. and to establish a quantitative morphology diagram of the single component model system it is necessary to solve eqs.(1)-(3) numerically. The direct solution of the sharp interface model is rather tedious as it is a moving boundary problem. The phase boundary has to be tracked at every time step leading to an evolving polygon trait. Only very few research groups have attempted this direct approach [**16, 17, 18**]. Another, more motivating approach is to introduce a second variable, the phase field ϕ, which keeps track of the physical phase state at every point of the system. The crucial mathematical parameter here is the interface thickness, which determines how close to the Heaviside approach of the classical model the phase field approach is. The most important advantage of this method is, that the interface does not have to be tracked at all, as the phase variable is defined for the whole domain of interest. The interface is found by identifying regions of steep phase field changes. This commodity comes however at the expense of solving two coupled differential equations. From the algorithmic point of view the phase field method is much more elegant as it shifts the problem to simply solving partial differential equations. It is important to note that this method is only a substitute for solving eqs.(1)-(3) directly when they are recovered asymptotically for vanishing interface thickness [**23**]. A rigorous investigation on asymptotics was performed by Karma and Rappel [**20, 21**].

In this paper we present numerical simulations for two models of the phase field approach which will be referred as the Wheeler-model and the Karma-model. We have chosen both models in order to investigate the difference in the results (if there are any) and to provide a more stable physical base for the quantitative prediction of experimental morphologies.

The first numerical simulations of the Wheeler-model were presented in [**22**]. Shortly afterwards the proof of its thermodynamical consistency was given by Wang et al. [**23**]. The non-dimensional governing equations can be formulated as:

$$\frac{\varepsilon^2}{m}\frac{\partial \phi}{\partial t} = \phi(1-\phi)\left(\phi - \frac{1}{2} + 30\varepsilon\alpha\Delta u\phi(1-\phi)\right) + \varepsilon^2\nabla_a^2\phi \tag{4}$$

$$\frac{\partial u}{\partial t} = -\frac{1}{\Delta}\frac{\partial}{\partial t}\left[\phi^3(10-15\phi+6\phi^2)\right] + \nabla^2 u \tag{5}$$

The temperature field is non-dimensional with the melting temperature $u_m = 0$ and the initial temperature distribution $u = -1$. The phase variable ϕ is defined from $\phi = 0$ solid to $\phi = 1$ liquid. Δ is the non-dimensional undercooling. The

parameters m and α are defined as

$$\alpha = \frac{\sqrt{2}w_0 L^2}{12c\sigma T_m} \tag{6}$$

$$m = \frac{\mu\sigma T_m}{DL} \tag{7}$$

with w_0 a chosen characteristic length scale, L the latent heat, c_p the specific heat, $\mu = c_p/(L\beta)$ the interfacial mobility, σ the interfacial free energy and D the thermal diffusivity. With the interface thickness δ the phase field model leaves one degree of freedom $\varepsilon = \delta/w_0$ which is used to set the interface thickness. The interfacial mobility $\mu = \mu(\mathbf{n})$ is anisotropic, however we have decided that we will choose an isotropic (average) value $\mu = \mu_0$ for the simulations of both models. The Laplacian in eq.(4) was modified in order to take into account the preferred growth directions of the material. For the limit $\lim_{\varepsilon\to 0}$ it can be shown that eq.(5) reduces to the diffusion equation $\partial u/\partial t = \nabla^2 u$. An early asymptotic analysis showed that the moving boundary conditions eqs.(2) and (3) can be recovered with $O(\varepsilon)$, which is sufficiently fast for a convergence [**19**]. Karma and Rappel have shown in their model that even a second order accuracy can be obtained [**21**]. This faster convergence is in particular useful since it allows to simulate the growth with coarser grids or larger grids without loosing accuracy.

The first three-dimensional simulations were performed by Kobayashi [**24**]. Also by means of phase field simulation Abel et. al. [**25**] showed that stable triplons in 3 dimensions exist for channel growth. Plapp and Karma [**26**] used a random walker algorithm to solve the phase field equations and simulate dendrites at very low undercoolings.

In 2 dimensions the anisotropy with respect to growing angle is usually modeled as

$$\eta(\theta) = 1 + \gamma\cos 4\theta,\ \theta = \arctan\left(\frac{\partial\phi}{\partial y}/\frac{\partial\phi}{\partial x}\right), \tag{8}$$

where γ denotes the strength of the anisotropy. Anisotropic variables, e.g. the surface energy can the be expressed as the product of a constant parameter and $\eta(\theta)$. The anisotropic 2D Laplacian in eq.(4) can be written as

$$\nabla_a^2\phi = -\frac{\partial}{\partial x}\left(\eta\eta'\frac{\partial\phi}{\partial y}\right) + \frac{\partial}{\partial y}\left(\eta\eta'\frac{\partial\phi}{\partial x}\right) + \nabla\cdot\left(\eta^2\nabla\phi\right), \tag{9}$$

where $'$ denotes the differentiation with respect to θ.

In 3 dimensions the anisotropy can be expressed as

$$\eta(\mathbf{n}) = (1-3\gamma)\left(1 + \frac{4\gamma}{1-3\gamma}\frac{n_x^4 + n_y^4 + n_z^4}{|n|^4}\right), \tag{10}$$

where $\mathbf{n} = \nabla\phi/|\nabla\phi|$ is the normal vector of the interface (in 2D and 3D). Then the anisotropic 3D Laplacian is given by

$$\nabla_a^2\phi = \frac{\partial}{\partial x}\left(|\nabla\phi|^2\eta\frac{\partial\eta}{\partial\phi_x}\right) + \frac{\partial}{\partial y}\left(|\nabla\phi|^2\eta\frac{\partial\eta}{\partial\phi_y}\right) + \frac{\partial}{\partial z}\left(|\nabla\phi|^2\eta\frac{\partial\eta}{\partial\phi_z}\right) + \nabla\left(\eta^2\nabla\phi\right) \tag{11}$$

The governing equations in the Karma model are expressed by:

$$\begin{aligned} \tau(\mathbf{n})\frac{\partial \phi}{\partial t} &= [\phi - \lambda u(1-\phi^2)](1-\phi^2) + w_0^2 \nabla_a^2 \phi \\ \frac{\partial u}{\partial t} &= D\nabla^2 u + \frac{1}{2}\frac{\partial \phi}{\partial t} \end{aligned} \tag{12}$$

In this model, the non-dimensional melting temperature is set to be zero, while the far-field temperature is equal to $-\Delta$. The phase-field variable is -1 in liquid and 1 in solid.

The anisotropic parameter $\tau(\mathbf{n}) = \tau_0 \eta(\mathbf{n})$ is chosen in such a way that the kinetic term can be canceled. The parameter λ and the capillary length d_0 are connected in the following way:

$$d_0 = a_1 \frac{w_0}{\lambda}, \tag{13}$$

where $a_1 = 5\sqrt{2}/8$ is a numerical constant and $w(\mathbf{n}) = w_0 \eta(\mathbf{n})$. The main difference between the Wheeler model and the one from Karma is that in the latter one kinetics can be eliminated for any undercooling by a proper choice of the parameters. Karma [**20**] showed that with his model quantitative results can be obtained already for interface thicknesses comparable to the capillary length $w_0 \approx d_0$, whereas in the Wheeler model the interface thickness must be much smaller than d_0. It was stated [**21**] that the Karma model is better suited for very low undercoolings $\Delta \ll 1$ where the kinetic term βv_n can be neglected. In the Wheeler-model the $\beta = c_p/L\mu \to 0$ leads to numerically unstable equations.

In the sharp interface limit $\varepsilon \to 0$ the kinetic coefficient is recovered by the relation

$$\beta(\mathbf{n}) = a_1 \frac{\tau(\mathbf{n})}{\lambda w(\mathbf{n})}. \tag{14}$$

In the thin interface approximation, where $\delta u \ll |u_{interface}|$ corresponding to $wv/D \ll \beta v$ the kinetic coefficient can be written as

$$\beta(\mathbf{n}) = a_1 \frac{\tau(\mathbf{n})}{\lambda w(\mathbf{n})} \left(1 - a_2 \frac{\lambda w(\mathbf{n})^2}{D\tau(\mathbf{n})}\right), \tag{15}$$

where $a_2 = 0.6267$ is another numerical constant. For small undercoolings the effect of the kinetic coefficient is negligible $\beta \approx 0$. Therefore it is possible to choose $\tau(\mathbf{n})$ in such a way, that $\beta(\mathbf{n})$ vanishes:

$$\tau(\mathbf{n}) = \frac{a_2 \lambda w(\mathbf{n})^2}{D} \tag{16}$$

For undercoolings higher than say 0.5 this choice of τ is inappropriate as the influence of the kinetic term significantly increases. MD simulations [**41**] have shown that the correction term $a_2 \lambda w(\mathbf{n})^2/D\tau(\mathbf{n})$ in eq.(15) can be neglected for high undercooling $\Delta \approx 1$. This leads to

$$\tau(\mathbf{n}) = \frac{1}{a_1}\beta(\mathbf{n})\lambda w(\mathbf{n}). \tag{17}$$

The application of Karma's model to solidification at high undercoolings was demonstrated by Bragard et al. [**38**]. In the phase-field equation (12) they replaced

λu by a non-linear numerical function $h(\lambda u)$ in order to recover the linear relationship between interface undercooling and velocity $u|_{interface} = -\beta v_n$. Moreover, the interface kinetic coefficient was modeled anisotropically as in equation (14). It was demonstrated in [**38**] that the growth morphologies depend on the anisotropy of the kinetic coefficient. In the present study, the model with eliminated kinetics (16) was used for the whole range of undercoolings.

3. Numerical schemes

The equations of Karma's model (12) were first non-dimensionalized by transforming space coordinates $(x, y, z) \to w_0(x, y, z)$ and time $t \to w_0^2/Dt$. This leads to the equations

$$\widetilde{\tau}\eta^2 \frac{\partial \phi}{\partial t} = \eta^2 \nabla^2 \phi + [\phi - \lambda u(1-\phi^2)](1-\phi^2) \tag{18}$$

$$\frac{\partial u}{\partial t} = \nabla^2 u + \frac{1}{2}\frac{\partial \phi}{\partial t} \tag{19}$$

where $\widetilde{\tau} = \tau_0 D/w_0^2$. In the case of vanishing kinetics we find $\tau_0 = a_2 \lambda w_0^2/D$ and therefore $\widetilde{\tau} = a_2\lambda$. In the case of high undercoolings $\widetilde{\tau}$, using the relation $w_0 = \lambda d_0/a_1$, becomes

$$\widetilde{\tau} = \frac{\tau_0 D}{w_0^2} = \frac{D}{w_0^2}\frac{1}{a_1}\beta\lambda w_0 = \frac{\beta D}{d_0} \tag{20}$$

We have used two different numerical schemes in order to solve the phase-field equations. For low undercoolings $\Delta < 0.5$ we have used a parallel adaptive finite element (paFEM) code [**39**]. In this approach, mesh repartitioning is performed after every grid update in order to balance the load on every processor. The finite element discretization was performed automatically by the symbolic computational tool femLego [**40**]. For higher undercoolings and therefore sufficiently well developed morphologies we implemented a parallel finite difference (paFD) code. We have found that for $\Delta < 0.5$ the paFEM code is more efficient in terms of computing time, where as for higher undercoolings the paFD code turned out to be faster. In both methods a second order accurate space discretization was implemented, and a first-order Euler scheme was used to discretize the time derivatives. To discretize the anisotropic Laplacian in the paFD code, we applied the standard central differences:

$$\begin{aligned}\frac{\partial}{\partial x_i}\left(|\nabla\phi|^2\eta(\mathbf{n})\frac{\partial\eta(\mathbf{n})}{\partial(\phi_x)}\right) &= \frac{\partial}{\partial x_i}\left(\eta(\mathbf{n})\cdot 16\gamma\left(\frac{\phi_x}{|\nabla\phi|^2} - \frac{\phi_x^4+\phi_y^4+\phi_z^4}{|\nabla\phi|^4}\right)\frac{\partial\phi}{\partial x_i}\right) \\ &= \frac{\partial}{\partial x_i}\left(f(\phi_x,\phi_y,\phi_z)\frac{\partial\phi}{\partial x_i}\right)\end{aligned} \tag{21}$$

where x_i corresponds to x, y, z. Therefore

$$\begin{aligned}\frac{\partial}{\partial x_i}\left(f\frac{\partial\phi}{\partial x_i}\right)\Bigg|_{i,j,k} &= \frac{1}{2\Delta x^2}\left[(f_{i+1,j,k}+f_{i,j,k})(\phi_{i+1,j,k}-\phi_{i,j,k})\right. \\ &- \left.(f_{i,j,k}+f_{i-1,j,k})(\phi_{i,j,k}-\phi_{i-1,j,k})\right]\end{aligned} \tag{22}$$

and the first derivatives were approximated by

$$\phi_x = \frac{\phi_{i+1,j,k} - \phi_{i-1,j,k}}{2\Delta x} \tag{23}$$

For the discretization we have used equal grid steps in all directions $\Delta x = \Delta y = \Delta z$. The smallest grid resolution of the adaptive grids was chosen to be equal to the grid size of the uniform meshes. In the parallel FD implementation the mesh was equally split between processors, so that every processor received the same load. During calculations, the data exchange between the processors was performed by the MPI protocol. Typically the 3D simulations were performed on 32 processors.

Visualization of the three dimensional results represented a problem when the computational domain exceeded 300^3 points. Before visualizing the data by OpenDX we had to preprocess the results. This was done by extracting the isosurface of the data where the phase field variable is a constant value - usually the average between solid and liquid state (for the Wheeler model we have used 0.5 and for the Karma model 0) . On this spatial information of the interface the temperature field was extracted. Subsequently we have plotted the information $T|_{\phi=\text{const}}(x, y, z)$. In order to extract the isosurface we interpolated the surface between the grid positions using tetrahedral decompositions, so that no ambiguities can arise.

4. Experiments

In our experiments we are able to observe a growing crystal in three dimensional free growth. We use the rare gas xenon as a model substance for metals because (i) it forms a 'simple liquid', (ii) it has a low melting entropy and (iii) it crystallizes in fcc structure (4-fold symmetry). Xenon is transparent in solid and liquid state, therefore it is possible to observe the growth process in situ. Undercoolings that are experimentally accessible with xenon are in the range of $50m\text{K} \leq \Delta T \leq 220m\text{K}$ (corresponding to $10^{-3} \leq \Delta \leq 10^{-2}$ in dimensionless units). The melting temperature of xenon is $T_m = 161.389\text{K}$.

The experimental setup consists of a high precision cryostat with which the temperature can be stabilized better than $\pm 10^{-4}$K as long as necessary. The cooling substance for the cryostat is liquid nitrogen. We use isopentane as a thermostating liquid. An adjustable helium gas atmosphere between the liquid nitrogen and the isopentane allows to control the heat flux. The temperature is measured by means of temperature sensitive resistors (Pt-100). The electrical heating is regulated by a commercial Proportional-Integral-Differential-Controller (PID). A stirrer in the thermostating liquid produces a laminar flow in order to ensure a homogeneous temperature distribution in the heat bath. The actual growth vessel is immersed in the heat bath. In order to initiate the growth of the crystal we use the capillary injection technique proposed by Glicksman and Schaefer [**28**]: A capillary reaches into the growth vessel which is completely filled with undercooled xenon. A small crystallization seed is produced in the upper part of the capillary. The crystal starts growing and moves along the capillary until it reaches the end and enters the state of free three dimensional growth. Our experimental apparatus allows us to turn the capillary along its axis so that the crystal can be oriented to its maximal projection

Description	Value
Range of undercooling ΔT	$50m\mathrm{K} \leq \Delta T \leq 220m\mathrm{K}$
Anisotropy γ (MD simulations)	1.55%
Capillary length d_0	4.9E-8 cm
Specific heat C_p	s: 36.0 l:44.6 J/mol K
Interfacial free energy σ	9.95mJ/m^2
Latent heat L	2299J/mol
Diffusivity κ	s:4.96E-3 l:7.29E-3
Conductivity	s:4.76E-3, l:0.734E-3 W/cm K
Melting temperature T_m	161.3897K
Melting entropy ΔS_m	24.24J/mol
Molar weight M_{xe}	131g/mol

TABLE 1. Relevant material properties of xenon.

area. It is also possible to shift the capillary up and down (vertical translation) in order to follow the crystal during its growth. A self built periscope allows the in situ observation of the crystal. The tested optical resolution is 1.22μm. We use a spatially homogeneous cold light source to illuminate the crystal. As solid and liquid state are both transparent the crystal can only be seen due to differences in the index of refraction ($n_{\text{liquid}} = 1.3918$, $n_{\text{solid}} = 1.4507$ for wave length $\lambda_{light} = 546$nm) [**29, 30**]. A more detailed description of the experimental setup and a sketch of the apparatus is given in [**32, 33, 14, 15**]. A high resolution digital CCD-camera (1280x1024 pixels) records the images on a computer. The relevant data for xenon are given in table 1. A more complete list can be found in [**33**].

5. Results and discussion

5.1. Experimental results. Before presenting our results for the phase field simulations and experimental results we would like to define how we classified the found structures. Although it was stated in [**8**] that the doublons are actually building blocks for seaweed structures we believe that the doublon-case should be treated as a separate morphology. We define the different morphologies in the following way:

Dendrite: The dendritic morphology shows a 4-fold symmetry (fcc) perpendicular to the main axis of growth. On the four fins in 3D respectively two fins in 2D side branches appear after a certain parameter dependent distance behind the tip. Although no coupling between the individual fins exists the sidebranch frequency on each fin is in average the same. Despite of the ongoing discussion about the exact shape of the tip [**21, 35, 36, 37**] it can at least be stated that it has a convex spear-like appearance. In a moving frame of reference the tip remains unchanged and the side branches move upwards, grow longer and compete with their direct neighbours.

Seaweed: The seaweed does not show any apparent symmetry nor is a distinct main tip observable. The main property of this morphology is its

FIGURE 1. Examples of typical morphologies obtained in our three dimensional free growth experiments: seaweed growth (top), doublon growth (middle), dendritic growth (bottom).

continuous splitting of any prominent tip in the temporal evolution. One of the new formed tips is immediately outgrowing the other one and starts increasing its tip radius again whereas the other decelerates and eventually stops growing.

Doublon: The doublon morphology shows one distinct axis of symmetry. The main feature of this morphology is that two main tips grow simultaneously and parallel influencing and stabilizing each other. Unlike the seaweed morphology the two tips evolve with the same velocity and hinder each other to outgrow the other tip unless a perturbation or experimental asymmetric noise is perturbing the system. While doublons in 2D possess a protected channel where heat is not able to flow out this is obviously not true in 3 dimensions. The structure is topologically different from its corresponding 2D pendant. It should also be mentioned that doublons have an orientational order and should therefore be classified as a "dendrite" within Brener's classification system.

Experimentally the different morphologies are produced in two different ways: i) spontaneously and ii) induced. Spontaneous transitions are usually observed only for very low undercoolings $\Delta T < 90$mK ($\Delta = 10^{-3}$). We have observed spontaneous morphology changes from seaweed to doublons and back. For higher undercoolings we observe a stabilization of the structure to dendritic morphologies. However it is still possible to induce a morphology change by perturbing the crystal: By shifting the capillary downwards and thus washing away the steady state isothermal lines, the crystal suddenly "feels" a much colder environment which leads to a drastic increase of the growth velocity and so eventually to a morphology change. As new isolines are formed around the crystal the interface is more and more shielded against the virtual high undercooling and after a certain time (typically 150-300s) the crystal relaxes back to the departing dendritic morphology.

Typical examples of the experimental morphologies are given in figure 1.

5.2. Numerical results. We have performed all our simulations for the Wheeler-model on a 2000x2000 square lattice with the following parameters: $\alpha = 400$, $m = 0.05$, $\varepsilon = 0.005$, $\Delta x = 0.01$, $\Delta t = 2 \cdot 10^{-5}$. The undercoolings were chosen $\Delta = 0.1, 0.2, ..., 0.9$ and the anisotropies $\gamma = 6.5 \cdot 10^{-3}, 1.3 \cdot 10^{-2}, ..., 6.5 \cdot 10^{-2}$, so that $\gamma_{max} = 6.5\%$. Additionally we have refined the choice of the anisotropy for given undercoolings in order to minimize the uncertainty regime of the morphology border. We have always used a spherical seed with a radius of $7 \cdot \Delta x$ placed at the left bottom corner of the domain as initial conditions for the simulated growth.

The results for the Wheeler model are given in figure 3. The anisotropy axis goes from 0 to 6.5% as it has been shown in [**42**] that the for higher anisotropies the crystal changes from rough to facetted growth. The blue zone corresponds to the uncertainty regime, where we have found seaweed morphologies ("sw") on the left side and dendritic morphologies ("den") on the right side. When comparing the diagram with the one of Brener et al. in figure 2 we found a qualitative correspondence. However when comparing it quantitatively we state that the border between the seaweed morphology and the dendritic morphology is much steeper than predicted. Additionally it can be seen that the morphology boundary is not

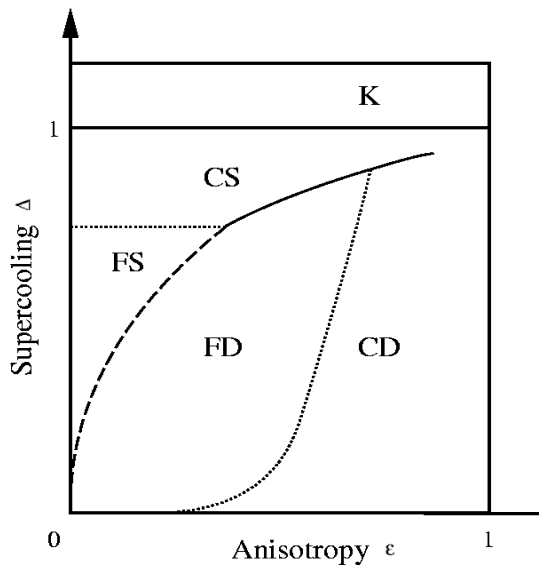

FIGURE 2. Morphology diagram in 2D based on analytical calculations by Brener et al. [**6, 7, 8**]. A distinction between dendritic (D) and seaweed(S) growth. Both domains are subdivided into compact (C) growth with average constant density and fractal (F) growth with fluctuating density.

globally concave as predicted but shows rather a sigmoid behaviour: for small undercoolings we find a convex shape of the border. The point where it changes to a concave behaviour is approximately $\Delta = 0.3$ and $\gamma = 0.9\%$. In our morphology diagram we find a region of parameters, where doublon structures evolve with the same initial conditions as in all other simulations. This domains is red and marked with "db". The doublon domain mainly develops on high undercoolings with sufficiently strong anisotropy. The higher the undercooling is, the less the strength of the anisotropy has to be in order to overcome the continuous tip splitting, stabilizing to two parallel evolving tips.

The initial coarse parameter scan of 100 simulations for the whole domain was refined by a binary search between two different anisotropies leading to different morphologies for the same undercooling. We have tied up the border (at least for higher undercoolings) to $\Delta\gamma < 2 \cdot 10^{-2}\%$. For lower undercoolings the simulation time takes increasingly longer therefore the variance is bigger. In order to refine the border from the right hand side we have applied following intuitive principle: for a given undercooling a certain anisotropy is necessary to stabilize the morphology to a dendrite. If the undercooling is increased - leading to a higher growth velocity the strength of the anisotropy must increase as well. Mathematically we therefore applied the principle of monotony for $\gamma_2(\Delta_2) \geq \gamma_1(\Delta_1)$ for $\Delta_2 > \Delta_1$. Therefore knowing the morphology boundary for higher undercoolings, we could also reduce the variance for lower undercoolings.

We have considered only the main growth directions to determine the morphology of a structure. Despite of the fact that for very high undercoolings and

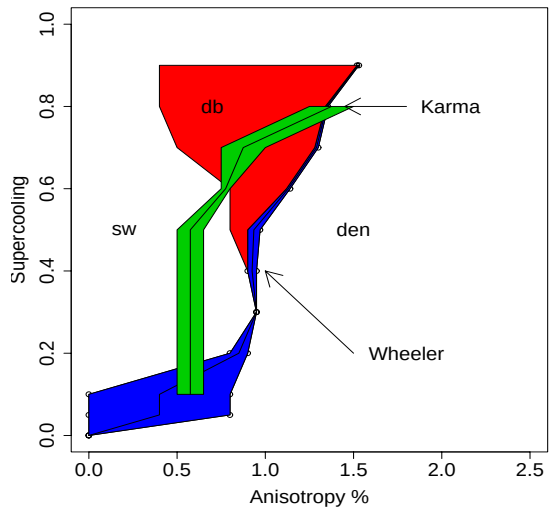

FIGURE 3. Morphology diagram in 2 dimensions of the Wheeler model and the Karma model . The blue and green zones correspond to the uncertainty regimes given by the Wheeler and the Karma models, respectively. The dendritic domain is denoted as "den", seaweed as "sw" and doublon (red region) as "db".

sufficiently low anisotropies spherulite structures are observed (the envelope is spherical) only the two directions $< \pm 1, 0 >$ and $< 0, \pm 1 >$ contributed to the determination of the morphology. If these directions formed one single tip then the morphology would be a dendrite. Showing two stable tips (regardless of what other directions would show) the morphology was determined as a doublon. When the directions showed a continuous tip splitting and erratic growth directions the structure was classified as a seaweed.

Equations (18) and (19) of Karma's model were solved in two dimensions on a 2000x2000 mesh with $\Delta x = 0.8$ and $\Delta t = 0.1$. The initial spherical seed was chosen to have a radius of $5 \cdot \Delta x$. We shall emphasize that the big difference in the non-dimensional parameters Δx and Δt for the two models is due to different values of the reference length w_0 used for non-dimensionalization. The 2D morphology diagram given by the Karma model is presented (superimposed to the morphology diagram for the Wheeler model) in Fig. 3. As we have used the same physical parameters for both models in the 2D simulations it is not surprising that for uncritical values like the morphology far away from the morphology border the results are identical. We however state that there is one significant difference: the border given by the Karma model is shifted to the left. The choice of the parameter λ has a crucial impact not only on the size of features of the crystal, but also on its morphology. We observed, that for Δ and γ close to the morphology border, an increase of λ leads to a transition from a dendritic to a seaweed structure, i.e. large values of λ give a false morphology. This impact of λ becomes more noticeable at

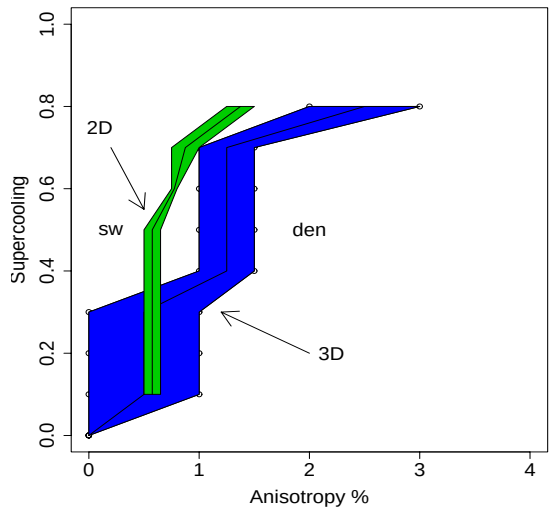

FIGURE 4. Morphology diagram in 3 dimensions of the Karma model superimposed with the values of the 2D case .The blue region represents the uncertainty regime, where seaweed morphologies ("sw") are found on the left side and dendritic morphologies ("den") on the right side.

higher undercoolings [**38**]. We have chosen λ to vary from 20 to 3 for undercoolings 0.1 to 0.8, respectively.

In general, we found that an increase of λ would shift the morphology boundary to the right, i.e. closer to the one obtained with the Wheeler model. Since the interface thickness used in Wheeler's model is approximately 20 times greater than the capillary length of Ni, this can explain the discrepancy of the results given by the two models. Similar to the Wheeler model, a 2D doublon region was found for the Karma model at high undercoolings and moderate values of anisotropy.

The discrepancy is more pronounced at low undercoolings. This could come from the fact that the Wheeler model does not consider the effect of vanishing interface kinetics for $\Delta \to 0$. Therefore, as the computational costs for 3D simulations even in the parallelized version of our codes are considerable, we have decided to perform 3D calculations only for the Karma-model.

Figure 5 shows the results of all the simulations which were performed in three dimensions as a table of anisotropy and undercooling. For every simulation the value of λ and the final time (in non-dimensional time units) is provided to give an impression on how fast the crystals grow dependent on Δ. Most of the three dimensional simulations were performed in a domain of size 400^3. An initial seed was always placed in one of the domain's corners, i.e. we calculated only 1/8 of the crystal. The morphologies presented in Fig. 5 are then obtained by mirroring with respect to the main symmetry axis.

The morphology diagram for 3 dimensional structures superimposed to the one of 2D structures is given in figure 4. Comparing the shape of the morphology

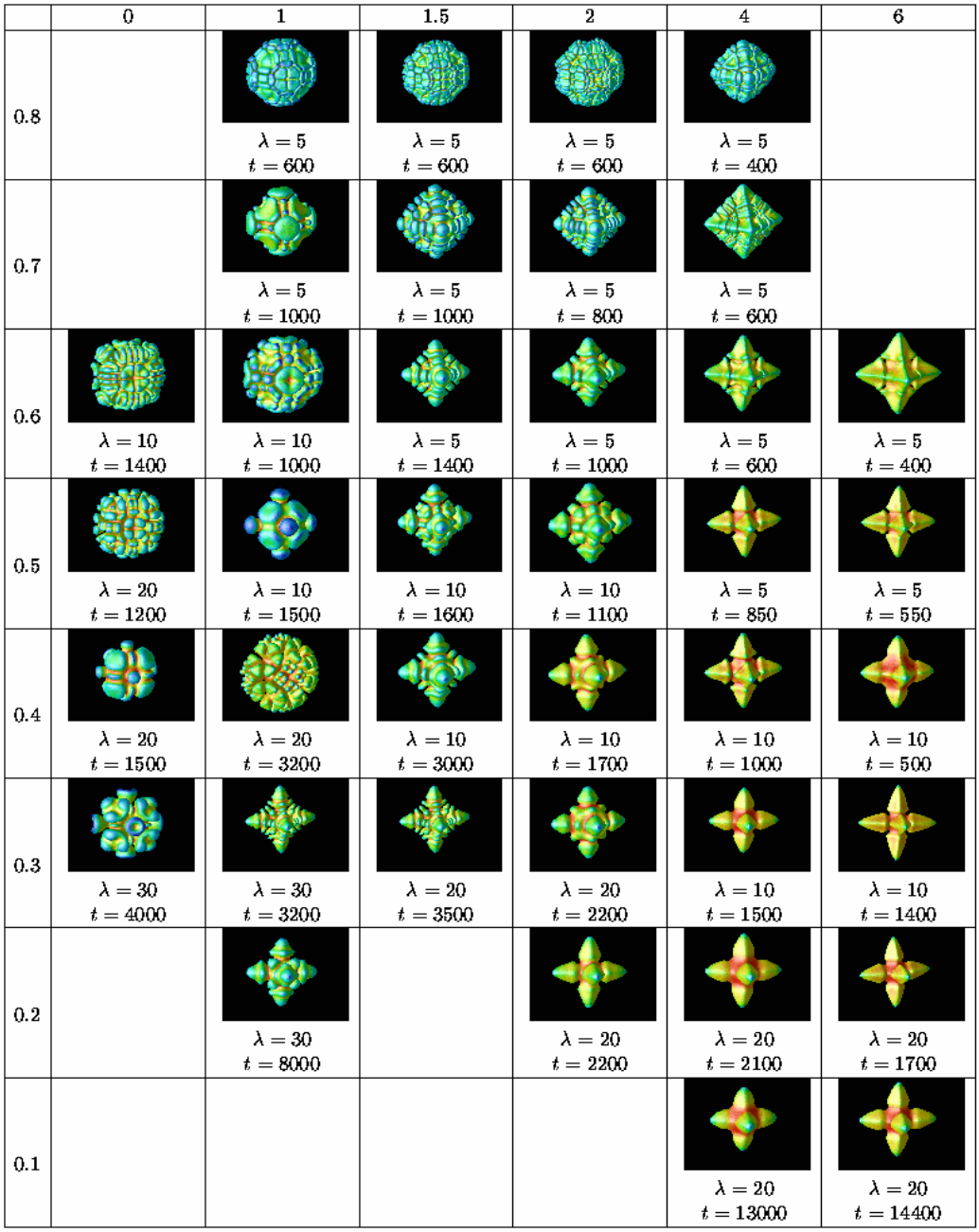

FIGURE 5. A table with the simulated three dimensional morphologies. Every structure is supplied by the parameter λ and the non-dimensional final time of the simulation. Columns and rows correspond to different values of γ and Δ, respectively.

boundary with the one in 2 dimensions we find that they look qualitatively the same: both show the same sigmoidal behavior. Quantitatively however, the two boundaries differ: the 3D boundary is shifted by an amount of 0.32 along the anisotropy axis. This shift might be explained by the topological differences of 2D and 3D objects: a 3D object must have a higher anisotropy in order to stabilize its growth to dendritic morphology as an additional spatial direction is available to transport heat away.

It is interesting to note that no 3D doublons as produced in our experiments (Fig. 1) could be found. A doublon domain such as we find in the 2D morphology diagram does not seem to exist in 3D. Having noticed this, we have simulated 3D doublon structures with special initial conditions: two spherical seeds placed at a distance of $40\Delta x$. We obtained structures which look like two dendrites growing in parallel, where each one was missing one fin, forming a gap between the two tips. We attached the seeds in the middle of one of the walls, thus the morphology given in Figure 6 is presented as simulated, i.e. without mirroring. In order to observe finer details of the two tips growing in parallel, we applied the following procedure. At a certain stage of the simulation, when the two tips are sufficiently developed, we shift the computational box upwards, so that two tips have the possibility to grow further into the undercooled melt. Thus, we "chop" the doublon and consider only the tips. The same structure as in Figure 6 with superimposed temperature field in the cross section passing through the tips of both fins is given in Figure 7. With the present numerical implementation, these two tips would remain in a stable growth mode forever. In order for one of them to outgrow the other, we need to model asymmetric disturbances as found in our experiments, e.g. applying noise only to one of the tips.

6. Conclusions

We have performed two dimensional phase field simulations for the Wheeler model and the Karma model and found qualitative agreement between the models and theoretical predictions by Brener et al. [**6**]. Quantitatively however differences are found: the Karma model is strongly dependent on the use of the parameter λ. By increasing λ it is possible to shift the found morphology boundary to the right in direction of the one found for the wheeler model for constant interface thickness for all simulations. Both models show a much steeper boundary than predicted by the theory. Additionally for low undercoolings we have found a convex behaviour which is opposed to the theoretical predictions. We have found for both models well defined doublon regions for high undercoolings and moderate strength of anisotropy. Furthermore we have performed 3D simulations for the Karma model with the same λ as in 2D and have found that the morphology boundary is qualitatively identical to the one in 2D however it is shifted by an amount of 0.32 in direction of higher anisotropies. We state that in all the 3D simulations no doublons have been found. However by using special initial conditions it was possible to produce stable doublon growth, very similar to the morphology found in our experiments. Comparing the found results with our experiments we find very nice qualitative agreement with the doublon and dendritic morphology. For the seaweed morphology however we state that our experimental structures still show four fins in which the side

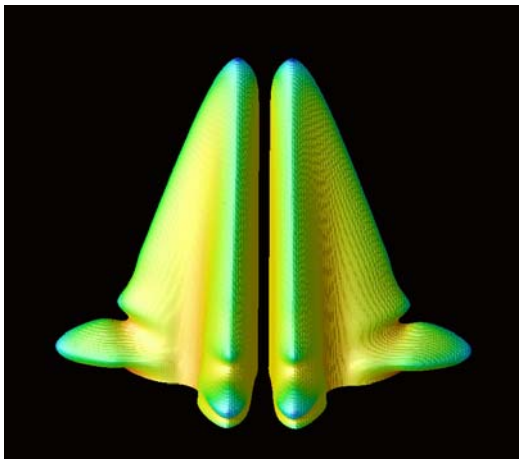

FIGURE 6. Two tips of a doublon computed for $\gamma = 4.5\%$, $\Delta = 0.5$ and $\lambda = 5$. The large values of γ and Δ were chosen to speed up the calculations.

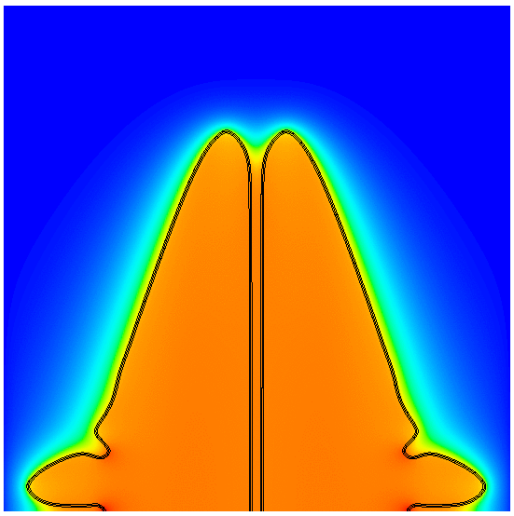

FIGURE 7. Temperature distribution in the cross section passing trough the doublon tips (Fig.6). The superimposed black line shows position of the solid-liquid interface .

branches and the main tip grow completely irregular (and eventually split) whereas for the simulations the four-fold symmetry is not maintained and a rather spherical envelope is observed.

Acknowledgments

We thank Professor Dr. H. R. Ott for his support of our experiments. This work was supported by the Swiss National Science Foundation and the Swedish Research Council for Engineering Science (TFR)

References

[1] L. I. Rubinstein, "*The Stefan Problem*", Providence, Rhode Island, 1971
[2] G.P. Ivantsov, Dokl. Akad. Nauk SSSR **58**, 567 (1947).
[3] A. Papapetrou, Z. Kristallogr. **92**, 89 (1935)
[4] J.S. Langer, Rev. Mod. Phys. **52**, 1 (1980).
[5] J.S. Langer, in *Chance and Matter: Les Houches, Sessions XLVI, 1986*, edited by J. Souletie, J. Vannimenus and R. Stora (Elsevier Science Publisher B.V., Amsterdam, 1987), pp. 629-711.
[6] E. Brener, K. Kassner, H. Müller-Krumbhaar and D. Temkin, Int. Jour. Mod. Phys. C **3**, 825 (1992).
[7] E. Brener, H. Müller-Krumbhaar and D. Temkin, Europhys. Lett. **17**, 535 (1992).
[8] E. Brener, H. Müller-Krumbhaar and D. Temkin, Phys. Rev. E **54**, 2714 (1996).
[9] R. Kupferman, O. Shochet and E. Ben-Jacob, Phys. Rev. E **50**, 1005 (1994)
[10] E. Ben-Jabob, Contemporary Physics 34, 247 (1993)
[11] R. Kobayashi, Physica D **66**, 410 (1993)
[12] S. Akamatsu and G. Faivre, Phys. Rev. E **58**, 3302 (1998).
[13] M.E. Glicksman, R.J. Schaefer, J.D. Ayers, Met. Trans. A, Vol. **7A**, 1747 (1976)
[14] I. Stalder and J.H. Bilgram, Europhys. Lett. **56**, 829 (2001).
[15] H.M. Singer, *Charakterisierung von Seaweed bei Xenon-Kristallen,* (Diploma thesis, Eidgenössische Technische Hochschule, Zürich-CH, 2001).
[16] T. Ihle and H. Müller-Krumbhaar, Phys. Rev. Lett. **70**, 3083 (1993).
[17] T. Ihle and H. Müller-Krumbhaar, Phys. Rev. Lett. E **49**, 2972 (1994).
[18] D. Juric and F. Tryggvason, J. Comp. Phys. **123**, 127(1996)
[19] G. Caginalp ans W. Xie, Phys. Rev. E **48**, 1897 (1993)
[20] A. Karma and W.-J. Rappel, Phys. Rev. Lett. **77**, 4050 (1996).
[21] A. Karma and W.-J. Rappel, Phys. Rev. E **57**, 4323 (1998).
[22] A.A Wheeler, B.T. Murray and R.J. Schaefer, Physica D **66**, 243 (1993)
[23] S.L. Wang, R.F. Sekerka, A.A. Wheeler, B.T. Murray, S.R. Coriell, RJ. Braun and G.B. McFadden, Physica D **69**, 189 (1993)
[24] R. Kobayashi, Simulations of Three Dimensional Dendrites, Pattern Formation in Complex Dissipative Systems, ed. S.Kai, World Sci. Pub. Singapore, 1992, 121-128
[25] T. Abel, E. Brener and H. Müller-Krumbhaar, Phys. Rev. E **55**, 7789 (1997).
[26] M. Plapp and A. Karma, Phys. Rev. Lett. **84**, 1740 (2000).
[27] H. M. Singer, *Extracting Isosurfaces of 3D Domains*, internal report
[28] M.E. Glicksman, R.J. Schaefer, and J.D. Ayers, Metall. Trans. A **7A**, 1747 (1976).
[29] A.C. Sinnock and B.L. Smith, Phys. Rev. **181**, 1297 (1969)
[30] *Rare Gas Solids*, edited by M.L. Klein and J.A. Venables, (Academic, New York, 1977)
[31] J.H. Bilgram, M. Firmann, and E. Hürlimann, J. Cryst. Growth **96**, 175 (1989).
[32] E. Hürlimann, R. Trittibach, U. Bisang and J.H. Bilgram, Phys. Rev. A **46**, 6579 (1992).
[33] U. Bisang and J.H. Bilgram, Phys. Rev. E **54**, 5309 (1996).
[34] H.M. Singer, J.H Bilgram, J. of Cryst. Growth, in print .
[35] E. Brener, D. Temkin, Phys. Rev. E **51**, 351 (1995).
[36] G.B. McFadden, S.R. Coriell, and R.F. Sekerka, J. Crystal Growth **208**, 726 (2000).
[37] H. M. Singer, and J. H. Bilgram, Phy. Rev. Lett., submitted.
[38] J. Bragard, A. Karma, Y. Lee and M. Plapp Interface Science, **10**, 121-136, (2002)

[39] M.Do-Quan, I.Loginova and G.Amberg, Application of parallel adaptivity to simulation of materials processes, in preparation
[40] G. Amberg, http://www.mech.kth.se/∼gustava/femLego/
[41] J.J.Hoyt, B.Sadigh, M.Asta and S.M.Foiles, Acta Mater, **47**, 3181 (1999)
[42] G.B. McFadden, A.A. Wheeler, R.J.Braun, S.R.Coriell and R.F.Sekerka, Physical review E, **48**, 2016 (1993)